Measurement of Nuclear Recoils in the CDMS II Dark Matter Search

A DISSERTATION

SUBMITTED TO THE FACULTY OF THE GRADUATE SCHOOL

OF THE UNIVERSITY OF MINNESOTA

BY

Scott M. Fallows

IN PARTIAL FULFILLMENT OF THE REQUIREMENTS

FOR THE DEGREE OF

Doctor of Philosophy

December, 2014

Acknowledgements

Countless wonderful people at the University of Minnesota, in the wider CDMS collaboration, and beyond have earned my gratitude over the better part of the last decade, and there's no realistic possibility of doing them justice in this space.

First and foremost, any effectiveness I have as a scientist must be credited to the towering influence of my advisor Prisca Cushman, who has consistently had the quickest and most incisive thought and action process I've ever seen. Her example is one I'll always be working to live up to. Vuk Mandic has been an excellent mentor as well, with a calm, encouraging voice always keeping things in perspective. Prolonged exposure to such level-headed, optimistic, world-class physicists has had an immensely positive influence on me.

My first taste of CDMS came before I even formally began as a graduate student, and I'm very grateful to Long Duong, Angie Reisetter, and Xinjie Qiu for welcoming me to the group before I had any clear right to be there, showing me the ropes, and making me feel that I could meaningfully contribute to a world-leading experiment before I'd even cracked open my copy of Jackson for the first time.

My very good friend Matt Fritts was there from that first summer as well, and it would be hopeless to try to measure the influence he's had on my appreciation of science and the wider world. As a naive dweeboid coming out of my undergraduate years badly in need of expansion from a very narrow life-parameter space, direct evidence and reminders that science is intrinsically groovy have been extremely helpful for keeping focused over the years, while learning how to grow into a more broadly sophisticated life (and I think we can agree that nothing says "sophisticated" like *Italian Spiderman*).

Those of the second wave of my Superiors, Oleg Kamaev, Hassan Chagani, and Anthony Villano, were each a unique pleasure to work with, having vast expertise in widely varying areas that I felt lucky to be able partially absorb. Anthony in particular made some of the deeper-and-darker years feel less isolated, which was very valuable and appreciated. My grad student office-mates, whether we shared the space for many years or only briefly – Jianjie Zhang, Tommy Hofer, Mark Pepin, D'Ann Barker, Hannah Rogers, and Allison Kennedy – were all a joy to spend time with, and I'm not yet sure how I'll manage to get by without being surrounded by so many active minds so willing to engage with and make nearly any topic deeply interesting and improbably amusing. Even our transient undergraduates have been uncommonly great people, with special thanks to Kirby Myers and Mark Johnson for introducing us to the best Korean karaoke joint in the Midwest.

The CDMS collaboration has been an unbelievably strong group of people from whom to learn what it takes to be a good scientist, and their uncompromising standard of courtesy and respect in the face of immeasurable stressors may be a world-leading achievement in itself. I especially appreciated the opportunity to work with and receive guidance from Lauren Hsu, Joel Sander, Dan Bauer, Richard Schnee, Ray Bunker, Dave Moore, and Kevin McCarthy. Icebound sunless shifts at Soudan with Scott Hertel, Todd Doughty, Joseph Kiveni, Durdana Balakishiyeva, Tarek Saab, Tali Figueroa, and others have made for many strangely fond memories I certainly won't forget.

Outside CDMS, thanks to Scott Thaller and the space physics crew for keeping my philosophy chops honed over the barley-juice. Thanks are also due to so many wonderful and patient friends in Minnesota, especially Kat for sustaining me with singularly bizarre and thoughtful gifts when I disappeared into the thesis-hole. Deep thanks to my friends on opposite sides of Canada for showing me that there are beautiful ways to live, if you can find them. And to my oldest friends in Minneapolis – Amelia, Stuart, Boris – thank you for teaching me that having a life need not prevent one from living.

Dedication

To my impossibly selfless parents, without whom I would be nothing and nobody.
You've done so much more for me than any person could possibly deserve.
I hope some day to find the words and means to express the depth of my gratitude.

and

To my boundlessly loving grandmother, Violet Weber, who set all this in motion.
Systole shudders to diastole by grace of your living memory alone, driving out the nameless dark and guiding me toward awe and wisdom. Love forever, Granny.

Abstract

The Cryogenic Dark Matter Search (CDMS) experiment is designed to directly detect elastic scatters of weakly-interacting massive dark matter particles (WIMPs), on target nuclei in semiconductor crystals composed of Si and Ge. These scatters would occur very rarely, in an overwhelming background composed primarily of electron recoils from photons and electrons, as well as a smaller but non-negligible background of WIMP-like nuclear recoils from neutrons. The CDMS II generation of detectors simultaneously measure ionization and athermal phonon signals from each scatter, allowing discrimination against virtually all electron recoils in the detector bulk. Pulse-shape timing analysis allows discrimination against nearly all remaining electron recoils taking place near detector surfaces. Along with carefully limited neutron backgrounds, this experimental program allowed for "background-free" operation of CDMS II at Soudan, with less than one background event expected in each WIMP-search analysis. As a result, exclusionary upper-limits on WIMP-nucleon interaction cross section were placed over a wide range of candidate WIMP masses, ruling out large new regions of parameter space.

These results, like any others, are subject to a variety of systematic effects that may alter their final interpretations. A primary focus of this dissertation will be difficulties in precisely calibrating the energy scale for nuclear recoil events like those from WIMPs.

Nuclear recoils have suppressed ionization signals relative to electron recoils of the same recoil energy, so the response of the detectors is calibrated differently for each recoil type. The overall normalization and linearity of the energy scale for electron recoils in CDMS II detectors is clearly established by peaks of known gamma energy in the ionization spectrum of calibration data from a ^{133}Ba source. This electron-equivalent ($\mathrm{keV_{ee}}$) energy scale enables calibration of the total phonon signal ($\mathrm{keV_t}$) by enforcing unity yield for electron recoils, in aggregate. Subtracting an event's Luke phonon contribution from its calibrated total phonon energy ($\mathrm{keV_t}$), as measured by the ionization signal, results in a valid measure

of the true recoil energy ($\mathrm{keV_r}$) for both electron and nuclear recoils.

I discuss systematic uncertainties affecting the reconstruction of this recoil energy, the primary analysis variable, and use several methods to constrain their magnitude. I present the resulting adjusted WIMP limits and discuss their impact in the context of current and projected constraints on the parameter space for WIMP interactions.

Contents

List of Tables

List of Figures

Chapter 1

Introduction: Evidence for Dark Matter

Cataloguing the constituents of the Universe and their properties has been a central concern of natural philosophy since its inception. Over the last century, the most readily accessible components of the Universe have been studied in exacting detail by the developing field of high energy particle physics, culminating in a theory called the Standard Model: a major human achievement that predicts the results of electromagnetic, weak, and strong nuclear interactions of subatomic particles with incredible precision.

And yet the Standard Model is incomplete. Its domain is largely that of the leptons and quarks that make up ordinary baryonic matter, and the mediating fields by which they interact. We now have overwhelming evidence from several independent lines of observation that the familiar baryonic matter making up all the planets, stars, and interstellar gas visible to our eyes and telescopes constitutes less than 5% of the total mass-energy content of the Universe.

These and other observations are unified into the ΛCDM (concordance) model. This "standard model" of Big Bang cosmology is one in which the Universe contains a cosmological constant, Λ, representing a dark energy component that dominates the overall

energy density ($\Omega_\Lambda \approx 68.3\%$), as well as a relatively large cold dark matter (CDM) component. The model parametrizes observations of a flat Universe ($\Omega_{\text{total}} \approx 1$) expanding at an increasing rate. This acceleration is due to the present dominance of the dark energy component, which has negative relativistic pressure, $p = -\rho c^2$, and a constant energy density. This is in contrast with the matter and radiation components, which have energy densities that decrease as $\sim 1/R(t)^3$ and $\sim 1/R(t)^4$, respectively, as the Universe expands. For non-relativistic matter, this is simply dilution of the number density, but relativistic particles also lose energy as their redshifted wavelengths grow with the scale factor $R(t)$. For nearly the first 50,000 years since the Big Bang, relativistic radiation was the dominant component of the Universe's energy density, but its steep $1/R(t)^4$ decline gave way to the matter-dominated era, which prevailed for nearly 10 of the $t_0 \approx 13.8$ billion years since then.

One of the conclusions of ΛCDM is that the baryonic matter that makes up the entire visible universe is dwarfed by roughly five times as much as-yet-unidentified non-relativistic, non-baryonic, non-luminous, nearly non-interacting dark matter ($\Omega_{\text{DM}} \approx 26.8\%$ and $\Omega_{\text{baryon}} \approx 4.9\%$). Several lines of evidence for these conclusions are outlined in the following sections.

1.1 Galactic velocity measurements

Some of the earliest and simplest evidence for the existence of dark matter came from the observation of rotation speeds of spiral galaxies as a function of radius. We can define a galaxy's disk radius R_D in terms of the observed surface brightness, $I(r) = I_0 \exp(-r/R_D)$. The optical radius R_{opt} is defined to be the radius containing 83% of the light. By the above relation, an ideal optical radius will be given by $R_{\text{opt}} = 3.2\, R_D$. For a typical galaxy, the optical radius is on the order of 10 kpc. Clouds of neutral atomic hydrogen typically extend to 2 to 3 R_{opt} and contribute negligibly to the mass. Thus at radii larger than R_{opt}, where $M(r)$ would be expected to become nearly constant, we can equate gravitational and centripetal accelerations for a particle in circular orbit, and predict that the rotation speed

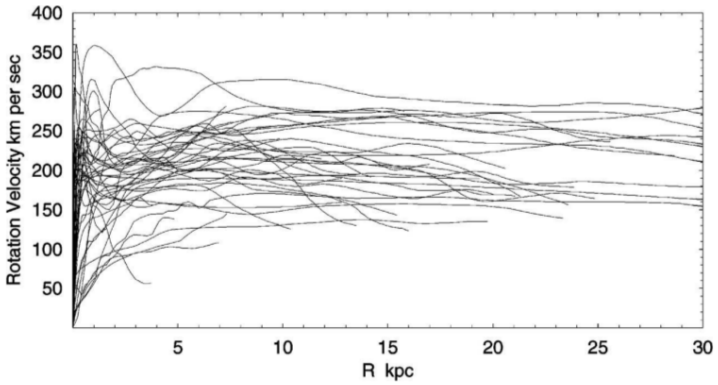

Figure 1.1: Measurements of rotation velocity vs radius for several spiral galaxies, superimposed. Figure from (1).

should fall off as $v \sim r^{-1/2}$.

Instead, numerous observations (1) indicate that the velocity remains remarkably constant out to radii well beyond R_{opt} (shown in Fig. 1.1). This implies that $M(r) \propto r$, which is consistent with an isothermal sphere profile with density $\rho \sim r^{-2}$ continuing out to at least several optical radii. Since the visible galaxy clearly cannot account for this, we infer that there is a non-luminous component extending well beyond the optical radius, which we refer to as the dark matter halo of the galaxy. Without this halo, matter moving at the velocities observed at high radii would not be gravitationally bound and the outer parts of the galaxy would fly apart.

A similar argument can be applied to the velocity dispersions of dwarf and elliptical galaxies. For a self-gravitating system in dynamical equilibrium, from the Virial Theorem, we have $2\langle T\rangle = -\langle V\rangle$, so we expect stars and gas at radius r bounding interior mass M to have velocity dispersion $\langle v^2\rangle \sim GM\langle 1/r\rangle$. From this we can infer the galaxy's mass and again find that the luminous components cannot account for all of it. In fact, it turns out that dwarf satellites of our galaxy appear to be among the most dark matter-dominated objects known, with mass-luminosity ratios several hundred times the solar value.

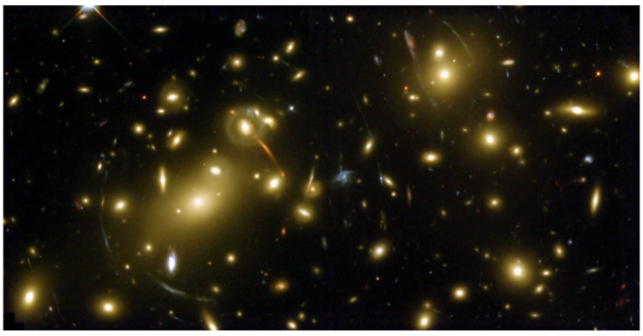

Figure 1.2: The Abell 2218 cluster as seen by the Hubble Space Telescope, showing the characteristic arcing effects of strong gravitational lensing.

1.2 Gravitational lensing

At the galactic cluster scale, a very successful way of determining the mass of astronomical objects is by gravitational lensing: measuring the extent to which light rays are bent when passing through regions containing an excess of matter. In the weak field limit of general relativity, a region with a gravitational potential Φ takes on a refractive index where $n(x) - 1 \propto \Phi(x)$, and behaves much like a classical optical lens. In the case of strong lensing, this can result in distant objects being imaged multiple times or distorted into arcs (shown in Fig. 1.2). Using these arcs one can perform detailed, case-by-case calculations to determine the amount of matter present in the lens. Such cases are not common, but the technique can be applied in the "weak lensing" limit with great utility. This method uses correlations between the ellipticities of background galaxies to provide information on the matter present in the system. This purely statistical method has been widely used, and its application to the study of distant galaxies and clusters from the Sloan Digital Sky Survey produced results consistent with the rest of ΛCDM cosmology (3).

Observations of a pair of colliding clusters known jointly as the "Bullet cluster" (1E0657-558) have provided some of the most striking lensing-based evidence for dark matter. Fig. 1.3 shows contour lines from weak gravitational lensing overlaid on an image of the baryonic matter, traced by the x-rays emitted from the hot gas making up the majority of

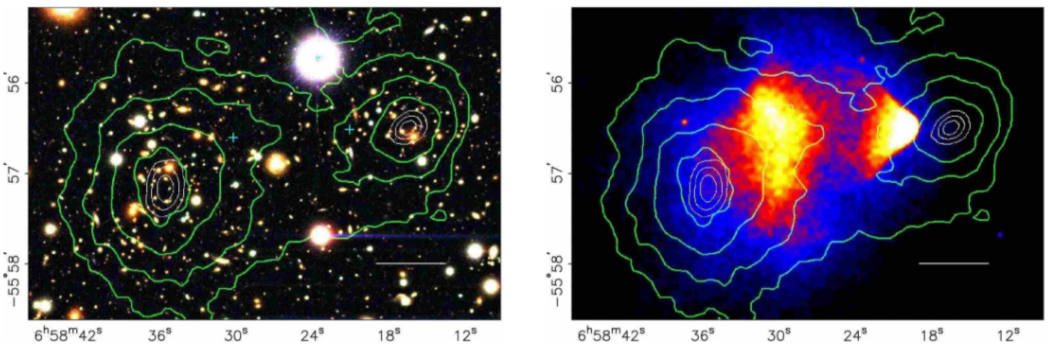

Figure 1.3: Two views of the Bullet cluster (1E0657-558), with contours from weak lensing overlaid. (left) As seen by the Hubble Space Telescope in optical photons. (right) X-ray image from Chandra. The shocked gas (brighter color denotes higher density) trails the motion of the majority of the mass. Evidently the gas experienced dissipative collisions on a level orders of magnitude greater than the rest of the matter. Figure from (4)

the cluster's mass in baryons. The lensing contours clearly indicate that the majority of the mass in each cluster kept moving, each dark matter halo passing through the other, while the shocked colliding gas from each cluster was left behind. This is very strong evidence for the bulk of a cluster's mass being in some non-collisional form (4).

1.3 Other evidence

The theory of Big Bang nucleosynthesis leads to direct constraints on the baryon content of the universe. The resulting number of baryons turns out to be too low to agree with our observations of a nearly flat universe, so we must infer a large non-baryonic component to the total matter content of the universe (5).

Another major body of evidence comes from the study of the formation of large-scale structure in the universe. Anisotropies in the cosmic microwave background (CMB) show inhomogeneities in the distribution of photons at the time of last scattering, when photons de-coupled from baryons, thus preserving the pattern of inhomogenities in the baryons. But observations of nonlinear structure in the present day require a much greater level of collapsed structure in the matter at the time of decoupling than is observed in the baryons

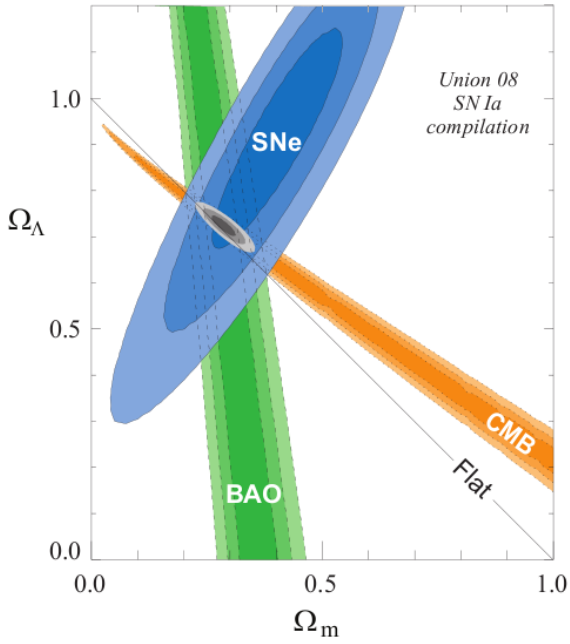

Figure 1.4: Constraints on the major components of the Universe's energy density from the Supernova Cosmology Project (7), shown along with related constraints from measurements of the cosmic microwave background power spectrum and baryon acoustic oscillations. Together the observations indicate a nearly flat Universe ($\Omega \approx 1$) dominated by the dark energy component $\Omega_\Lambda = 0.683$, with a matter component $\Omega_m = 0.317$.

at that time (6). Dark matter reconciles these observations, by collapsing into halos at a much earlier time than the baryonic matter, which must wait until it decouples from the photons.

The structure problem is also evident when considering hydrostatic pressure. As baryonic matter collapses, it heats up, reaching a hydrostatic pressure balance with too high a temperature to collapse further, and no stars are formed. The dark matter component acts as a compacting agent allowing the Jeans instability to proceed to the scale of star production.

Additional observations of light curves of Type Ia supernovae and studies of baryon acoustic oscillations combine with evidence from the CMB to give us a convincing measurement of the matter density of the universe (7), only a small fraction of which can be baryonic (Fig. 1.4). For all these reasons and more, that the majority of the matter in the visible universe is non-baryonic dark matter is now effectively an established empirical fact. The specific form it takes, however, is less certain, and is discussed in the following chapter.

Chapter 2

Dark Matter Candidates

Any candidate to explain the dark matter problem must satisfy what is by now a substantial list of criteria. Big Bang nucleosynthesis and fits to the CMB angular power spectrum both indicate that the matter must be predominantly non-baryonic. Observations such as those of the Bullet cluster and the null results of direct dark matter searches imply that it is also very nearly non-interacting. Since we still see it today, it must at least be stable on time scales comparable to the age of the universe. It must also be non-relativistic, or cold, throughout the formation of large-scale structure, so as not to wash out the formation of structure with large random velocities and a long free-streaming length. Hot dark matter would produce a top-down hierarchy where small structures form by fragmentation of larger structures, yet observations show that galaxies are older than superclusters. These constraints lead naturally to one group of candidate particle, though there are several other viable possibilities as well.

2.1 Weakly interacting massive particles

The leading candidates for the dark matter are weakly interacting massive particles (WIMPs), a fairly general class with an expected mass in the range of about 1 GeV to 10 TeV and weak-scale couplings. These particles are predicted by a proposed extension to the Standard

Model called supersymmetry (SUSY) that also solves several problems in particle physics.

Thermal evidence

Soon after inflation, a massive particle χ will be in thermal equilibium with the other components of the universe, and will experience Boltzmann suppression $e^{-M\chi c^2/kT}$ as the temperature falls. When expansion decreases their density to the point that annihilation of $\chi\chi$ pairs stops (see Fig. 2.1), the comoving number density $n_\chi(T)$ quickly reaches an equilibrium value,

$$n_\chi(T) \approx g \left(\frac{M_\chi kT}{2\pi\hbar}\right)^{3/2} e^{\frac{-M_\chi c^2}{kT}} \tag{2.1}$$

By numerically solving the Boltzmann equation in an expanding universe, we can derive an approximate solution for the annihilation cross section of these particles (8), requiring the relic density to be consistent with that observed for the non-baryonic dark matter, $\Omega_{\rm CDM}h^2 \sim 0.1$. The annihilation cross section is thus predicted to be on the picobarn scale, which happens to be typical for the weak interaction. This suggests that any massive stable particle interacting weakly would be a natural candidate for the dark matter.

Supersymmetry

Entirely independent from this motivation is one provided by the hierachy problem in particle physics. The masses of Standard Model particles receive radiative corrections to their masses from loop diagrams, which are divergent unless we assume that new physics appears to limit these loops at some high energy scale. This can be addressed by fine-tuning the Standard Model, or by introducing a symmetry between fermionic and bosonic fields. This new Supersymmetry (SUSY) introduces a "superpartner" with opposite spin statistics for each Standard Model particle. Since these particles have not yet been seen in accelerators, SUSY must be a broken symmetry up to at least the weak scale, with the lightest supersymmetric particle (LSP) expected to have a mass $\sim$100 GeV.

Nearly all versions of SUSY introduce a new discrete symmetry called R-parity, which is equal to +1 for all Standard Model particles and equal to -1 for their supersymmetric

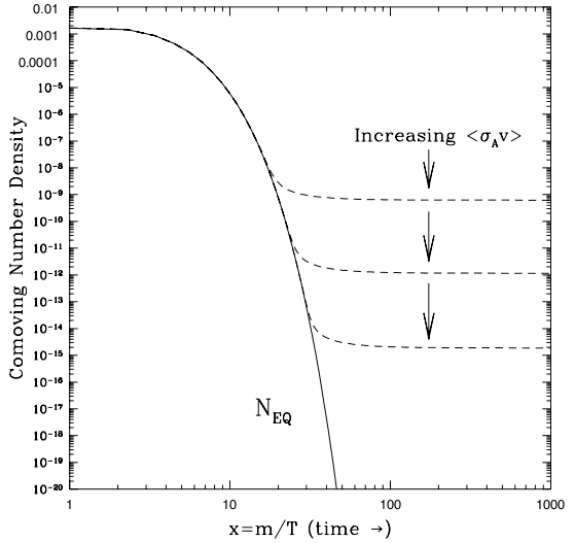

Figure 2.1: WIMP comoving number density as a function of temperature. The equilibrium abundance is shown as a solid curve. Actual abundances for various velocity-averaged annihilation cross sections are shown as dashed curves. Figure from (9).

partners. If R-parity is conserved, the LSP is stable, as it cannot decay to anything with $R = -1$. This makes it a natural dark matter candidate. The favored possibility for the LSP is the lightest neutralino, χ_1^0, a mass eigenstate mixing the bino, the neutral wino, and the neutral Higgsinos, which are all fermionic superpartners to Standard Model gauge bosons.

This happy coincidence of completely independent lines of evidence from cosmology and particle physics is one of the major reasons that WIMPs are considered the most promising and best-motivated dark matter candidates. For this reason, the majority of direct dark matter searches are designed to measure scatters of WIMPs on nuclei of a target material. As SUSY WIMPs have typical masses of the order 100 GeV, SUSY motivates the design of experiments to search for particles in this relatively high mass range.

Hidden sector and asymmetric dark matter

Dark matter may not necessarily exist on the weak scale, and even if it does, its constituent particles may have masses smaller than those predicted by SUSY. Recent "hints" from

several direct detection experiments with potential interpretations as WIMPs with mass $M_\chi < 10\,\mathrm{GeV}$ have led to increased interest in theoretical frameworks predicting WIMPs with these lower masses (10; 11).

Another deep mystery in modern particle physics is the observed baryon-antibaryon asymmetry. The visible universe has an excess of baryons over anti-baryons, typically parameterized in terms of baryon (antibaryon) number density n_b ($n_{\bar{b}}$) and entropy density s, by

$$\eta(b) = \frac{n_b - n_{\bar{b}}}{s}. \tag{2.2}$$

Current estimates put $\eta(b) \sim 10^{-10}$ (12).

One approach is to simultaneously deal with this baryon asymmetry problem and the dark matter problem, linking baryogenesis with the production of dark matter in the early universe. There is no particular reason to believe both of these problems should be solved by the same physics, but it is an attractive possibility that the new physics could be sufficiently minimal and unifying to do so.

Three general scenarios have been proposed linking baryons to dark matter in the early universe. The first proposes that there was a single sector connecting both dark matter and baryons, acting as a parent that generates both through decay, or as a mediator linking the asymmetry between the two. This is the primary approach taken by asymmetric dark matter (ADM) models, to be described below. The other two scenarios either use dark matter as an auxiliary to baryogenesis or relate relic abundances using the thermal WIMP paradigm.

In ADM scenarios (13), the current dark matter abundance is, in analogy with the current baryon abundance, only the surviving asymmetric part of an initial density, and these two asymmetries may be of the same order. If there is a mechanism relating the particle-antiparticle asymmetries of dark matter and baryons, then the relation between their densities suggests a natural dark matter mass scale of

$$\frac{\rho_{\mathrm{DM}}}{\rho_{\mathrm{baryon}}} m_p \approx 5\,\mathrm{GeV}. \tag{2.3}$$

This motivates the design of direct detection experiments to search for dark matter particles in a much lower mass range than SUSY WIMPs. These experiments have targets with lower, more kinematically favorable masses; very low recoil energy thresholds; or both.

2.2 Other candidates

Both SUSY and ADM theories provide compelling motivation to search for WIMPs over a wide mass range, but by no means do they guarantee that these particles form the majority of the dark matter in the universe, or indeed exist at all. While WIMPs continue to be the best-motivated candidates, there are several other plausible ways that the dark matter problem might be solved.

2.2.1 Axions

One relatively good candidate for dark matter is a particle called the axion, motivated by a solution proposed by Peccei and Quinn in 1977 to the "strong CP problem" (14). The Lagrangian of quantum chromodynamics includes a CP-violating term that should give rise to a measurable electric dipole moment for the neutron unless the coefficient of this term is extremely small. The best current upper limit on the neutron electric dipole moment is $|d_n| < 2.9 \times 10^{-26}$ ecm (15), which requires the magnitude of the coefficient of the CP-violating term $|\hat{\theta}| < 0.7 \times 10^{-11}$. The essence of the strong CP problem is that it remains unexplained why this coefficient should be so small. There is no reason that this value should be forbidden, but it can be argued that it would be more "natural" not to have such a finely-tuned, minuscule coefficient in the QCD Lagrangian.

The Peccei-Quinn solution to this problem interprets $\bar{\theta}$ as a dynamic field, adding a new global symmetry that is spontaneously broken shortly after the Big Bang. Different values of $\bar{\theta}$ represent different vacuum states. The vacuum state with minimum potential energy is the one with $\bar{\theta} = 0$, and any other initial value of $\bar{\theta}$ will naturally roll down to 0. A more detailed treatment that includes known weak CP violation finds the potential to have a minimum

at $|\bar{\theta}| \approx 10^{-17}$ (16). The global symmetry broken by the Peccei-Quinn mechanism leads to the production of a new pseudoscalar boson. The axion is thus the Nambu-Goldstone boson (17) associated with the spontaneous breaking of the Peccei-Quinn symmetry.

Axions would be created non-thermally in the early universe as a non-relativistic condensate, and could account for the universe's dark matter if $m_a \approx 10\,\mu\text{eV}$. Axion search experiments in the μeV range are currently underway and are beginning to probe the parameter space of axion models. Since axions interact electromagnetically, experiments like ADMX contain a detection cavity in a magnetic field whose virtual photons would be expected to interact with the axions and produce microwave photons. ADMX has probed a significant part of the theoretical parameter space and found null results for the mass range $1.9\,\mu\text{eV}$ to $3.52\,\mu\text{eV}$ (18). ADMX-Gen2 has been selected by the DOE as a part of the second-generation (G2) dark matter program. This stage of the experiment is considered a "definitive search," as it will have sufficient sensitivity to the axion-photon coupling to either detect the dark matter QCD axion or reject the hypothesis at high confidence.

2.2.2 Neutrinos

Ordinary Standard Model neutrinos are a natural class of non-baryonic dark matter candidates with weak-scale interaction cross-sections. Upon closer inspection, there are a number of problems that preclude their being the dominant component of the dark matter. The first is that they are relativistic, which is in conflict with the argument from structure formation for cold dark matter. Furthermore, we can calculate the present day relic density of neutrinos from thermal freeze-out (as in Sec. 2.1), and find that, to account for the amount of non-baryonic dark matter that has been observed, it must be that $\Sigma_i m_i = 10$ eV. Cosmological observations place an upper limit of $\Sigma_i m_i < 0.67$ eV (19), so neutrinos can make up only a small fraction of the total non-baryonic dark matter.

2.2.3 Baryonic matter

In some sense the most obvious dark matter candidate to consider is ordinary baryonic matter we simply haven't observed. The most common objects considered in this class are called massive compact halo objects (MACHOs) and may consist of hot white dwarfs and black holes. An immediate problem with this candidate is that these MACHOs would be composed of baryonic matter, which violates constraints from BBN and CMB anisotropy studies. Nonetheless, searches for these objects have been conducted using "gravitational microlensing," which consists of observation of a temporary brightening of a star when a compact gravitational lens passes between it and the observer. Results from the 2007 run of the EROS-2 microlensing survey (20) rule out a Milky Way halo composed primariliy of MACHOs with a mass in the range $0.6 \times 10^{-7} < M/M_{\odot} < 15$. For these reasons, MACHOs are strongly disfavored as a major component of the universe's dark matter content.

2.2.4 Modified gravity

Rather than postulating new particles to explain the observed dark matter distributions in the universe, we may consider an entirely alternative explanation – modifications to our understanding of gravity that explain many of these observations and allow for the possibility of a universe free of non-baryonic dark matter. The first modification to Newtonian dynamics (MOND) at very low accelerations was created specifically to produce flat rotation curves (21). Bekenstein has since attempted to transform MOND into a full theory with predictive power (22), but there remain difficulties, particularly at the cluster scale. Observations of the Bullet cluster are especially difficult to reconcile with MOND, as one would expect the lensing to trace the baryonic mass. Angus et al. have proposed a solution combining MOND and neutrino dark matter, using neutrino masses very near the current upper limits. This proposal has not yet been ruled out, but there is a strong consensus in favor of the ΛCDM model, and for the universe having a large component of non-baryonic dark matter.

Chapter 3

Detection of Dark Matter

The discovery of a totally new particle or class of particles calls for many lines of converging evidence, and as such, efforts are underway to study dark matter in four very different ways, each of which may lead to different inferences about the observed phenomena. All of these approaches are anchored by simulation efforts to model galactic halos, large-scale structure, and the dynamical evolution of the universe; and in turn observations should increasingly feed back into improved simulations.

3.1 Indirect detection

Indirect detection usually refers to the search for WIMP self-annihilation products in the cosmos. Prospects for such a detection may initially seem dim, given general arguments about crossing symmetry for scattering amplitudes and the current upper limits on the WIMP-nucleon interaction cross section. However, since these are the same annihilation processes that determined the relic density, they should continue today in regions of sufficiently high dark matter density. As the annhilation rate scales as the square of the number density, we naturally look to regions where the density is at a maximum. Over the age of the cosmological body in question, be it the sun or the galactic center, an excess of WIMPs should have accumulated in numbers sufficient to allow for their indirect detection through

the observation of several proposed annihilation channels.

3.1.1 Cosmic signals from self-annihilation

A variety of cosmic signals are available to us, and while many have large systematic uncertainties, such as poorly contrained line-of-sight density and boost factor, they provide complementary information that contributes to the broader picture. Several of these experiments have published leading upper limits in regions of parameter space less accessible to direct detection experiments.

Gamma rays

Gamma rays may serve as useful tracers of dark matter annihilation, as they retain directional information over galactic distances and are relatively easily detected. In principle, a perfect gamma ray telescope should be able to map out the dark matter distribution in the Milky Way's own halo, as well as pointlike sources from other nearby dark matter halos.

In a simple $\chi\chi \to \gamma\gamma$ annihilation, there would be an observable monoenergetic gamma line somewhere in the GeV–TeV range, a direct tracer of the WIMP mass. Annihilation to other final states is also possible, but final states such as $\gamma\gamma$ and γZ^0 are relatively independent of the WIMP model chosen.

Several complications limit the power of this technique. The branching ratio of neutral WIMPs into a γX final state is relatively low, so the actual rate from many sources may not be visible above continuum backgrounds. Current generations of gamma ray telescopes are also limited in resolution, which makes it even more difficult to distinguish a small, narrow feature above backgrounds. Final states with continuous gamma spectra (such as W^+W^-, hadronic jets, etc.) may have much higher branching ratios, and could appear more clearly above backgrounds, but they are naturally much harder to distinguish from those continuous background sources.

VERITAS and HESS are two ground-based observatories for penetrating gamma rays in the tens of GeV-TeV range. The Large Area Telescope (LAT) on the Fermi Gamma-ray

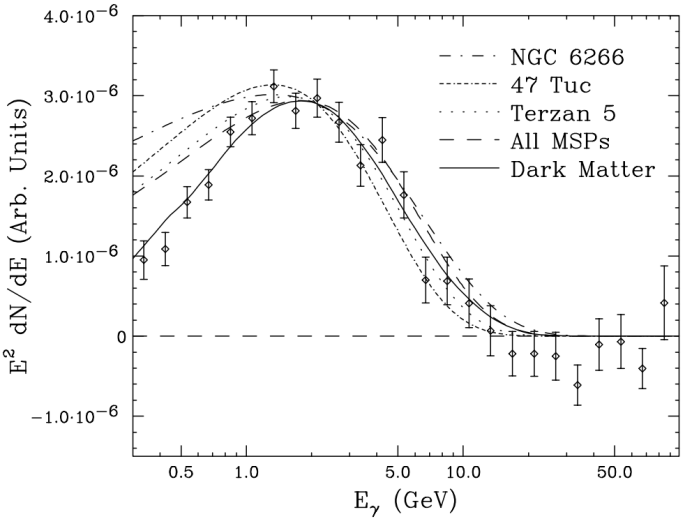

Figure 3.1: Spectral comparison of the gamma-ray excess in Fermi-LAT data as described in (24) to globular cluster measurements, and to the sum of all millisecond pulsars detected by Fermi-LAT as point sources. The spectrum from millisecond pulsars and globular clusters is argued to be consistently softer than that of the observed excess at energies below ∼1 GeV.

Space Telescope ("Fermi") is sensitive to gammas of lower energies. Several analyses of Fermi-LAT data (23; 24; 25) have seen a gamma excess near the galactic center that could be indicative of annihilating WIMPs with mass $M_\chi \sim 30\,\mathrm{GeV}$, shown in Fig. 3.1. It is as yet unclear whether this may instead be fully explained by variations on some other astrophysical phenomenon, such as millisecond pulsars, as considered in (26).

Fermi data has also led to the observation of a line at ∼130 GeV, shown in Fig. 3.2, with an initially reported significance of 3.2σ (27). This could be interpreted as evidence of dark matter annihilations through various channels with $M_\chi \approx 130\,\mathrm{GeV}$ or $260\,\mathrm{GeV}$. After further analysis with more data, the significance of this result has dropped and is now within the 2σ uncertainty band of the continuum.

Cosmic rays

If WIMP annihilation leads to high-energy charged particles, these cosmic rays might be visible in excesses in the antimatter-to-matter ratio at high energies. The measured flux

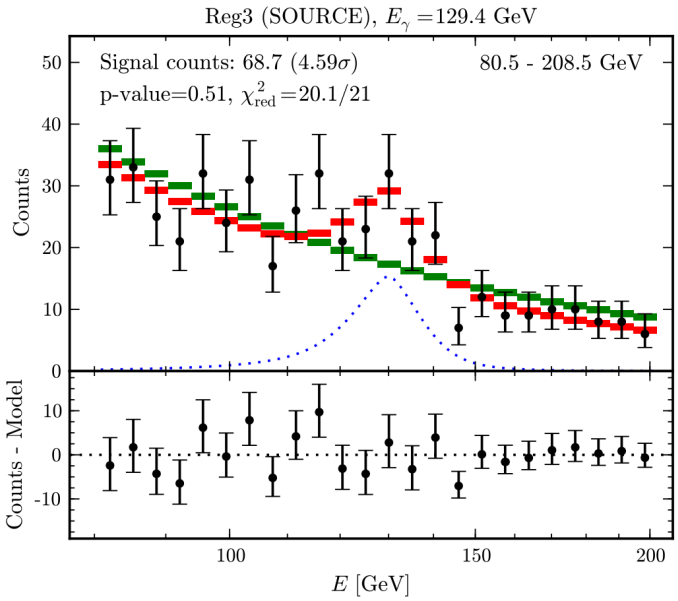

Figure 3.2: (top panel) Measured events in Fermi data with statistical error bars. Horizontal bars show best-fit models with and without dark matter, colored red and green, respectively. (bottom panel) Residuals after subtracting the model with ∼130 GeV line contribution. Figure from (27).

of cosmic rays is generally composed of far more electrons than positrons. Since WIMP annihilation should produce both in equal numbers, the positron fraction can be used to trace WIMP annhiliation. This approach faces many difficulties, including the loss of directional information of charged particles traveling through long distances, and the fact that several other processes could also produce e^+e^- pairs in the same locations where WIMP annihilation signals are sought.

Solar neutrinos

As the sun moves through the dark matter halo, WIMPs may interact with nucleons in the sun and lose momentum. Over the lifetime of the sun, many such interactions would be expected to take place, resulting in the accumulation of a population of WIMPs gravitationally bound inside the sun. The self-annihilation rate of these particles increases as the square of the increasing density, and models generally predict that an equilibrium between the capture and annihilation rates should be reached over the current solar lifetime, assuming the capture rate and annihilation cross sections are sufficiently large. WIMP annihilations proceeding by $\chi\chi \to b\bar{b}$ or $\chi\chi \to W^+W^-$ would result in further leptonic decays that include neutrinos as decay products. These neutrinos escape the sun with very little absorption, and could represent a strong indirect signal for WIMPs.

One useful feature of detection via solar neutrinos is that it is largely independent of the halo parameters. As the sun travels through the galactic halo over billions of years, the halo is sampled at many points throughout the galaxy. This has the effect of averaging out any possible structure in the halo. Therefore, for a given set of WIMP mass and properties, one can make a clear prediction of the signal rate in a neutrino telescope, with no detailed assumptions about halo structure. By comparison, searches for photons resulting from WIMP annihilations depend the contentious "cuspy" structure of the halo near the galactic center.

The most prominent example of this detection strategy is IceCube, an ice Cherenkov detector embedded in the glacier at the geographic South Pole. In a search for neutrinos from

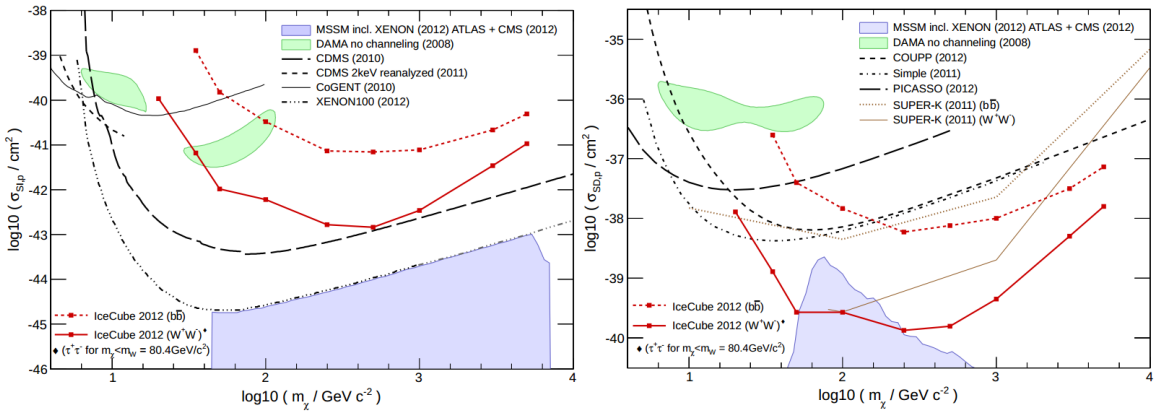

Figure 3.3: IceCube 79-string analysis, 90% CL upper limits on spin-independent (left) and spin-dependent (right) WIMP-proton cross section for "hard" (W^+W^-) and "soft" ($b\bar{b}$) annihilation channels vs WIMP mass m_χ. Figure from (28).

$\chi\chi$ annihilations in the sun (28), IceCube has published modest upper limits on the spin-independent WIMP-proton cross section (Fig. 3.3, left panel). Assuming the hard (W^+W^-) decay channel, their simultaneously published limits on the spin-dependent WIMP-proton cross section are world-leading for $m_\chi \gtrsim 30\,\mathrm{GeV}$ (Fig. 3.3, right panel).

Over 80% of the nucleons in the sun are protons, while the target materials of direct detection experiments contain more neutrons than protons. For spin-independent scattering, it is generally assumed that the WIMP's coupling to protons and neutrons is approximately the same (Sec. 3.3.1). If this is not the case, direct comparisons as in Fig. 3.3 are not so straightforward.

3.2 Production in colliders

With the discovery of the Higgs boson at CERN's Large Hadron Collider (LHC) and the "completion" of the Standard Model, the next goal for accelerator-based experiments is to look for physics beyond the Standard Model. Our observational evidence for dark matter has long been among the clearest signs that there is likely yet much to discover. Accelerators have been fertile discovery grounds for new particles, and with the LHC reaching the TeV range, the region of electroweak symmetry breaking is finally becoming accessible. A whole

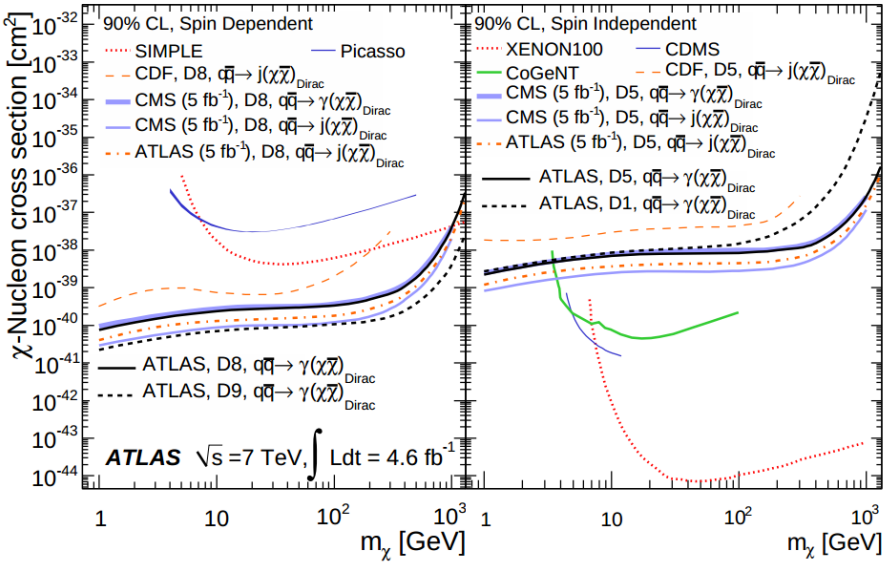

Figure 3.4: CMS and ATLAS 90% CL upper limits on the spin-dependent (left) and spin-independent (right) WIMP-nucleon cross section as a function of m_χ, for several production channels. Figure from (29).

host of new particles associated with supersymmetry or other new physics could be found, and it is possible that dark matter could be closely tied to these first discoveries.

Colliders have an advantage in that their constraints on WIMP mass and WIMP-nucleon coupling are independent of the parameters of the various dark matter halo models, all of which have significant uncertainties in their density and velocity distributions. Studying dark matter properties using colliders has its own challenges, and there is of course no direct verification that any new particle discovered is what actually makes up most of the dark matter in the Universe. Collider production is thus considered a complementary strategy to direct detection, with both expected to provide important evidence as the picture is pieced together. At the LHC, the CMS and ATLAS detectors have produced competitive limits on the WIMP-nucleon cross section for spin-dependent interactions, and modest limits on spin-independent interactions, shown in Fig. 3.4.

3.3 Direct detection

Direct detection experiments are designed to search for elastic scattering of dark matter particles off atomic nuclei. These interactions are expected to occur at a very low rate that is dependent on the local density and velocity profile of the galactic dark matter halo, the properties of the target nuclei, and details of the WIMP-nucleus coupling. This is the detection strategy employed by CDMS, and will henceforth be the focus of discussion.

3.3.1 WIMP-nucleus scattering

The thermal equilibrium argument for weak-scale WIMP interactions (Sec. 2.1) allows us to make an approximation for the event rate expected in a direct detection experiment. Crossing symmetry implies that the scattering process $\chi q \to \chi q$ should have a cross section of the same order of magnitude as that predicted for $\chi\chi \to q\bar{q}$, namely $\sigma_{\chi\chi} \sim 1\,\mathrm{pb} = 10^{-36}\,\mathrm{cm}^2$. Using the standard value of 0.3 $\mathrm{GeV}/c^2/\mathrm{cm}^3$ for the local WIMP density and a velocity $\sim 10^{-3}c$, we can predict that 100 GeV WIMPs passing through the Earth would interact with one kilogram of hydrogen a few times a day. This leads to a general detector philosophy: there will be at most a few interactions per kg-day, so a direct detection experiment that hopes to positively identify WIMP interactions should have a low background event rate.

WIMPs are expected to scatter elastically off nuclei. Since a particle of mass $100\,\mathrm{GeV}/c^2$ with velocity $10^{-3}c$ has DeBroglie wavelength $\lambda = h/M_\chi v \approx 12\,\mathrm{fm}$, the interaction happens coherently over the entire nucleus. From simple considerations of conservation of momentum and energy, an elastic collision of a WIMP with kinetic energy E_χ on a nucleus will deposit a maximum energy E_R in a recoiling target, given by

$$\frac{E_R}{E_\chi} = \frac{4Mm}{(M+m)^2}. \tag{3.1}$$

When averaged over recoil angles, the mean kinetic energy deposited is one half this amount. So a 100 GeV WIMP with a kinetic energy of ∼40 keV, characteristic of galactic speeds,

would deposit ∼20 keV in the lattice by scattering off a 67 GeV germanium nucleus. By contrast, the same WIMP scattering with an electron would deposit ∼0.5 eV. This is not enough to produce a single electron-hole pair in Ge. Thus electron recoils from WIMPs are not detectable with CDMS detectors, so CDMS and other direct detection experiments search for WIMP-induced nuclear recoils.

WIMPs in the galactic halo have small velocities $\sim 10^{-3}c$, which strongly affects the nature of their interaction with nuclei. A typical 60 GeV WIMP has a deBroglie wavelength $\lambda_\chi = h/M_\chi v$ of about 20 fm, comparable to the size of a fairly large atomic nucleus. This means that the interaction between the WIMP and the nucleus does not resolve the individual nucleons. Instead, their individual scattering amplitudes will be added, contructively or destructively, in calculations of the scattering cross section.

In the non-relativistic limit, the WIMP-nucleon scattering amplitude can be simplified to include only the scalar and axial-vector terms in the interaction Lagrangian. Kurylov and Kamionkowski have shown (30) that in this limit the general interaction is characterized by only five parameters: the WIMP mass M_χ, the spin-independent (SI) couplings to the proton and neutron f_p and f_n, and the spin-dependent (SD) couplings a_p and a_n:

$$\mathcal{L}_{\chi N} \approx 4\chi^\dagger\chi\left(f_p\eta_p^\dagger\eta_p + f_n\eta_n^\dagger\eta_n\right) + 16\sqrt{2}G_F\chi^\dagger\frac{\vec{\sigma}}{2}\chi\cdot\left(a_p\eta_p^\dagger\frac{\vec{\sigma}}{2}\eta_p + a_n\eta_n^\dagger\frac{\vec{\sigma}}{2}\eta_n\right) \tag{3.2}$$

Here χ is the WIMP wave function, η are the neutron and proton Weyl spinors, and $\vec{\sigma}$ is the spin operator.

We can consider special cases of this more general form where some of the terms are zero, as in the case of totally spin-independent scattering (left term in Eq. 3.2 only), or spin-dependent scattering (right term in Eq. 3.2 only).

Spin-independent scattering

The simplest case of SI scattering is one in which the momentum transfer q is nearly zero. This is equivalent to zero recoil energy E_R, as $q = \sqrt{2M_TE_R}$ for a target of mass M_T. In this case the scattering amplitudes add perfectly coherently, with the total amplitude

proportional to the coupling constants f_p and f_n scaled by the number of protons Z and neutrons in the nucleus of atomic mass A. The cross section involves a kinematic factor depending on the reduced mass of the interaction, $\mu_{\chi N} = \frac{M_\chi M_N}{M_\chi + M_N}$, and is simply the square of the amplitude,

$$\sigma_{\rm SI} = \frac{4}{\pi}\mu_{\chi N}^2 \left(Z f_p + (A - Z) f_n\right)^2 . \tag{3.3}$$

Under the standard assumption that $f_p \approx f_n$, the cross section is proportional to the square of the atomic mass A. This coherent enhancement effect is a major motivation to use a target medium composed of heavy nuclei when searching for spin-independent interactions. For example, $A^2_{\rm Si} \approx 700$, while $A^2_{\rm Ge} \approx 4500$.

The general form for the recoil energy spectra from such an interaction is a featureless falling exponential as a function of increasing recoil energy (31):

$$\frac{dR}{dE_R} = \frac{R_0}{E_0 r} e^{-E_R/E_0 r} \tag{3.4}$$

where R is the event rate per unit mass, R_0 is the total event rate, E_0 is the most probable incident kinetic energy for a WIMP, and r is the kinematic factor from the righthand side of (3.1). In order to find the total rate, we simple integrate from the energy threshold of the experiment E_T to arbitrarily high energies.[1] The resulting total rate is $R \approx R_0 e^{-E_T/E_0 r}$.

In a realistic case, the momentum transfer q is not zero, so the individual WIMP-nucleon scattering amplitudes do not add perfectly coherently across all nucleons. As the momentum transfer increases, the wavelength $\hbar/q$ decreases, until it becomes smaller than the nuclear radius. At this point the nucleus is no longer seen as a coherent whole. Consequently the cross section is reduced with increasing q, as characterized by a nuclear form factor $F(qr_n)$, where r_n is an effective nuclear radius. This factor represents the Fourier transform of the density distribution of neutrons and protons in the nucleus, normalized to lie between 0 and

[1] A more detailed numerical calculation of these differential and integrated rates is presented in Sec. 8.6, where a small resonance feature is found in the Si recoil spectrum that helps to constrain the systematic uncertainty in the energy scale for nuclear recoils.

1. From fits to muon scattering data, r_n can be modeled as

$$r_n^2 = c^2 + \frac{7}{3}\pi^2 a^2 - 5s^2, \tag{3.5}$$

where c, a, and s are empirically estimated as

$$c \approx (1.23A^{1/3} - 0.60)\text{fm} \qquad a \approx 0.52\,\text{fm} \qquad s \approx 0.9\,\text{fm}. \tag{3.6}$$

An analytical approximation of the nuclear form factor commonly used (31; 2) to calculate recoil spectra is that proposed by Helm (32), an exponentially suppressed spherical Bessel function of the first kind:

$$F(qr_n) = 3\frac{j_1\left(qr_n\right)}{qr_n}e^{(qs)^2/2} = 3\frac{\sin\left(qr_n\right) - qr_n\cos\left(qr_n\right)}{\left(qr_n\right)^3}e^{(qs)^2/2} \tag{3.7}$$

The differential WIMP-nucleus cross section, now a function of this non-zero momentum transfer, can be represented as

$$\frac{d\sigma_{\text{SI}}}{dq^2} = \frac{4}{\pi}\mu_{\chi N}^2\left(Zf_p + (A-Z)\,f_n\right)^2 F^2(q). \tag{3.8}$$

Examples of this form factor for some commonly used detection materials are shown in the left panel of Fig. 3.5. The suppressed form factor for heavier targets works against the coherent enhancement A^2 factor. This can be seen in the right panel of Fig. 3.5, which shows the total spin-independent scattering rate as a function of energy threshold. This demonstates that for heavy targets like Xe to be effective in a search for spin-independent WIMP-nucleus scatters, a low energy threshold is optimal.

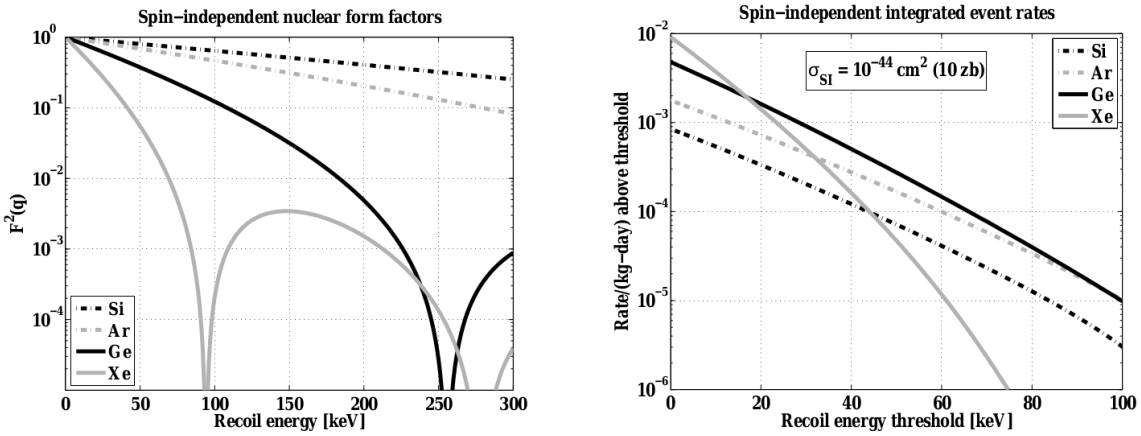

Figure 3.5: (left) Helm form factors for the most abundant isotope of four common detection materials. (right) Spin-independent integrated event rates for a 100 GeV WIMP with cross section $\sigma_{\rm SI} = 10^{-44}{\rm cm}^2$ (2).

Spin-dependent scattering

In the case of spin-dependent WIMP-nucleon interactions, the zero momentum transfer limit of the cross section is

$$\sigma^0_{\rm SD} = \frac{32(J+1)}{\pi J} G_F^2 \mu^2 \left[a_p \langle S_p \rangle + a_n \langle S_n \rangle\right]^2 \tag{3.9}$$

where J is the nuclear spin and $\langle S_p \rangle$ and $\langle S_n \rangle$ are the expectation values of the proton and nuclear spins. The expectation values must be evaluated numerically from nuclear spin structure calculations. In general, $a_p \not\approx a_n$.

The spin-dependent term in the Lagrangian looks similar to the spin-independent term, but with amplitudes that contain spin inner products so that the sign of the spin matters. Most nucleons in a nucleus are aligned in spin-singlet pairings, such that each pair has both a positive and negative contribution to the amplitude. Not only is there no coherent enhancement effect for high-A materials, spin-paired nucleons destructively interfere, leaving only odd unpaired nucleon contributions to the cross section. For this reason, spin-dependent cross sections are optimized for targets with the most unpaired nucleons per kg.

For CDMS, the only Si isotope with a non-zero nuclear spin is ^{29}Si ($J = 1/2+$), though

it has only ∼4.7% abundance in natural Si. The only naturally occuring Ge isotope with non-zero nuclear spin is ^{73}Ge ($J = 9/2+$), at ∼7.8% natural abundance. As it has a higher nuclear spin and greater natural abundance than the corresponding Si isotope, CDMS is most sensitive to spin-dependent scatters on the ^{73}Ge atoms in each Ge detector.

It is beneficial to use a variety of detection media to explore this relatively unknown parameter space. Natural xenon contains two non-zero spin isotopes, ^{129}Xe ($J = 1/2+$) and ^{131}Xe ($J = 3/2+$), with an abundance of 26.4% and 21.2%, respectively. Direct detection experiments using Xe targets are thus somewhat more sensitive to spin-dependent interactions than those using Ge. Fluorocarbons tend to have even better sensitivity per kg. Fluorine (^{19}F) has an unpaired proton ($J = 1/2+$), and even ∼1.1% of natural carbon has an unpaired neutron ($J = 1/2-$). These materials are used by bubble chamber experiments such as COUPP and PICASSO. These two collaborations have merged to form PICO, the next generation of which (PICO-250L) will have the sensitivity to set much stronger limits on spin-dependent WIMP interactions than any other current or proposed direct detection experiment.

3.3.2 Annual and Sidereal modulation

Current models of the Milky Way's dark matter halo have virtually no rotational component, while the galactic disk itself is clearly rotating. The result is a "WIMP wind" on Earth as the solar system passes through the halo, shown in the left panel of Fig. 3.6. Because of the Earth's orbital motion around the sun, the relative velocity of this WIMP wind on Earth varies throughout the year. In June, the Earth is moving most quickly upwind, and terrestrial WIMP-search counting detectors should see an increase in their rates. Conversely, when moving most quickly downwind in December, the rate should be lowest.

In a completely background-free experiment, a sinusoidal annual modulation of the event rate would be powerful evidence that WIMPs had been scattering in the detector. No real experiment is completely background-free, and many background signals, such as radioactivity levels in the surroundings, environmental temperature and pressure, water

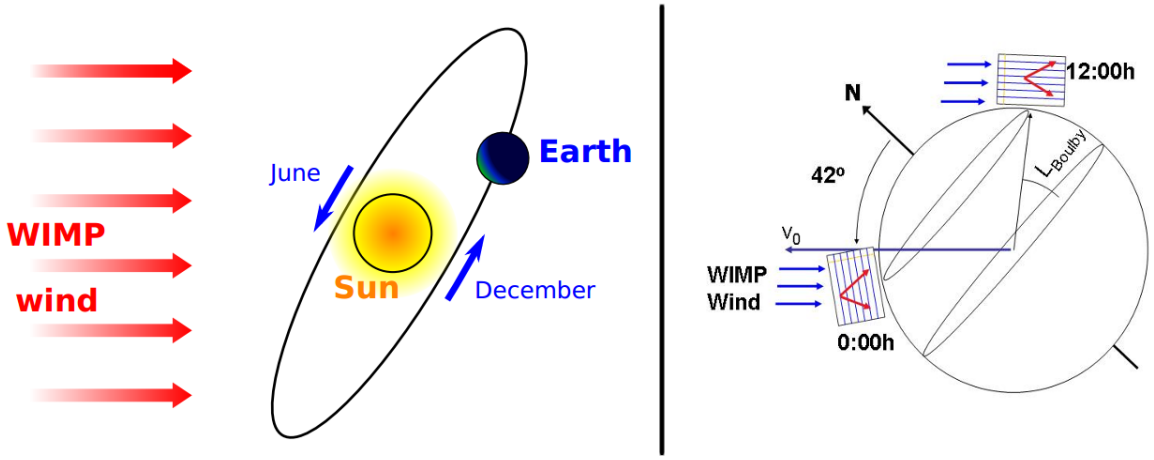

Figure 3.6: (left) A schematic image of the relative velocity of the sun and Earth relative to the dark matter halo. The Earth's orbit is inclined at $\sim$ 60 deg from the plane of the galactic disk. Image from (35). (right) A depiction of diurnal modulation of WIMP scattering direction over a sidereal day at 42° N latitude.

table variation, and incident muon flux, also exhibit some degree of annual modulation and could influence the final event counting rate. It is very difficult to completely isolate these factors, and while there have been results from DAMA/LIBRA (33) and CoGeNT (34) that are compatible with WIMP interpretations, remaining potential background systematics have prevented these results from being widely accepted as evidence of terrestrial WIMP scatters.

Any detector on the Earth's surface will also experience sidereal variations in the WIMP wind as the Earth rotates, shown in the right panel of Fig. 3.6. Since background variations generally track with solar days, detectors able to detect sidereal variations in track direction are less prone to systematic uncertainties.

Since gas chamber detectors have lower target density than most other detection media, their tracks for WIMP-nucleus scatters should be macroscopic. One such search, the DMTPC experiment, has a target medium of CF_4 gas. Signals from scintillation and drift electrons are measured using CCDs and PMTs. Preliminary surface runs have demonstrated the ability to reconstruct energy and track vectors for nuclear recoils. The recoil energy and

track length are dependent on the incident particle type, so these parameters can be used to discriminate against electromagnetic and alpha backgrounds. As these detectors have low density by design, light nuclides like fluorine with unpaired nucleons can be used to provide sensitivity to spin-dependent interactions. Since the low density makes it more difficult to attain large exposures, these are no longer considered discovery detectors. However, they will become more important if no signals are found in nuclear recoil counting experiments at the irreducible background of coherent neutrino scattering (36; 37).

3.3.3 Direct detection technologies

There are presently three primary classes of direct detection technologies in use, distinguished from each other and within their own class primarily by their target material and the signal channels made available by the properties of that target. Solid-state semiconductor crystals were the first to be developed, but detectors using noble liquids have rapidly caught up and have now published the strongest upper limits on spin-independent WIMP-nucleon cross section in the 10-100 GeV/c^2 WIMP mass range.

Solid-state detectors

The largest background for any search for rare nuclear recoil events are electron recoils produced by natural radioactivity in the experimental apparatus and environment. Solid-state detectors have excellent energy resolution to aid in identifying the sources of this background, and to subtract it if necessary. Many of these detectors include multiple signal channels to provide excellent discrimination against electron recoils. In CDMS, this discrimination power comes from the simultaneous measurement of ionization and athermal phonons, since nuclear recoils produce much less ionization than electron recoils of the same energy (sometimes called "quenching"). This clearly separates the two populations down to recoil energies of less than 10 keV.

EDELWEISS, like CDMS, uses Ge crystals operated at cryogenic temperatures and identifies ionization and heat response. Rather than measuring athermal (out-of-equilibrium)

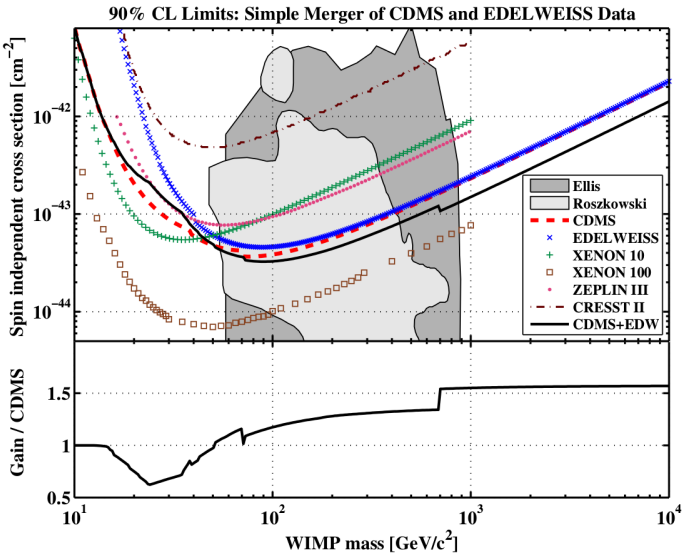

Figure 3.7: **Top**: 90% CL upper limits on the spin-independent WIMP-nucleon cross section vs WIMP mass. (red dashed) CDMS II (42), (blue crosses) EDELWEISS (43), (black line) merged CDMS-EDELWEISS limit (41). **Bottom**: Improvement vs the CDMS II limit. The combination is stronger only above WIMP masses $M_\chi \approx 50\,\mathrm{GeV}/c^2$. The gain reaches a maximum of 1.57 above $700\,\mathrm{GeV}/c^2$.

phonons, EDELWEISS measures thermal phonons, in the form of a small temperature change of the entire crystal. The ionization detection system has many similarities with CDMS. The most recent SuperCDMS iZIP detectors use interdigitated ionization electrodes similar to the design first implemented by EDELWEISS (38). This design was itself inspired by an early design developed by the CDMS collaboration (39). Interdigitated electrode design allows extremely strong rejection of surface electron recoils (40). CDMS and EDELWEISS observations have been combined into a single spin-independent upper-limit (41). Shown in Fig. 3.7, it is stronger than either individual limit above WIMP masses of $50\,\mathrm{GeV}/c^2$, up to a factor 1.57. Further collaboration, even to the extent of a mixed detector payload, is under consideration as SuperCDMS moves to its future site at SNOLAB.

CRESST uses a $CaWO_4$ target instrumented with two tungsten superconducting transition edge sensors (TES). One measures the thermal phonon signal, like EDELWEISS, as a rise in the temperature of the scintillating crystal. The other monitors the temperature of a

Si wafer that absorbs scintillation light. EURECA is a planned dark matter search uniting the CRESST and EDELWEISS collaborations, and as such CRESST-style scintillation detectors are also under discussion as a way to increase target diversity within a SuperCDMS SNOLAB tower.

CoGeNT uses ultra-low-noise p-type point contact (PPC) Ge detectors with ionization readout only (44). The low-capacitance charge electrode design allows for very good ($\sim$70 eV) energy resolution at zero energy, with an electron recoil threshold of 0.5 keV. CoGeNT has reported an excess of events below 3 $\mathrm{keV_{ee}}$ that may be consistent with dark matter interactions (45), as well as an annual modulation signal at 2.2σ significance, though its modulation amplitude is $\sim$4-7 times larger than predicted for a standard WIMP halo (46).

Noble liquids

A newer, broad class of experiments based on noble liquid target materials uses rejection techniques that are conceptually similar to those of CDMS, though the signal channels themselves are quite different.

Dark matter searches move forward by increasing exposure while limiting backgrounds. Maximizing livetime can help, but the best way to increase exposure is to increase the target mass. Detectors based on a liquid target mass are conceptually simple to scale up in mass simply because the sensitive material is in the liquid state. The leading noble liquid detectors are dual-phase time-projection chambers, with large tanks holding liquefied Xe (LUX, XENON, ZEPLIN) or Ar (DarkSide), with a gas phase at the top of the chamber. Particle interactions in the liquid excite and ionize the target atoms. Photomultiplier tubes (PMT) measure the primary scintillation light signal (S1). An applied electric field of $\sim$1 kV/cm drifts the ionized electrons up to the gas phase, where they produce a secondary scintillation signal (S2). Much like CDMS, these experiments use the ratio of these two signal channels to discriminate against electron recoil backgrounds. The S1 signal can also be used in pulse-shape discrimination. S1 pulses from electron recoils have longer tails than

those from nuclear recoils, as nuclear recoils primarily excite target atoms into an excimer state with a shorter time constant. This pulse-shape rejection parallels phonon pulse timing parameters used by CDMS to reject surface electron recoils, discussed in Sec. 6.3.1.

Chapter 4

CDMS Overview

The CDMS experiment uses solid state detectors instrumented on semiconductor substrates operated at cryogenic temperatures to look for elastic scatters of WIMPs on the Si and Ge nuclei. This chapter details the experimental configuration of the five-tower CDMS II experiment during the 2006 to 2008 data runs.

4.1 Installation

The CDMS II experiment is installed at the Soudan Underground Laboratory in northeastern Minnesota. The laboratory is located at the deepest level of an iron mine, at a depth of 714 m below the surface. Other experiments hosted at this level include the MINOS neutrino oscillation experiment, and the CoGeNT dark matter search experiment. CDMS II is located in the cavern formerly occupied by the Soudan 2 proton decay search experiment, to the west of the MINOS cavern, as in Fig. 4.1

The chief advantage of this underground location is the dramatically reduced atmospheric muon flux at this depth. At the surface, some of these muons would interact with nuclei in the material near the detectors, producing neutrons that could leave signatures in the detectors similar to the signal expected from a WIMP interaction. The rock overburden at the Soudan Underground Laboratory provides 2090 meters of water equivalent shielding

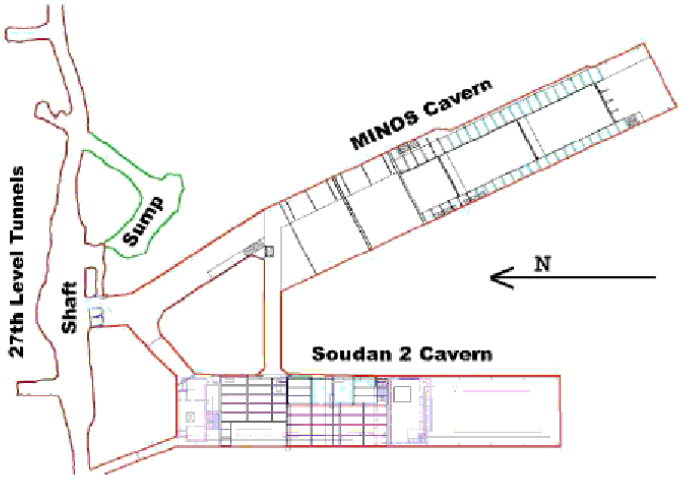

Figure 4.1: Map of the Soudan Underground Laboratory on the 27th level of the Soudan Mine. CDMS II is installed in the former Soudan 2 cavern, to the west of the MINOS cavern.

from this radiation. The resulting muon flux is reduced relative to that at the surface by a factor of 5×10^4, with a consequent reduction of cosmogenic neutron flux due to daughter particles of this cosmic radiation.

4.2 Shielding

Much like any other rare event search experiment, the shielding system to protect the CDMS II detector cold volume ("icebox") from unwanted particle interactions is of primary importance. This sytem involves several layers and incorporates both active and passive shielding technologies.

4.2.1 Muon scintillator veto

Even with the highly reduced muon flux half a mile underground, a population of higher-energy cosmic ray muons does penetrate through the 2090 mwe overburden and impinge on the shielding, producing neutrons with energies of a few MeV, which can result in nuclear

recoils in the detectors.

The outermost layer of shielding consists of an active veto system used to identify and reject any remaining muon flux that has passed through the full rock overburden. It consists of 40 plastic scintillator panels in an overlapping arrangement that surrounds the entire experimental configuration (see Figs. 4.2, 4.4a, 4.4b). Scintillation photons produced as a muon passes through the panel are sent down acrylic light guides to photomultiplier tubes, which are periodically calibrated and monitored by taking "pulser" runs in which a blue light source in each panel is pulsed and the amplified signals are recorded.

Muons can be easily identified in the veto panel signal. Each panel is 5 cm thick. Downgoing minimum ionizing muons typically deposit 10 MeV, and can be distinguished from gammas, which generally deposit a maximum of ∼2.6 MeV. The average muon rate on the entire apparatus is one muon per minute. The activity rate in a veto panel, mostly from radiogenic gammas, is ∼400 Hz for the 5-tower runs at Soudan. A global trigger is issued by the veto system if two panels register a hit in the same history buffer window. The rate of veto-triggered events was fairly constant, shown for the last 5-tower runs (numbered 125-128) in Fig. 4.3). The efficiency of tagging muon events and the overall estimate of the cosmogenic neutron background event rate in the WIMP-search data are discussed in Sec. 6.2.1.

4.2.2 Passive shielding

Five distinct layers together compose the passive shielding system: two layers of polyethylene, two layers of lead, and a mu-metal shield. The outermost passive shielding is a layer of polyethylene bricks, 40 cm in thickness, intended to shield against neutrons by moderating their energies.

Next are the two lead layers, designed to block gamma particles arising from natural radioactivity in the rock and other material surrounding the experiment. The 17.8 cm outer layer is naturally contaminated by the beta-emitting isotope ^{210}Pb ($\tau_{1/2} = 22.3$ yr), part of the ^{238}U decay chain. The inner layer is 4.4 cm of "ancient" lead, built from lead ingots

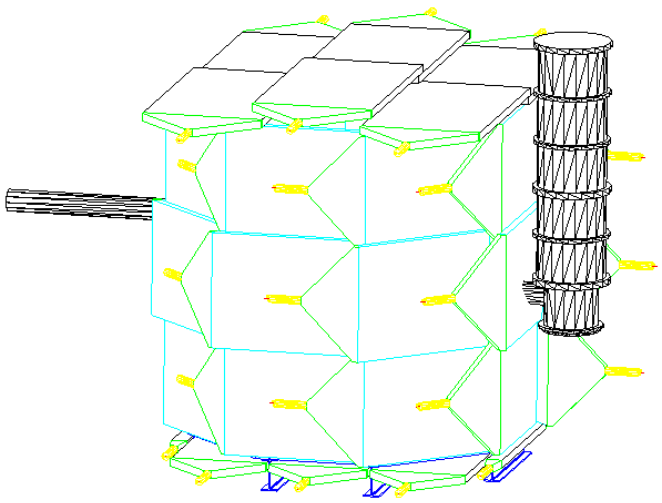

Figure 4.2: The array of scintillator panels composing the outermost layer of shielding. Each rectangular panel consists of a 5 cm thick slab of Bicron BC-408 plastic connected via offset triangular segments to either one or two 2 in Hamamatsu R329-02 PMTs. Adjacent panels overlap, and the top panels extend well beyond the sides to minimize the lack of coverage due to spacing between the tops of the side panels and the top panels themselves. There is no direct line of sight to the detectors through the uncovered areas.

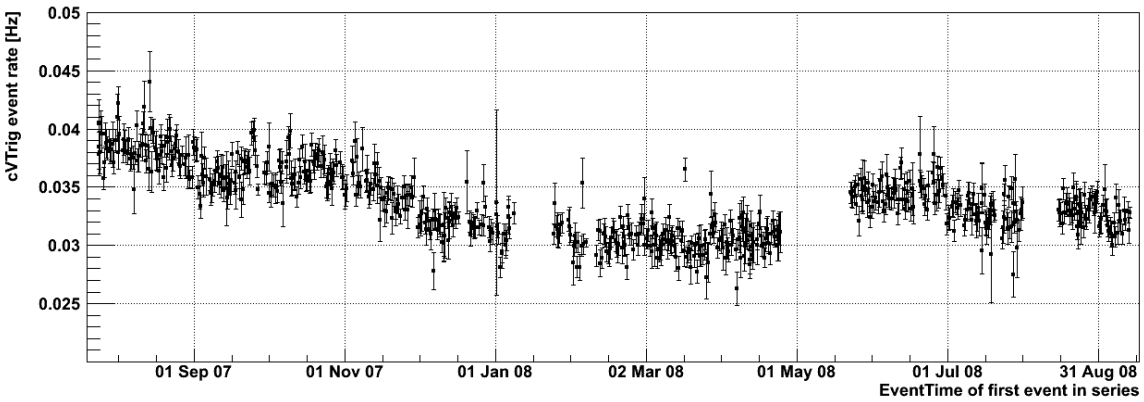

Figure 4.3: Rate of veto-triggered events in Runs 125-128. The rate is relatively stable and no extreme outlier periods are observed.

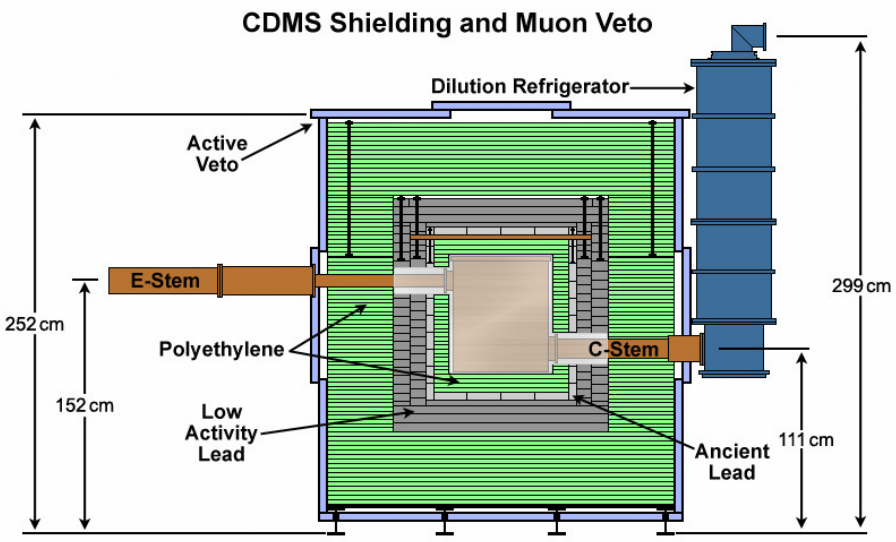

(a)

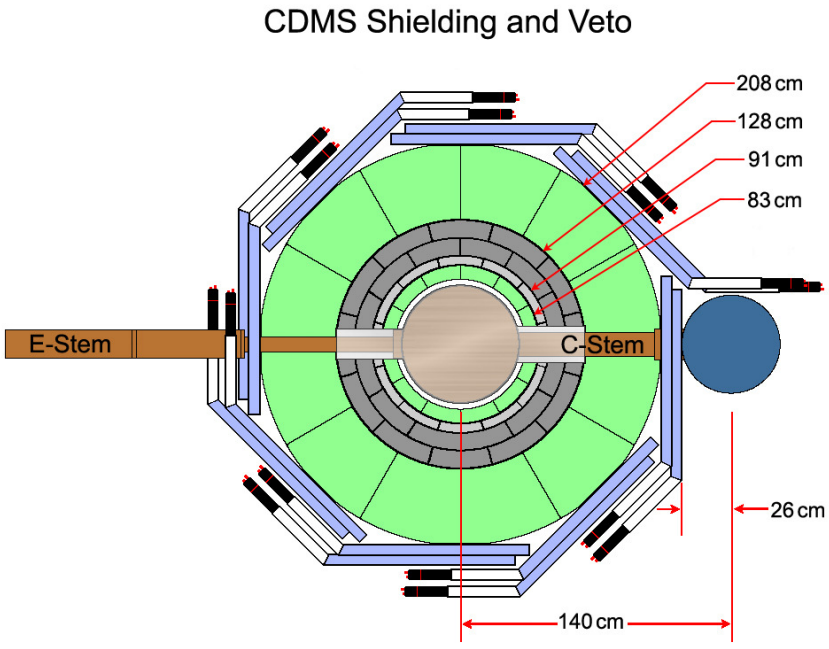

(b)

Figure 4.4: Diagram showing (a) side and (b) top view of the muon veto and inner layers of passive shielding. The veto panels are shown as the outermost, staggered layers (cyan), surrounding the outer circular layer of polyethylene (green), followed by a thinner layer of low-radioactivity lead bricks (gray), an even thinner inner layer of ancient lead (light gray), an inner polyethylene shield (green), and finally a mu-metal shield surrounding the copper icebox (silver). The mu-metal shielding is connected to the "E-stem" and "C-stem," which pass through all layers of shielding and connect to the electronics readouts and the dilution refrigerator, respectively.

harvested from the ballast of an 18th century shipwreck in waters off the coast of France. Its very low ^{210}Pb content makes it an excellent shield for both environmental gammas and radioactivity coming from the outer layer of lead. An analysis of a Monte Carlo simulation of the CDMS II gamma background conservatively estimated the total contamination in the lead shielding from the ^{238}U decay chain at 5.925 mBq/kg (47).

Just inside the lead is a second layer of polyethylene. It has a thickness of 10 cm on all sides but the top, which has a thickness of 7.6 cm. This layer suppresses any cosmogenic neutrons from the lead layers. It is thin enough that it does not significantly increase the gamma flux at the detectors.

The final layer of shielding is a nickel-iron alloy (mu-metal) shield surrounding the copper cans that house the detectors. Unlike the other layers, this shield is not intended to reduce a particle flux, but instead to block any external magnetic fields that could impact the operation of the SQUIDs, thus introducing noise on the readout channels. The current shielding has been shown to reduce the ambient magnetic field by approximately two orders of magnitude.

Inside the shield, the icebox itself is composed of a series of copper cans, each heat-sunk to a different temperature-stage of the dilution refrigerator. In order of decreasing radius and temperature, these stages are the following: room temperature (300 K), nitrogen shield (77 K), helium bath (4 K), still ($\sim$1 K), cold plate ($\sim$130 mK) and mixing chamber ($\sim$40 mK). Detector housings and most of the cold hardware inside the icebox are made from high-purity copper, limiting radioactive contamination near the detectors. The total thickness of this surrounding copper is a few cm, which is sufficient to block alpha and beta particles from entering the cans.

One disadvantage of the underground location is that radon concentration in the air is higher ($\sim$700 Bq m^{-3}) than at the surface. During the first CDMS run at Soudan in 2003, it was found that when air was present inside the lead shield the gamma background increased by a factor of 4 or greater. To counteract this, a continuous purge of dry nitrogen gas has been used to keep the radon-rich mine air from entering the shielding at any point

interior to the lead layers. The purge gas enters between the inner polyethylene layer and the mu-metal shield. Layers further interior, the copper icebox "vacuum cans," are held under vacuum and require no nitrogen purge.

4.3 Cold hardware

Immediately proximate to the detectors themselves are the support structures, wiring, and amplifiers. A simplified view of this arrangement is shown in Fig. 4.5, which depicts the tower hardware stack used for CDMS II runs at Soudan. Fig. 4.6 is a top-down interior view of the vacuum cans inside the icebox.

4.3.1 Detector housing

Each detector is mounted inside its own high-purity copper hexagonal housing using a set of six flat Circlex clamps. These are grouped into stacks of six and mounted within a tower structure (see Sec. 4.3.2). Having no lids, the housings allow adjacent detectors full view of opposing faces. This results in a large fraction of events interacting and triggering in both detectors, particularly in the case of events due to surface contamination. As a WIMP would be expected to scatter only once, these events can be rejected relatively easily in the analysis stage.

The connection between the detector and the readout electronics is made by a detector interface board (DIB) located at the edge of the housing. The coupling to the detector is made through ten aluminum wirebond connections. On the external end, the DIB plugs into one end of a side coax (see Sec. 4.3.3). The DIB is also the installation site for two infrared LEDs used to improve detector neutralization by clearing trapped charges between data series. Each LED shines on the phonon sensor face of its attached detector and the ionization electrode face of the adjacent detector.

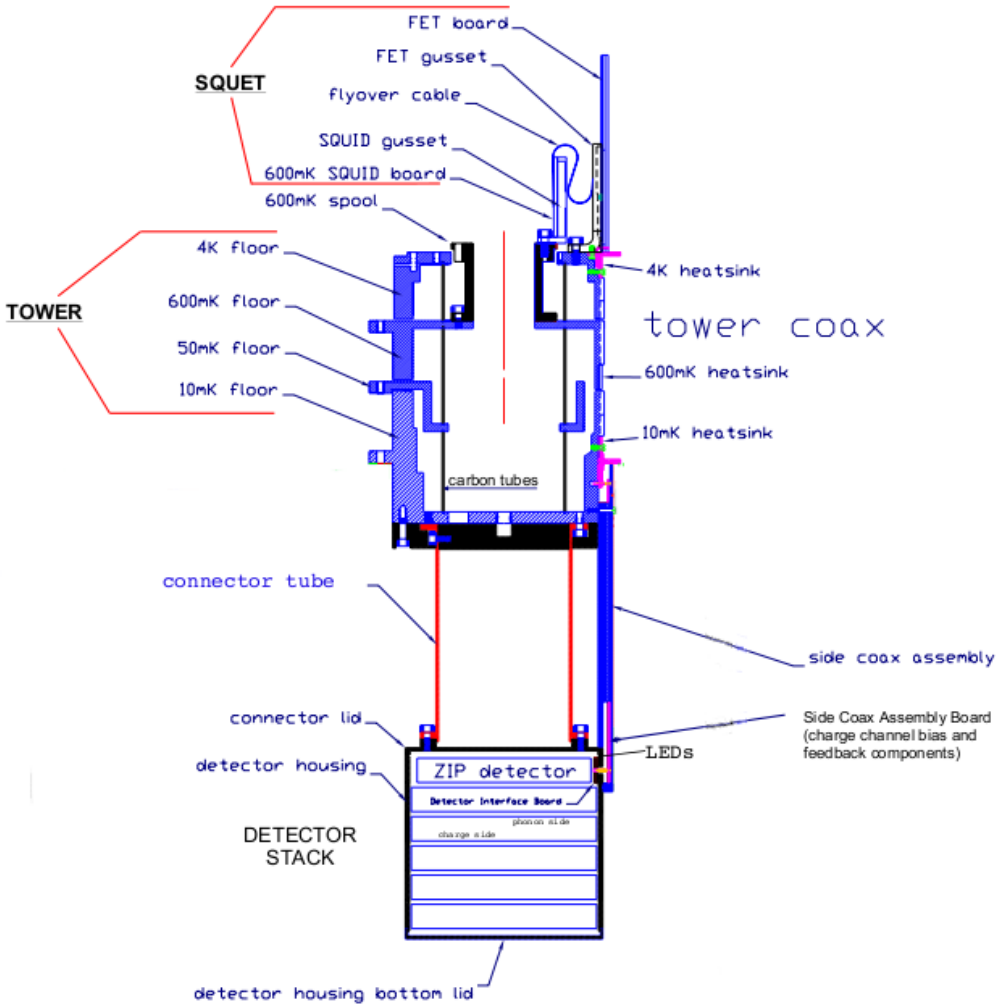

Figure 4.5: Cross section of the cold hardware assembly for one tower inside the Soudan icebox. The detector stack lies at the bottom, and a connector tube makes the connection from the detector housing to the rest of the tower assembly above, in four temperature stages each coupled to one of the icebox cans. The side coax assembly connects each detector interface board at the edges of the detector housing to the SQUET cards at the 4 K stage, where the ionization and phonon signals are amplified.

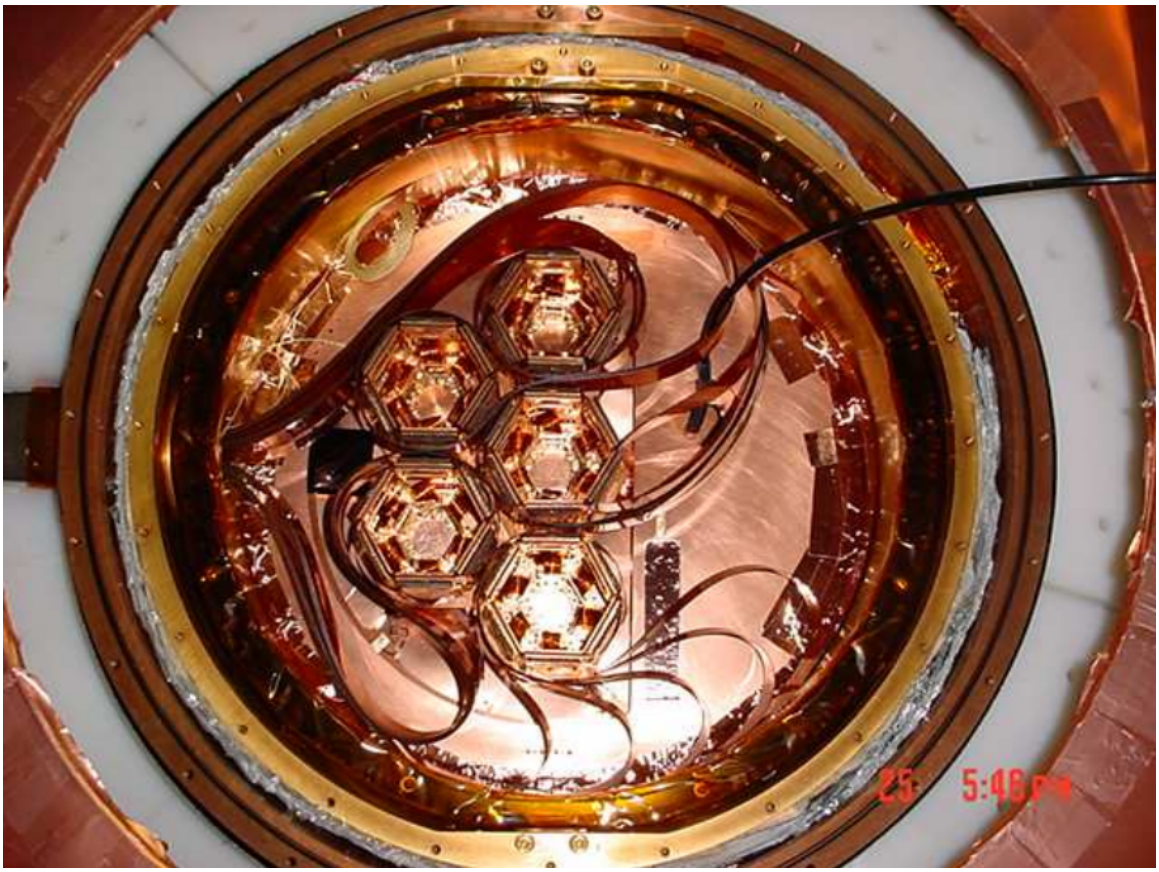

Figure 4.6: Top-down view of the Soudan icebox in its complete 5-tower configuration. Electronics exit the icebox to the left and the dilution refrigerator is connected to the right of the image.

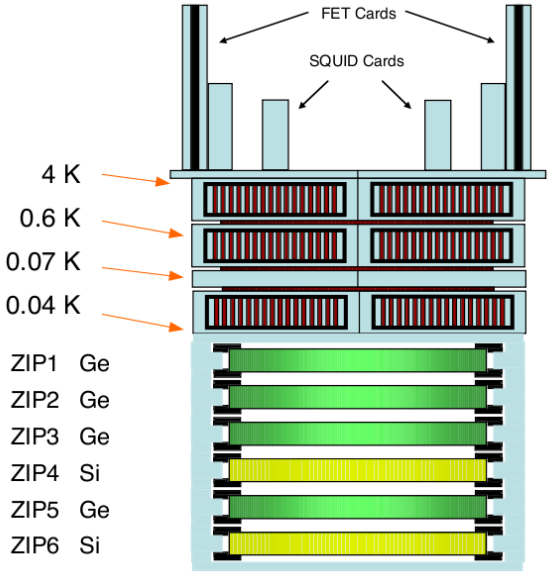

Figure 4.7: Detail of the layout of the tower labeled "T1" throughout Soudan operations, containing four Ge detectors and two Si detectors. A central graphite connector tube supports the separation of the four temperature stages.

4.3.2 Tower arrays

Each "tower" is a hexagonal copper support structure that houses the detector stack and facilitates the electrical connection to the SQUET cards (see Sec. 4.3.3). The temperature steps down through each of the tower's four separate copper stages, each heat-sunk to a different icebox can. These four stages are supported by a central graphite cylinder, which separates the stages with a connection of low thermal conductivity. The six faces of the tower correspond to the six detectors inside, with each face carrying the bias and signal wires from the side coax at base temperature up to the SQUET card at 4 K. Between base temperature and the 4 K stage, the wires are additionally thermally coupled to the still temperature stage (∼500 mK), and are routed under tension through vacuum channels. A cross-section of the first tower is shown in Fig. 4.7. The Si ZIPs are located in the stack positions labeled 4 and 6, so the convention is to refer to these detectors as T1Z4 and T1Z6, respectively.

4.3.3 Other assembly hardware

Side coaxes

The connection between a detector and the base temperature stage of its tower face is made by a connector called a side coax, which also houses the coupling capacitors and bias and feedback resistors of the two ionization channel amplifiers for that detector. Keeping these components at base temperature reduces their Johnson–Nyquist noise contributions to the ionization signal.

SQUET cards

Mounted at the top of each tower is an assembly including both SQUID and FET components, known as the "SQUET" card assembly (Fig. 4.8). The primary circuit board in this assembly houses the FETs for the charge amplifiers, and a second contains the SQUIDs and associated components for the phonon amplifiers. Located at the 4 K stage, where their carriers would be frozen out, the FETs must be self-heated to ∼140 K. To protect the rest of the 4 K stage from the much warmer FETs, they are supported on a Kapton membrane within a copper gusset. The SQUID card is heat-sunk to the still stage of the tower for improved SQUID performance and reduced Johnson–Nyquist noise in the shunt resistors compared to what could be attained at the 4 K stage.

Striplines

The final step in the cold hardware chain is a set of flexible, flat 3 m long electrical cables called striplines, each containing 50 copper conductors surrounded by Kapton insulation, sandwiched between two copper ground plates. One end is connected to a SQUET card, while the other end passes through the E-stem to a connector on the E-box bulkhead. The striplines are bundled and heat-sunk at two distinct points along the E-stem to limit heat flow into the 4 K stage.

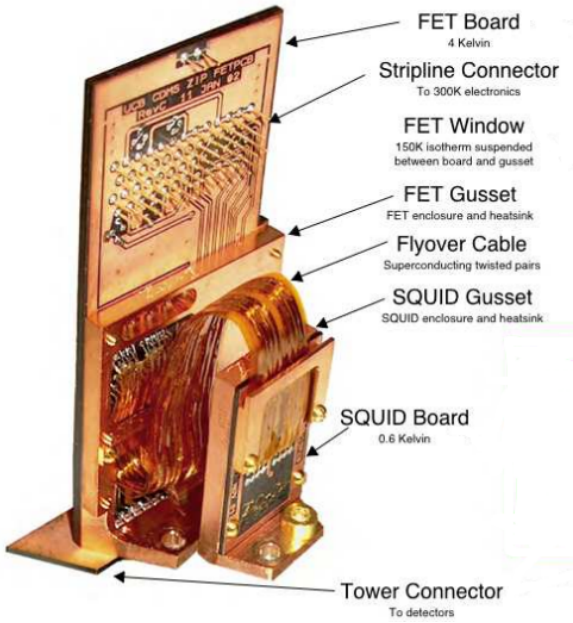

Figure 4.8: Detail of the CDMS SQUET (SQUID+FET) card assembly that facilitates electronics readout from each tower.

4.4 Warm electronics

4.4.1 Front-end boards

After exiting the E-box, signals pass along 50-pin D-sub cables toward several electronics racks in which the front-end boards (FEBs) are installed, each of which handles the signals from a single detector. These boards serve several distinct purposes. They buffer and amplify signals prior to digitization, and control the LEDs installed next to each detector used in restoring neutralization. They also contain the circuits used to apply the voltage bias to the ionization electrodes and for biasing the SQUIDs. These boards are controlled by a GPIB interface from the external electronics room, through fiber optic connections exiting the RF room.

4.4.2 Receiver-trigger-filter boards

After amplification by the FEBs, detector signals exit the RF room and are sent to receiver-trigger-filter (RTF) boards in the electronics room. Here the signals are prepared for digitization by having their baselines adjusted and being run through a 336 kHz 2-pole Butterworth anti-aliasing filter.

Digitization of a trace should occur only if an event of interest has taken place in one or more detectors. The RTF boards generate five distinct logical trigger signals that can be configured using logical operators to trigger digitization of signal traces. These consist of a low and high-level ionization signal triggers and three phonon signal triggers. All of these trigger values are recorded in a bit mask and saved for use in analysis.

The four analog phonon signals are summed. A comparator tests whether this summed phonon signal exceeds its baseline by an amount defined in a configuration file, typically a few mV. These thresholds are written to the RTF boards at the beginning of each series of data acquisition. The primary phonon trigger is set to minimize the energy threshold while avoiding triggering on a majority of noise events. The five trigger bits can be used together in other ways, such as to reject very high energy events or tag multiple scatters.

4.4.3 Data acquisition hardware

Trigger logic signals from the RTF boards next pass to a trigger logic board (TLB) where they are joined by similar triggers from the veto panel. The TLB determines when to issue a "global" trigger, which will initiate data acquisition for the most recent event. This will occur if either a ZIP has issued a phonon trigger, the veto shield has registered simultaneous hits in multiple veto panels, or a "random" trigger has been issued by the data acquisition system to measure the noise environment.

When a global trigger is issued, an array of 14-bit Struck SIS 3301 analog-digital converters digitize the signal from each of the six readout channels on each ZIP, and this "raw" data is saved to disk. The native sampling rate of this digitizer is 80 MHz, but to reduce digitizer noise, 64-sample sequences are averaged internally. There are 2048 samples recorded

per trigger, so at the averaged output rate of 1.25 MHz, each trace is 1.64 ms long. These traces are generally divided so that the post-trigger period is three times longer than the pre-trigger period. Thus each trace includes a 410 µs period preceding the trigger and a 1.23 ms period following the trigger.

The triggering mechanism for the muon veto is analogous. Raw pulses from the scintillator panels last only a few tens of nanoseconds, so they are sent through a pulse-stretching filter network before digitization. These reshaped pulses are then digitized by 12-bit Joerger VTR812 analog-digital converters, in a ∼200 µs trace (1024 samples at 5 MHz). Logic-level triggers are issued for each panel by comparators checking the signals against predetermined threshold values. These logic signals are passed along to the TLB where they are used to determine whether to issue a global trigger.

The triggers themselves are recorded by a set of Struck SIS 2400 time-to-digital converters. Timestamps with a resolution of 1 µs are recorded for each trigger in a circular buffer. As each event is saved to disk, this trigger history buffer is recorded as well, which allows inspection of the full trigger mask and timing information for up to four triggers prior to the primary global trigger and up to five triggers that follow.

At this point the hardware chain ends and further management of the data is taken up by software. The interface and processing, along with the management and diagnostic evaluation systems, are presented in detail in App. A.

Chapter 5

CDMS ZIP Detectors

The detectors used by the CDMS collaboration have gone through several iterations, but they all operate on the same basic principle of two-channel discrimination against electron recoil backgrounds. The strategy is encapsulated in their name: Z-sensitive Ionization and Phonon (ZIP) detectors.

The energy deposited in elastic scatters is partitioned into ionization and phonons differently for different recoil types, and ZIP detectors measure these two signals simultaneously for each recoil event.

5.1 Crystal characteristics

A ZIP detector is built on a cylindrical crystal substrate made of either germanium or silicon. The Soudan icebox was designed to house detectors with a 3 in diameter. The ZIPs used in CDMS II (sometimes called "oZIPs") had a thickness of 1 cm; for later versions used in SuperCDMS, such as the iZIP, the thickness was increased to 1 in. Future designs call for even larger dimensions, such as a 100 mm diameter for detectors planned for deployment at SuperCDMS SNOLAB. This chapter is concerned with the original ZIP design, as the primary nuclear recoil energy scale analysis presented here was performed on data acquired from these detectors during the dilution refrigerator runs numbered 125 through 128, from

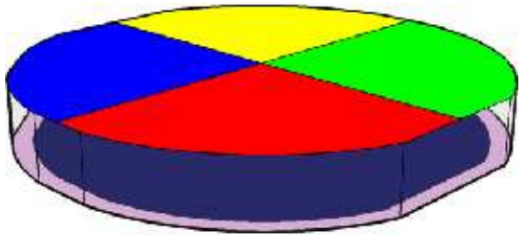

Figure 5.1: Simplified depiction of the sensor layout of a CDMS II ZIP detector. The top face is divided into four phonon sensor quadrants, and the bottom face is instrumented with two concentric ionization electrodes.

June 2007 to September 2008, in the final 5-tower configuration.

The detector shape is not perfectly cylindrical: there are two major flats at the north and south ends of the detector, two minor flats at the east and west ends, and an even smaller fifth flat at the northwest, which indicates the orientation of the crystal axis in the face-centered cubic structure: the vertical axis is aligned with the (001) crystal axis, and the fifth flat, centered at 45° west of north, is along the (100) crystal axis.

The use of two different target materials was motivated by their different responses to potential dark matter signals. Silicon has a density of $2.33\,\mathrm{g/cm^3}$, while that of germanium is more than double: $5.34\,\mathrm{g/cm^3}$. As a result, each Si ZIP has a mass of $\sim$100 g, while each Ge ZIP is $\sim$230 g. Assuming similar livetimes, a Ge detector will always have more WIMP exposure than a Si detector of the same volume. However, as discussed in Sec. 6.2.2, Si has a higher neutron scattering cross section than Ge for nuclear recoils in the analysis energy range. If many WIMP candidates were seen in both Si and Ge, a comparison of the relative rates in each detector type could thus indicate whether the candidate events were likely neutron-induced.

The faces of each detector are photolithographically patterned with sensor wiring, as seen in Fig. 5.1. The detectors were installed in the icebox with the ionization side facing downward and the phonon side facing upward. The bottom face is covered by two concentric electrodes: "Q_{inner}," the inner electrode covering $\sim$80% of the bottom surface, and "Q_{outer}," an outer guard ring 3 mm in width. The top face is covered by phonon sensors divided into

four quadrants, each composed of 1036 parallel tungsten transition edge sensors (TES) fed by an array of aluminum fins acting as quasiparticle traps (detailed in Sec. 5.4.1).

5.2 Ionization signal

A portion of the total energy deposited into a semiconductor crystal by a particle interaction is dissipated into the electron system of the crystal, separating charge carriers into electron-hole pairs. The first electrons produced in this way have relatively high momentum, which allows them to excite other electrons from their ground states up to the conduction band. This process repeats many times, resulting in a cascade of charge carriers in the conduction band, and finally a population of relatively low-momentum electron-hole pairs close to the particle track.

Only a fraction of the total energy deposited into the crystal lattice by the incident particle goes into the production of charge carriers, as this process is in competition with the generation of phonons. The partitioning of energy between these two systems is characterized by the parameter ϵ, defined as the average recoil energy required for an electron recoil to produce one electron-hole pair. At 0 K Ge and Si have band gaps of 0.734 eV and 1.12 eV, respectively, while they have ϵ values of approximately 3.0 eV and 3.82 eV. This factor is of critical importance in understanding the ionization yield, and its temperature and particle type dependence are discussed in Sec. 7.3.

In the absence of any applied field, these newly created charge carriers diffuse through the crystal and either recombine or fall into "trap" states within the band gap. However, under an applied voltage across the crystal, these carriers drift toward the ionization electrodes, which detect induced image charges as the carriers approach. With perfect charge collection (an assumption discussed in Sec. 7.2.2), the total image charge collected on both electrodes should equal the true charge generated by the interaction, with no dependence on interaction depth. The charge resulting from a hole drifting downward and an electron drifting upward will sum to the same amount as for an electron traversing the full path length from electrode to electrode.

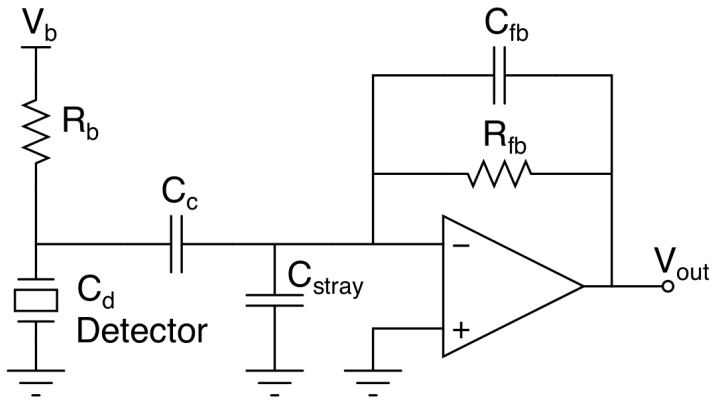

Figure 5.2: Schematic of the ionization readout amplifier circuit. The detector's inner electrode has a capacitance $C_d = 93\,\mathrm{pF}$, and is coupled to the amplifier by a capacitance $C_c = 300\,\mathrm{pF}$. The detector is voltage biased through a resistor $R_b = 40\,\mathrm{k\Omega}$.

5.2.1 Ionization readout

The electrodes are held at a constant DC voltage through a large bias resistance. The high frequency ionization signals are passed through a coupling capacitor to a FET amplifier before being read out as an analog voltage. A schematic of this readout circuit is shown in Fig. 5.2.

Charge collection takes less than 1 µs, so the pulse is seen as a sharp spike with an exponentially falling tail. The shape is set by the time constant τ of the feedback resistor and capacitor, $R_f = 4\,\mathrm{M\Omega}$ and $C_f = 1\,\mathrm{pF}$, so $\tau = 40\,\mu\mathrm{s}$. All charge pulses have this shape, and are distinguished by their overall amplitude and noise variations.

5.3 Athermal phonon signal

The number of phonons generated when a particle scatters in a ZIP is in general proportional to the recoil energy deposited, but this proportionality is not straightforward. A key feature of ZIP detectors is that they are designed to measure phonons before the detector has had time to come to thermal equilibrium. An advantage of the promptness of this measurement is that the phonons encode positional information about the event in the relative start times

of the phonon signals in each quadrant of the phonon sensor.

These out-of-equilibrium phonons are referred to as "athermal" phonons, and they are produced in several populations by three distinct mechanisms. The relative contribution of each mechanism to the total phonon signal, when combined with the ionization response, allows for discrimination between electron recoils and nuclear recoils.

Primary phonons

The first phonons to be produced are those resulting from displacements of nuclei and electrons. The major fraction of the deposited kinetic recoil energy goes into the production of two types of primary phonons - high energy, low-momentum "optical" phonons (in which mode adjacent atoms move in opposition) and lower-energy "acoustic" phonons (in which adjacent atoms move together). These primary phonons play the dominant role in encoding information about position and timing of the interaction event.

Recombination phonons

The fraction of the deposited recoil energy not immediately devoted to phonon production goes into ionization, liberating electrons into the conduction band. Each such liberation requires an input of the band gap energy E_g. The energy stored in the drifting charge carriers is thus simply $N_Q E_g$. When the carriers reach the electrodes and relax to the Fermi level, this energy is returned to the crystal in the form of recombination phonons. Together with the primary phonons, these two mechanisms account for the total recoil energy of the particle interaction, entirely through phonons.

Neganov-Trofimov-Luke phonons

The total phonon signal has one additional component. The mechanism was separately proposed by Neganov and Trofimov (48) and by Luke (49). As the applied electric field does work moving the liberated charge carriers across the crystal, this energy is dissipated into the crystal in radiated Neganov-Trofimov-Luke phonons (often also called simply "Luke

phonons"). These phonons are analogous to Cherenkov radiation in that they are produced when charge carriers travel faster than the speed of sound in the drift medium. They contribute an energy to the total phonon signal equal to the work done by the field's work on the charges:

$$E_{\text{Luke}} = \sum_i q_i \int_{C_i} \vec{E} \cdot d\vec{x}, \tag{5.1}$$

where the sum runs over each charge i and the integral is over its path C_i. Since the electric field is approximately uniform in the fiducial volume of the detectors, and because each electron-hole pair travels a total distance d equal to the thickness of the crystal, a sum over individual charge carrier paths becomes

$$E_{\text{Luke}} = eV_b \sum_i \frac{d_i}{d} = eV_b N_Q. \tag{5.2}$$

To see how the Luke phonon energy is related to the ionization energy, we recall that $E_Q = N_Q \epsilon$, and so $E_{\text{Luke}} = E_Q \left(eV_b/\epsilon\right)$. Under the assumption that all three phonon types are collected with the same efficiency, the total phonon energy becomes:

$$E_P = E_{\text{prim.}} + E_{\text{recomb.}} + E_{\text{Luke}} \tag{5.3}$$

$$= (E_R - N_Q E_g) + N_Q E_g + \frac{E_Q e V_b}{\epsilon} \tag{5.4}$$

$$= E_R + \frac{E_Q e V_b}{\epsilon} \tag{5.5}$$

This equation immediately suggests that an event's recoil energy E_R can be measured by a simple linear combination of the total phonon energy E_P and the ionization energy E_Q. After these energies are calibrated, they are combined in this way to form the primary analysis variable, a dual-signal measure of the recoil energy that is valid for both electron recoils and nuclear recoils.

5.4 Phonon propagation and collection

As phonons propagate across the crystal they participate in scattering off impurities in the crystal, charge carriers, and each other, as well as anharmonic decay, where a phonon decays into two lower-energy phonons each carrying roughly half the energy. At mK temperatures the dominant scattering mode is scattering off impurities. This process and anharmonic decay are both highly frequency-dependent, so lower-frequency phonons have much longer mean free paths. Most primary phonons initially have frequencies of several THz. At these very high frequencies, rapid anharmonic decay proceeds until isotope scattering begins to dominate around 1.6 THz. At this point the phonons "quasi-diffuse" through the crystal by frequent isotope scattering and occasional further anharmonic decays. These decays proceed for several µs, after which their mean free paths are comparable to the size of the detector. At this point they are said to be "ballistic" and they are able to reach the detector surfaces relatively unimpeded. They are then collected at the top surface of the ZIP.

For the reasons stated above, the primary phonons detected by the ZIPs are generally at ballistic frequencies. Luke phonons are generated in this range as well (50). Recombination phonons are generated at much higher energies, but upon interacting with the metal fins at the detector surface they rapidly down-convert to ballistic frequencies as well. This same rapid down-conversion process occurs for any high-frequency primary phonons that reach the fins. Phonons from recoils very near the detector surface therefore tend to reach ballistic frequencies more quickly and are thus more likely to absorbed over a shorter time scale. This is believed to be a source of the observed faster pulse timing characteristics of surface events (see Sec. 6.3.1).

5.4.1 Phonon sensors

Each ZIP has four phonon sensor quadrants instrumented on the top face, as depicted in Fig. 5.3. Each of these quadrants is patterned with 1036 tungsten transition-edge sensors (TES) wired in parallel, each just 1 µm in width, but connected to a 350 µm-long aluminum collector fin that serves to feed the TES with phonon energy gathered over a much larger

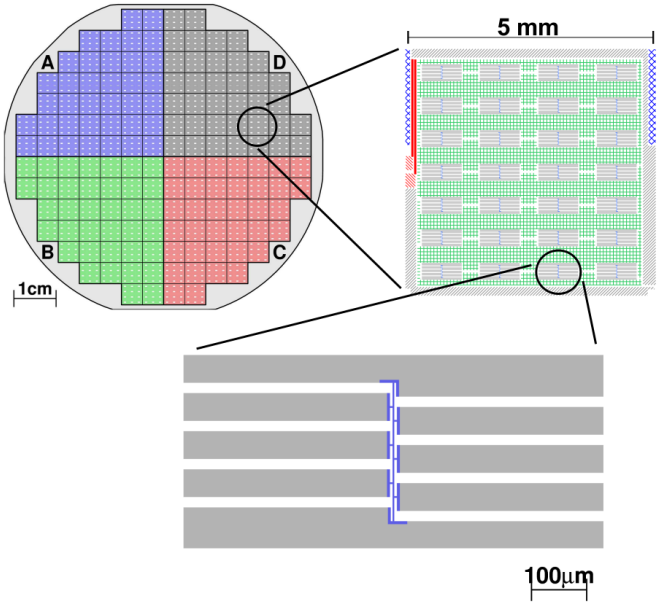

Figure 5.3: The layout of the four phonon sensors on a ZIP detector. Each sensor consists of 37 square 5 mm dies. Top right, a single die, consisting of 28 individual QETs. Bottom, one QET shown in detail, where a 1 µm-wide W TES is connected to Al collector fins (51).

area.

The Al fins function by absorbing phonons, and those with energy greater than 0.36 meV (twice the superconducting gap energy in Al, roughly two orders of magnitude greater than the typical energy of thermal phonons at 40 mK) can break a Cooper pair and create quasiparticles. These quasiparticles diffuse through the fins toward the end of the TES, where there is an overlap between the Al fin and the W TES. The minimum quasiparticle energy in W is much lower than that in the fins (∼25 µeV). This means that a quasiparticle that enters the tungsten will not be able to diffuse back into the Al if it has lost enough energy to be below the minimum quasiparticle energy in Al. The quasiparticles lose energy by rapidly radiating low-energy phonons back into the crystal, as they relax to the local gap level. They are thus effectively trapped in the TES, as depicted in Fig. 5.4.

The TES is a thin film of tungsten held at its superconducting transition temperature, $T_c \approx 80$ mK. As it transitions between superconductivity and normal resistance, large

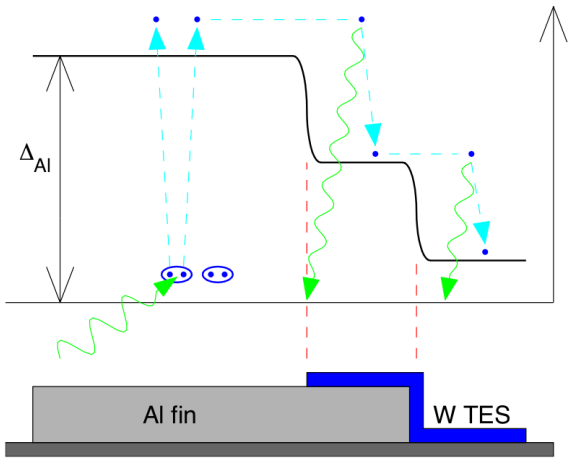

Figure 5.4: Incoming phonons with energy above the band gap $\Delta_{Al} = 0.36\,\text{meV}$ can break Cooper pairs in the Al fins. The resulting quasiparticles diffuse through the fins, first entering an overlap region between the Al fin and W TES, and then the TES itself. These regions have successively lower minimum quasiparticle energies. Since quasiparticles rapidly lose energy by radiating low-energy phonons, they relax to the local gap levels and cannot diffuse backward, trapping them in the TES (51).

changes in resistance can be detected for very small temperature changes due to input phonon energy.

5.4.2 TES readout via SQUIDs

Ultimately, the TES sees a small change in current, which must be converted to a voltage that can be digitized. The TES is voltage biased using a bias current I_b and a shunt resistor $R_s = 25\,\text{m}\Omega$ wired in parallel with the TES. A change in the current through the TES produces a change in magnetic flux through a DC SQUID. The change in SQUID voltage is then amplified and returned to a feedback coil. This configuration allows for a negative feedback loop: the amplifier adjusts its output voltage so that it drives enough current to cancel the change in SQUID flux. This current is converted into a voltage by the feedback resistor $R_f = 1200\,\text{k}\Omega$ and is read as the voltage output. This feedback loop keeps the TES biased near the middle of its superconducting transition, ready to respond to the next phonon pulse.

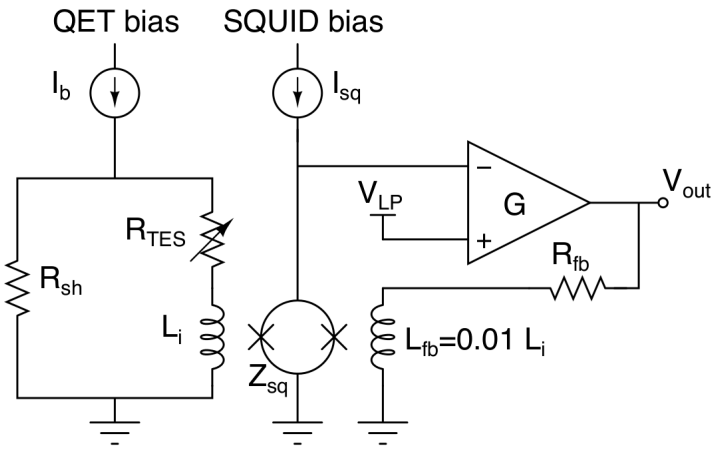

Figure 5.5: Schematic of the phonon channel bias and SQUID-based readout circuit. The TES is voltage biased using a bias current I_b and a shunt resistor $R_s = 25\,\mathrm{m}\Omega$ wired in parallel with the TES. The input coil L_i couples the current through the TES to the SQUID and amplifier.

5.5 Signal reconstruction

The primary pulse reconstruction algorithm used by CDMS is an optimal filter, by which the observed trace is fit in the frequency domain to a template pulse. The optimal filtering algorithm is described in detail in Appendix B of Sunil Golwala's dissertation (52). The technique works especially well for the ionization pulses, which have essentially the same shape at all energies. Optimal filtering minimizes the influence of variations in the noise power across frequencies and provides a consistently good fit down to very low energies in ZIPs, generally as low as a few keV.

5.5.1 Ionization pulse reconstruction

Ionization traces from CDMS II ZIPs have a very uniform shape: an extremely sharp rising edge with decay times determined by the electronics, and Gaussian noise. A typical electron recoil ionization trace is shown in Fig. 5.6, with an example template inset. These templates are constructed by averaging a subset of well-collected and well-formed pulses for each detector. The optimal filter fits the ionization traces from the inner and outer channels

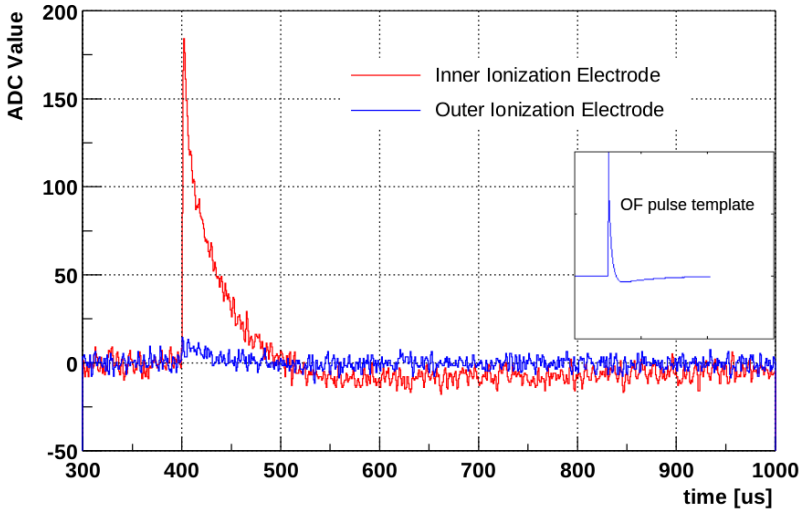

Figure 5.6: Pulses from inner and outer ionization channels for a typical electron recoil event. (inset) An example template used for optimal filtering of charge pulses.

to the corresponding templates in the frequency domain to reconstruct collected ionization.

5.5.2 Phonon pulse reconstruction

Signals from the phonon channels are also run through an optimal filtering algorithm, but unlike the charge signals, phonon pulse shape (shown in Fig. 5.7) carries useful information. Therefore energy and pulse reconstruction are handled separately.

To reconstruct the energy of an event's phonon signal, the start time and amplitude of each channel's phonon trace are fit separately to a double exponential template. Like the ionization reconstruction, there is a fixed template. Phonon pulse shapes vary widely with position and relative energy collected per channel, so there is a significant energy and position dependence to these fits, which must be corrected (see Sec. 7.2.1).

The pulse shape is parametrized by the time of first-crossing of several thresholds. The two most important phonon timing parameters are:

- Rise time: the difference between the first-crossing times for 10% and 40% of the maximum amplitude of the largest phonon pulse

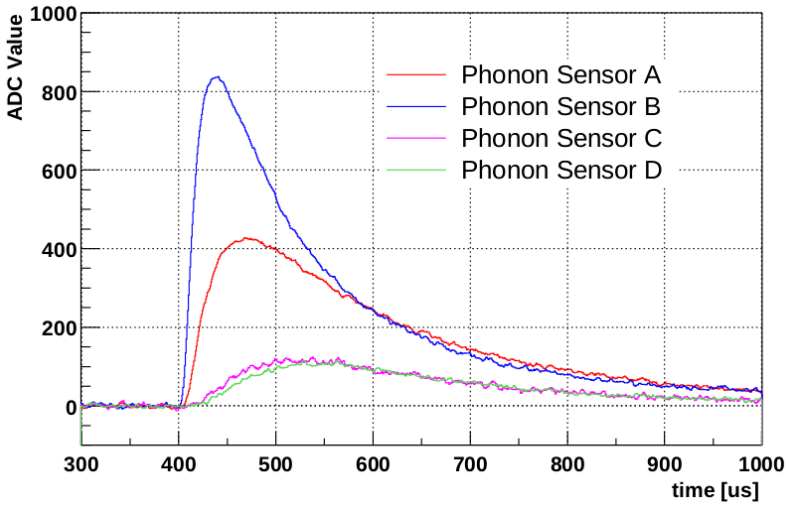

Figure 5.7: The phonon traces from a typical electron recoil event of $\sim 50\,\mathrm{keV}$. The channel nearest the initial scattering site has the largest pulse amplitude.

- Delay time: the difference between the start time of the ionization pulse and the first-crossing time for 20% of the maximum amplitude of the largest phonon pulse

To mitigate excess high frequency noise, the pulses are passed through a low-pass Butterworth filter (50 kHz) before the calculating the first-crossing times. These times are calculated using a simple time-domain walk algorithm.

The initial position reconstruction of an event is done by comparing phonon pulse amplitudes and pulse-shape parameters across the four quadrants. This results in two independent measures of each event's position.

1. Phonon delay: phonons are first absorbed into sensor quadrant nearest the initial site of the interaction. The largest phonon pulse is taken to be the closest to the event, and delay times are calculated relative to this quadrant. So for an event for which the pulse is largest in the 'B' quadrant, the phonon delay times are defined in terms

of the 20% risetimes (P*r20) as

$$\text{xdel} \equiv \text{PBr20} - \text{PCr20}$$
$$\text{ydel} \equiv \text{PAr20} - \text{PBr20}$$

The resulting position distribution for a ^{109}Cd calibration data set is shown in the left pane of Fig. 5.8.

2. Phonon partition: the greatest fraction of phonons is absorbed in the sensor quadrant nearest the initial site of the interaction. This can be seen in the reconstructed energy for each quadrant. Based on this principle we define an independent position estimates based on the partitioning of energy (p*) between the sensors, called the x-partition and y-partition:

$$\text{xppart} \equiv \frac{(\text{pc} + \text{pd} - \text{pa} + \text{pb})}{(\text{pa} + \text{pb} + \text{pc} + \text{pd})}$$
$$\text{yppart} \equiv \frac{(\text{pa} + \text{pd} - \text{pb} + \text{pc})}{(\text{pa} + \text{pb} + \text{pc} + \text{pd})}$$

This partition is a four-point reconstruction of the position, mapping the detector onto a square, as shown in the right panel of Fig. 5.8. As this is based solely on the amplitude measure of the optimal filter, it has superior resolution to the delay-based position quantities, which rely on the filtered walk algorithm.

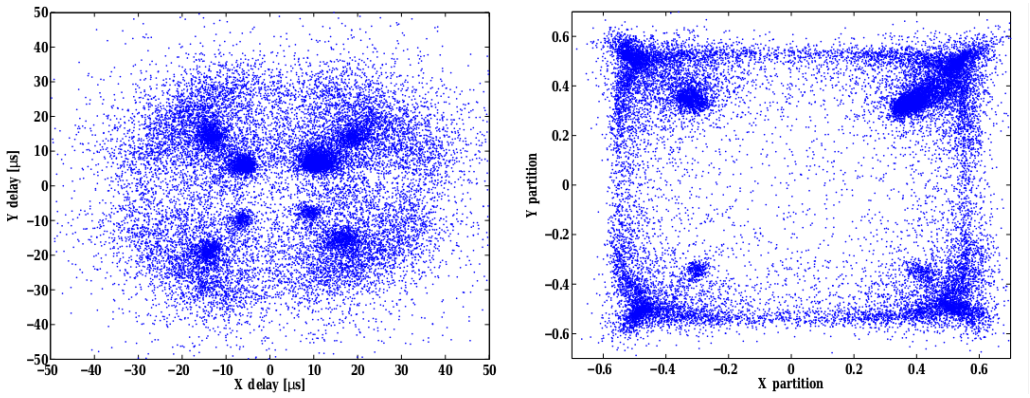

Figure 5.8: Reconstructed event positions for ^{109}Cd calibration data, collimated through eight holes, seen as denser event clusters. (left) Phonon timing: y-delay vs x-delay. (right) Fractional phonon energy per quadrant: y-partition vs x-partition.

Chapter 6

Signal Analysis and Backgrounds

Interactions between dark matter particles and ZIP detectors are expected to result in a very small energy deposition, with a very low event rate. Suppression and discrimination against backgrounds to this very small signal is the chief task of shielding and data analysis. The active and passive shielding were detailed in Sec. 4.2. The majority of the remaining background comes from radioactive decays of contamination inside the shielding. Cosmic ray-induced neutron backgrounds can also begin to play a significant role as the overall exposure increases, ultimately motivating a move to a deeper site.

This chapter is concerned with the characterization of the signals seen by ZIP detectors. The backgrounds are grouped into three broad classes, each of which is minimized and quantified in its own way.

6.1 Bulk electron recoils

Electron recoils occurring in the bulk of the detector lead to far more triggered events than any other particle interaction type during low background running. These events typically result from photons produced by radioactive materials in the detector housing and surrounding material. Most of the materials used in the apparatus were screened before installation with a high purity Ge detector to quantify and minimize this contamination.

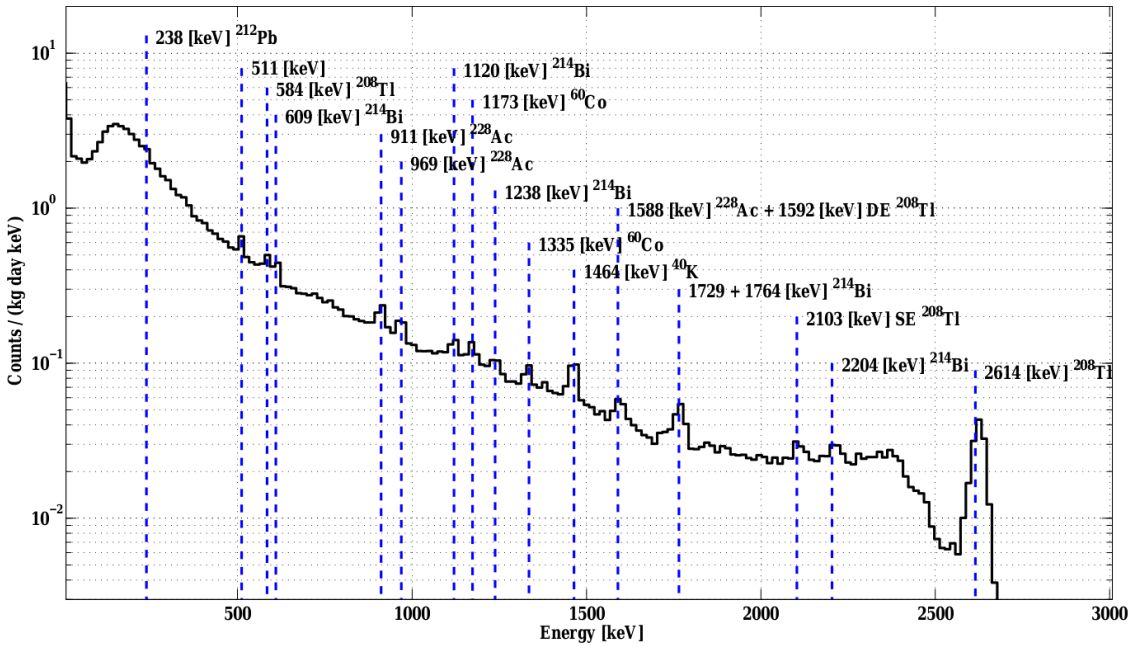

Figure 6.1: Energy spectrum of bulk electron recoils recorded in low-background data-taking mode for Run 123-128, coadded over Ge detectors. The labeled lines are part of the ^{238}U and ^{232}Th decay chains, or directly from the decay of ^{40}K and ^{60}Co (51).

The inner volume between the innermost polethylene layer and the mu-metal shield is continuously purged with N_2 gas to minimize radioactivity from the radon-rich mine air. Thus the bulk gamma background comes primarily from materials that are very close to the detectors: the vacuum cans inside the icebox and the copper towers themselves.

Peaks in the energy spectra of these bulk electron recoils can be identified with the radioactive isotopes that produce them. A detailed study of the spectral peaks found in background data from all 5-tower runs, coadded over all Ge detectors, is shown in Fig. 6.1. The major source of these background gammas is shown to be naturally present ^{238}U and ^{232}Th isotopes and their decay products, which account for most of the identified lines. A subdominant contribution is seen to come from ^{40}K and ^{60}Co. The high rate in the first bin is due to activation of ^{73}Ge by the ^{252}Cf neutron calibration source. This produces a prominent activation line at 10.36 keV.

CDMS discriminates against electron recoil backgrounds using the ionization yield parameter, combining data from both the ionization and phonon sensor systems. A charged particle moving through a crystal lattice loses energy primarily through two mechanisms: ionizing atoms by interacting with and liberating valence electrons, and by transferring kinetic energy directly to nuclei, resulting in the emission of phonons. The partitioning of energy loss between these two mechanisms is determined by the incident particle's mass, charge, and kinetic energy. A detailed discussion of these processes can be found in Sec. 7.3.

Nuclear recoils have suppressed yield relative to electron recoils. In the energy range of interest, generally above 10 keV, there is very clear separation of bulk electron recoils and nuclear recoils in the plane of yield vs recoil energy, shown in Fig. 6.2. The electron recoil band was sampled extensively several times per week through the collection of calibration data while exposed to a ^{133}Ba source. The nuclear recoil band was measured more infrequently by calibration with a ^{252}Cf neutron source. The analysis and construction of these bands is discussed in Sec. 7.3.1 and 7.3.2. For recoil energies greater than $\sim$10 keV, yield discrimination rejects bulk electron recoils from leaking into the nuclear recoil signal band at a level better than 1 event per 10^4.

6.2 Nuclear recoils

Nuclear recoils from neutrons are the most dangerous background for a WIMP-search analysis, as nuclear recoils from WIMPs cannot in general be distinguished from those coming from non-WIMP sources. A neutron with energy in the MeV range could produce a nuclear recoil in the keV range and subsequently be identified as a WIMP candidate. The CDMS II experimental configuration is located underground and has extensive shielding to reduce the rate of these events, with the goal of limiting them to less than one expected event over the entire exposure. The two major neutron sources are cosmic ray showers and natural radioactivity in the materials around the detectors.

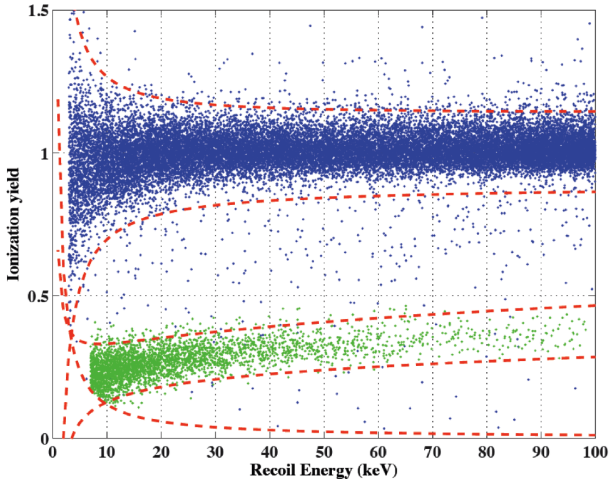

Figure 6.2: Ionization yield vs recoil energy for a typical ZIP detector. The electron recoil band at unity yield is populated by events from a data set taken with a ^{133}Ba calibration source, while the band at yield ~ 0.3 is populated mostly by nuclear recoils from a data set taken with a ^{252}Cf calibration source.

6.2.1 Cosmogenic neutron background

Muons produced by high energy cosmic rays in the atmosphere can penetrate the rock overburden if they have sufficient energy. These muons can produce neutrons, either by forced nuclear disintegration (spallation) or through secondary processes in their electromagnetic and hadronic showers. No practical detector shielding can sufficiently reduce the flux of these very high energy muons, but the composition of the Earth itself makes it effective large-scale shielding. The location of CDMS II at the Soudan Underground Laboratory, at a depth of 2090 meters water equivalent, below 714 m of underground greenstone, reduces the incident muon flux as measured on the surface by a factor of approximately 5×10^4. The CDMS veto shield (see Sec. 4.2.1) detects approximately 1 muon per minute, and so the residual cosmogenic neutron background, while greatly reduced, is not obviously negligible.

The active portion of the experimental shielding is the scintillating muon veto described in Sec. 4.2.1. An event is considered veto-coincident and excluded from WIMP-search data if there is a history buffer hit in any veto panel in the 50 µs prior to the global trigger, or if any panel exceeds its muon-tagging threshold. The efficiency of this veto cut is calculated as

$1-P$, where P is the probability for the veto cut conditions to be satisfied during a WIMP event, assuming no correlations between the veto and the WIMP. A somewhat conservative estimate of this efficiency can be found by calculating the fraction of random-trigger events excluded by the veto cut. For Runs 125-128, this efficiency was $97.876 \pm 0.013\%$.

The muon-tagging efficiency is calculated by examining identified muon events entering the shielded volume through a top panel and checking for discriminator hits in the bottom and side panels as the muon exits. Similarly, muon events exiting the shielded volume through a bottom panel are used to check for corresponding discriminator hits in the top and side panels. The inefficiencies for tagging entering and exiting muons are multiplied, and the resulting overall muon-tagging efficiency is found to be $99.9225^{+0.0060}_{-0.0062}\%$.

The overall cosmogenic neutron background estimates were calculated using a series of Monte Carlo simulations in Geant4 and FLUKA to compare fractions of vetoed and unvetoed single- and multiple-scatter events to those event classes measurable in the real data. The vast majority of cosmogenic nuclear recoil events scatter in multiple detectors, and would be excluded as WIMP candidates. For single scatters, the ratio of unvetoed events to vetoed events is multiplied by the number of vetoed nuclear recoil single scatters observed in the data to estimate the expected number of unvetoed nuclear recoil single scatters in the data.

The most current simulations for the 5-tower configuration used in dilution refrigerator Runs 125 through 128, the primary data under analysis, give a raw unvetoed single-scatter nuclear recoil rate of $(8.30 \pm 3.14) \times 10^{-5}\,\mathrm{kg}^{-1}\mathrm{day}^{-1}$ in the Ge detectors and $(2.59 \pm 1.16) \times 10^{-5}\,\mathrm{kg}^{-1}\mathrm{day}^{-1}$ in the Si detectors. In all cases these rates are integrated from the run- and detector-dependent threshold of each detector (10 keV for Ge, and 7-15 keV for Si) up to 100 keV. Weighted by the WIMP-search exposures for these runs, the total estimates for the unvetoed cosmogenic nuclear recoil background events are $0.214 \pm 0.0081(\mathrm{stat.}) \pm 0.0086(\mathrm{syst.})$ in the Ge detectors and $0.129 \pm 0.0058(\mathrm{stat.}) \pm 0.0033(\mathrm{syst.})$ in the Si detectors.

Component	Ge rate (n/kg-yr)	Si rate (n/kg-yr)
Copper cold hardware	3.6×10^{-3}	1.1×10^{-2}
Copper icebox cans	2.31×10^{-2}	6.0×10^{-2}
Inner polyethylene	$< 6 \times 10^{-3}$	$< 1.6 \times 10^{-2}$
Total copper/polyethylene	$2.67 - 3.27 \times 10^{-2}$	$7.1 - 8.7 \times 10^{-2}$
Inner lead	$< 3 \times 10^{-3}$	$< 2.4 \times 10^{-2}$
Outer lead	$< 7 \times 10^{-3}$	$< 5.3 \times 10^{-2}$
Total lead	$< 1 \times 10^{-2}$	$< 7.7 \times 10^{-2}$

Table 6.1: Expected radiogenic neutron event rates per kg-year integrated over the energy range 10-100 keV. Sufficiently many events were simulated that statistical errors are negligible.

6.2.2 Radiogenic neutron background

Radioactivity in the rock surrounding the experiment is an additional source of neutron background. Neutrons with energies in the MeV range are created through (α,n) reactions and spontaneous fission. The α particles mostly come as part of the uranium and thorium decay chains associated with contamination in the materials. Spontaneous fission is almost entirely from the uranium. If these neutrons come from a source outside the outer polyethylene shielding, they are moderated to sufficiently low energies that they do not trigger the detectors. Radiogenic neutrons originating in interior layers have a flux at the detectors dependent on both the distribution of the contamination and the geometry of the nearby hardware and shielding. Through a combination of screening and Geant4 Monte Carlo simulations, upper limits have been placed on the event rates for radiogenic neutrons in Ge and Si detectors, quantified in Table 6.1.

For neutrons to deposit recoil energies in the analysis range, they must have kinetic energies of a few hundreds of keV. Neutrons in this energy range have a ~ 10 times larger scattering cross section on Si than on Ge (see Fig. 8.25). Thus the radiogenic neutron event rates in Si are significantly larger than those in Ge. This is is somewhat counteracted by the much smaller total mass of Si present than Ge. The expected total detection rates are of the same order of magnitude. Over the exposures of the 5-tower runs, the expected

radiogenic background count in each material is much less than 1, and essentially negligible compared to the dominant background from surface electron recoils.

6.3 Surface electron recoil events

Unlike those events occurring in the bulk of the detectors, electron recoils occurring within $\sim$10 µm of the detector surface (referred to as the "dead layer") have pathological charge signals. Because the charge carriers are liberated so close to the electrodes, some charge carriers of the wrong polarity are collected rather than being drifted to the opposite face. This results in a suppressed ionization signal, and therefore suppressed ionization yield. This causes these events to mimic nuclear recoils, and as such they form a significant background for any search for nuclear recoils from WIMPs.

In contrast to bulk events, which are predominantly due to Compton scatters of photons from local radioactivity with long mean free paths, surface events are caused either by Compton scatters that happen to occur near the surface or by low energy electrons incident on the detector surface. The contribution from Comptons is estimated using ^{133}Ba calibration data, for which the ratio of single-scatter surface events to bulk events is $(8\pm4)\times10^{-4}$. The ambient bulk electron recoil rate has been measured to be 295 counts/kg/day, and so the expected rate of surface events from Comptons is (0.217 ± 0.1) counts/kg/day.

Another source of this background is believed to be electrons coming from beta decays of ^{210}Pb surface contamination. This contamination may occur during fabrication, or it may result from decays of the ^{222}Rn isotope in the mine air, which decays to ^{210}Pb with a half-life of 3.8 days. The half-life of ^{210}Pb itself is 22.3 years, so this contamination is effectively permanent. By observing other decay products in this chain and comparing to Monte Carlo simulations, the expected rate of surface events from ^{210}Pb β-decay electrons is estimated to be (0.240 ± 0.183) counts/kg/day.

Together these sources represent a very large background of events that are indistinguishable from WIMPs based solely on their reconstructed energies in the ionization and

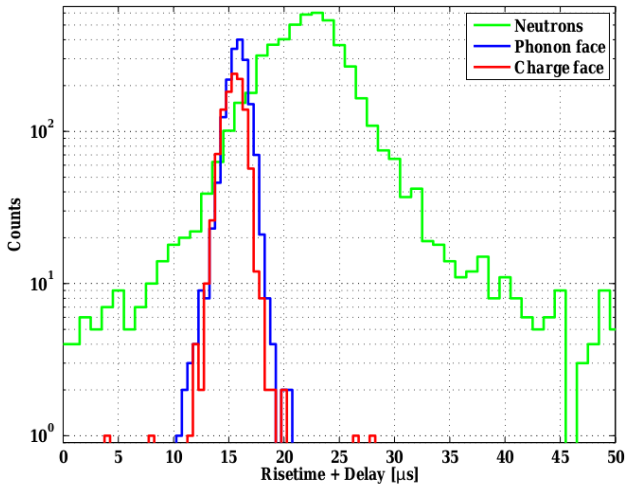

Figure 6.3: Timing distribution of surface events in each face vs bulk nuclear recoil events. The timing cut must be set at a sufficiently high combined timing parameter so that the expected leakage is below some chosen value (generally 0.5) while minimizing loss of the broader signal distribution biased toward slower timing.

phonon channels. However, surface events have different timing properties than bulk electron recoils. Discrimination against this background is therefore possible through detailed timing analysis. CDMS II is able to reject more than 99% of surface events while maintaining good nuclear recoil acceptance.

6.3.1 Timing cuts

Surface events generally have faster timing characteristics than bulk electron recoils. This means their phonon pulses tend to have a sharper rising edge and shorter delay times relative to the charge signal (shown in Fig. 6.3). These timing differences can be combined into a multi-parameter cut optimized to maximize acceptance of signal while keeping the expected surface event background to a minimal leakage level initially chosen to be 0.5 expected events in the signal region after all analysis cuts. This cut is defined using surface event and bulk nuclear recoil samples from ^{133}Ba and ^{252}Cf calibration data.

In setting this cut, care must be taken to account for systematic differences between the surface event populations in the calibration data and the WIMP-search data.

- Yield distribution: Events occurring at the charge-side surface tend to have higher yield than those on the phonon-side surface. Because of the location of the sources during calibration running, the charge faces receive significantly less illumination with the low-energy gammas that cause these surface events than do the phonon faces. This biases the yield distribution of surface events in calibration data to lower yield than is seen in low background WIMP-search data. Charge-side surface events also tend to have more outliers on the slow side of the timing distribution, which requires a harsher cut, costing signal efficiency.

- Energy distribution: WIMP-search signal region events have a much higher fraction of low energy events than surface events from the ^{133}Ba calibration sample, on either detector face. Due to the poorer signal-to-noise ratio at low energy, these events have smeared timing characteristics and are reconstructed to have slower timing than surface events at higher energy, making them harder to distinguish from bulk nuclear recoils.

These systematics result in a lower surface-event leakage estimate from the calibration sample than from WIMP-search sidebands. These differences are accounted for using scaling factors between the distributions when optimizing the final timing cut to get the most accurate leakage estimate possible.

Chapter 7

Energy Calibration

WIMP signal events will be extremely rare and are most likely to appear at low recoil energies. Taking advantage of the good energy resolution of solid-state detectors like CDMS, CoGeNT, EDELWEISS, etc., requires a deep understanding of the relevant energy scales. This chapter describes the methods used to calibrate energy scales for both the ionization and phonon channels in CDMS ZIPs.

The concept of ionization yield, introduced in Sec. 6.1, dictates the classes of events to which these calibrated energy scales will be applicable. Nuclear recoils (NRs) have suppressed ionization signals relative to electron recoils (ERs) of the same recoil energy, and so we calibrate the response of the ZIPs to each recoil type differently. A brief outline of the procedure, which will be described in more detail throughout in this chapter, is as follows:

1. The overall normalization and linearity of the energy scale for ERs in the ZIPs is clearly established by peaks of known gamma energy in the ionization spectrum of calibration data from a ^{133}Ba source.

2. This electron-equivalent ($\mathrm{keV_{ee}}$) energy scale enables calibration of the total phonon signal ($\mathrm{keV_t}$) by enforcing unity yield for ERs in aggregate.

3. Subtracting an event's Luke phonon contribution, as measured by the ionization signal, from its calibrated total ($\mathrm{keV_t}$) phonon energy results in a valid measure, to within resolution effects, of the true recoil energy ($\mathrm{keV_r}$) for both ERs and NRs.

The ultimate calibration goal for a WIMP-nucleus scattering experiment is to characterize the response of the detector to the deposition of energy in nuclear recoils, for each detection channel. An accurate measure of their true recoil energy near the low energy threshold, where the expected WIMP signal rate is highest, is crucial. This is complicated by several systematic effects that will be presented toward the end of the chapter.

7.1 Ionization calibration

The ionization signal is calibrated using data taken with a ^{133}Ba source, which has spectral lines at 302.8 keV, 356.0 keV and 383.8 keV. At these energies, photons are not stopped by the copper of the icebox cans and they provide reliable calibration features. Several steps are necessary to calibrate the ionization pulses to a physical energy quantity. The raw pulses are processed by an optimal filter (OF) algorithm (as described in 5.5), which returns an amplitude sensitive to a few minor detector-related pathologies.

Crosstalk

The first of these pathologies is residual crosstalk between the two ionization channels, in which a small portion of the charge signal collected by the inner electrode is registered in the outer electrode, and vice versa. This effect is corrected for with a small ($< 1\%$) linear correction factor (shown for representative Tower 3 detectors in in Figs. 7.1 and 7.2). This factor is found by applying a linear fit (shown as a red line) to a set of Gaussian fits of events clustered along the axis, binned in energy. This results in a more accurate measure of the true charge collection and improves the resolution of the measurement. The uncorrected outer vs inner charge amplitudes are compared to the fully crosstalk-corrected and calibrated energies in Fig. 7.3.

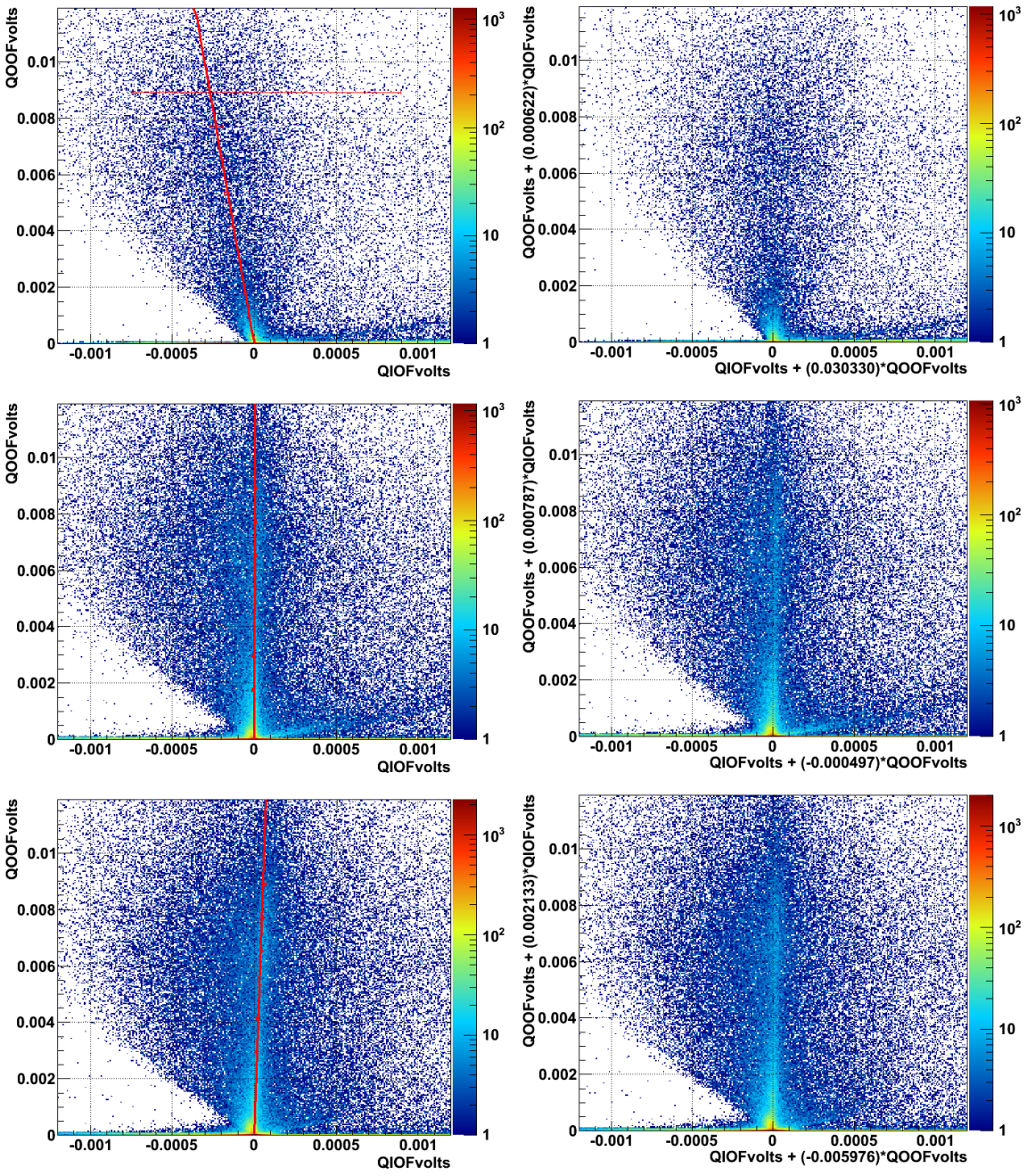

Figure 7.1: (left column) Charge crosstalk from the inner electrode for three Ge detectors: T3Z2 (top row), T3Z4 (center row), and T3Z5 (bottom row). Events with charge collected primarily by the outer electrode align along the y-axis. A nearly-vertical event band is tilted slightly toward more negative or positive values of reconstructed inner charge energy as the energy in the outer electrode increases. The red line represents a linear fit to this band of events clustered around the y-axis. The slope of this line determines the correction factor. (right column) Crosstalk-corrected outer electrode energy vs inner electrode energy.

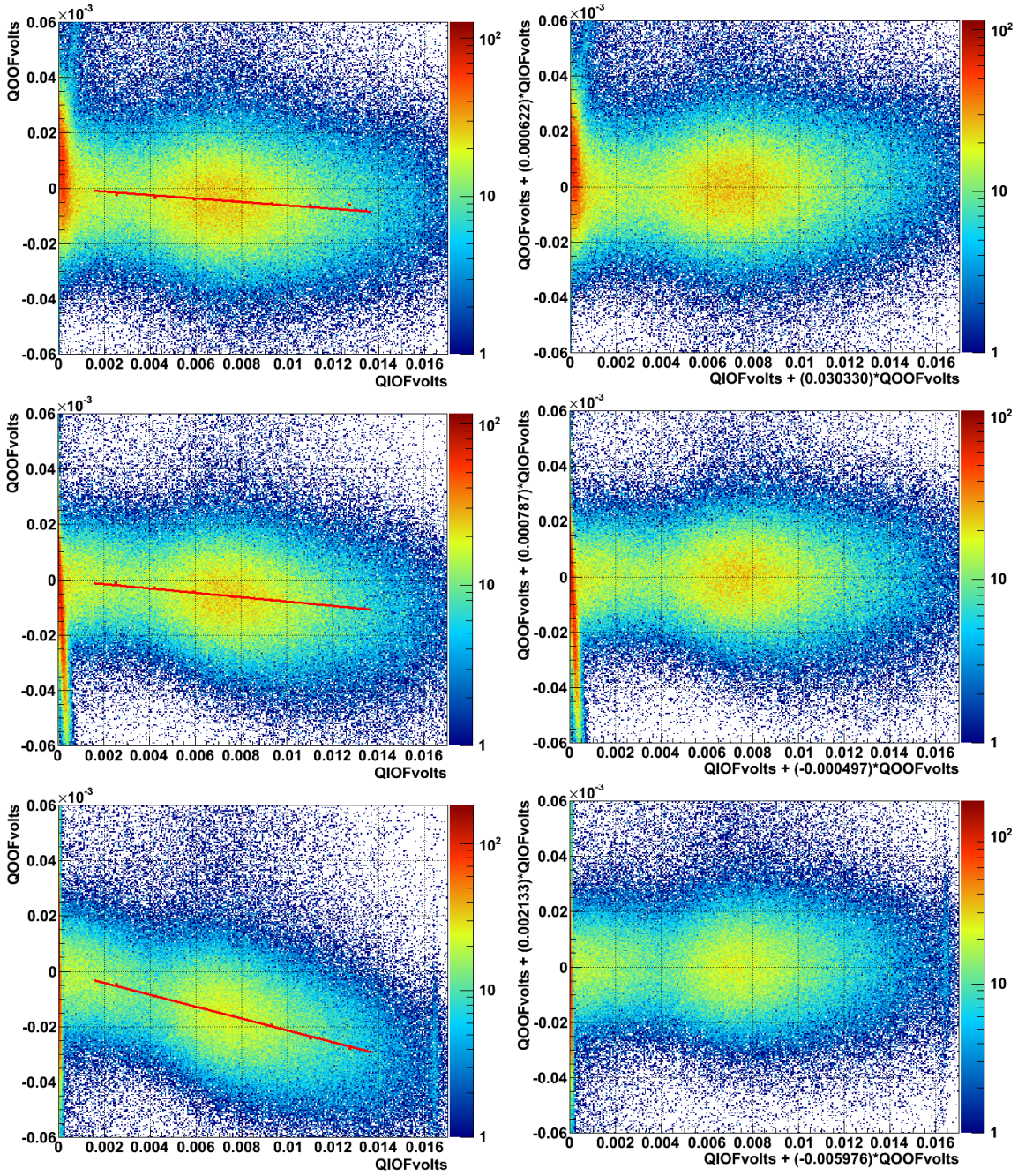

Figure 7.2: (left column) Charge crosstalk from the outer electrode for three Ge detectors: T3Z2 (top row), T3Z4 (center row), and T3Z5 (bottom row). Events with charge collected primarily by the inner electrode align along the x-axis. This band of events tilts down slightly toward more negative values of reconstructed outer charge as the energy in the inner electrode increases. The red line represents a linear fit to this band of events clustered around the x-axis. The slope of this line determines the correction factor. (right column) Crosstalk-corrected outer electrode energy vs inner electrode energy.

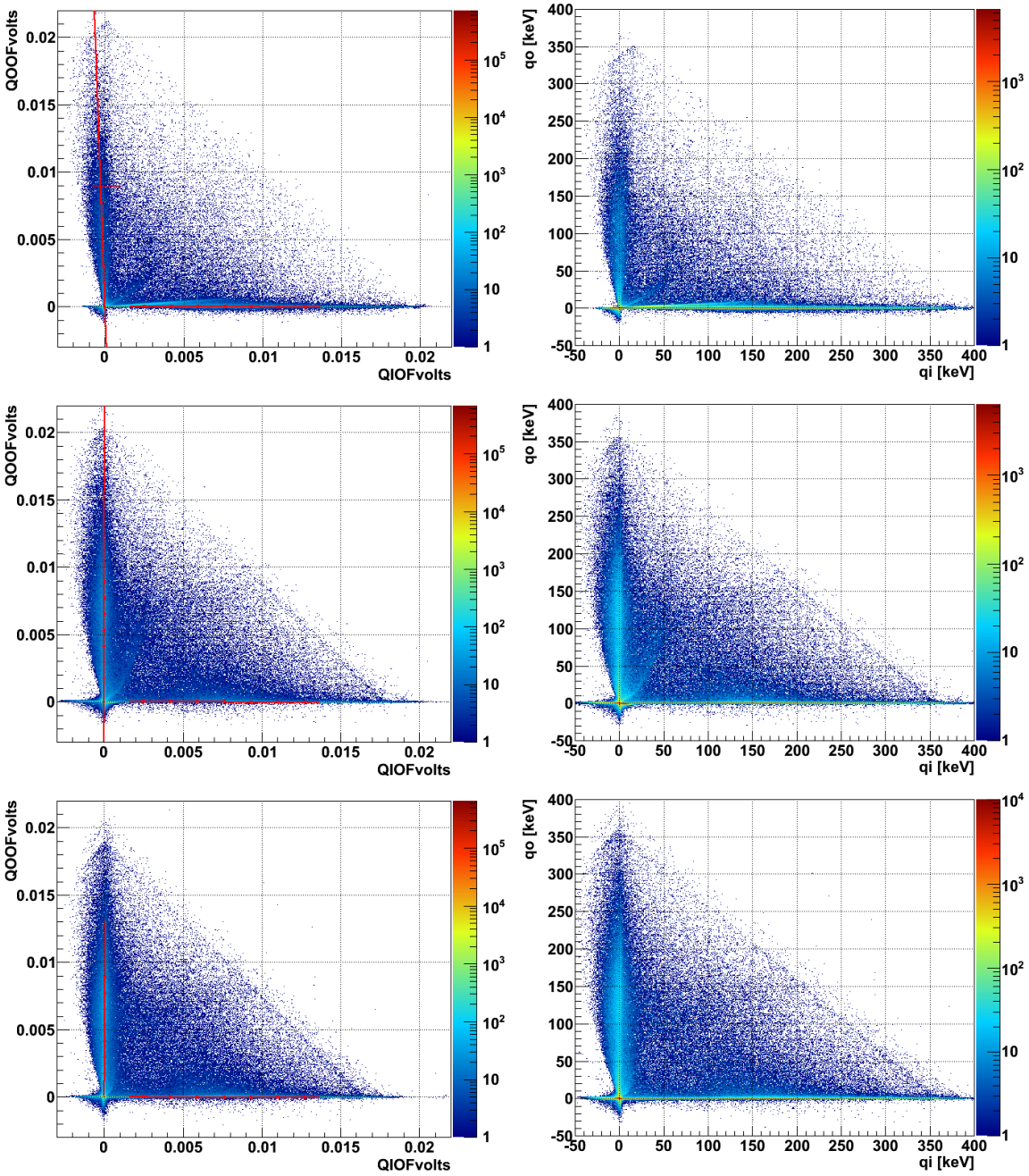

Figure 7.3: (left column) Outer vs inner charge electrode amplitude before crosstalk correction for the three Ge detectors in Tower 3: T3Z2 (top row), T3Z4 (center row), and T3Z5 (bottom row). (right column) Crosstalk-corrected and calibrated outer vs inner electrode charge energy.

Position dependence

A more obvious smearing effect is a ∼5% position dependence in the reconstructed charge signal, most visible as a y-dependence and a weaker x-dependence (shown in Figs. 7.4 and 7.5). The y-position is reconstructed using phonon timing delay quantities defined in Sec. 5.5.2. As this dependence is easily corrected, its cause has not been studied in great detail. The most plausible explanation suggested so far is that it may be a result of position-dependence in the TES ion implantation or that it is a sign of degraded neutralization. This correction is performed by first selecting a rectangular region in OF-derived inner electrode charge amplitude vs y-delay that contains most of the events from the 356 keV line. This distribution is then binned in delay and fit to a Gaussian function of amplitude (Fig. 7.6). These fits are then used as inputs to a fourth-degree polynomial fit to the centroid of these fits to the 356 keV line, as a function of position (Fig. 7.7). The ratio of this polynomial to a straight line gives a correction factor to straighten the line and remove the position dependence. This procedure is then repeated for the x-delay, along which the signal shows only a very weak position dependence, and a final position correction factor is applied. To set the overall calibration for the ionization signal, the position-corrected OF amplitudes are scaled such that the 356 keV spectral line appears at the correct energy, and the other nearby lines are checked to make certain they are also well matched (shown in 7.8).

Final calibration

The final step is to perform a cross calibration of the inner and outer electrode amplitudes using events whose energy is shared between the two electrodes. This is necessary as very few 356 keV Ba events deposit their energy entirely in the outer electrode. Since the population of shared events is also rather small, the calibration of the outer electrode is less precise than that for the inner electrode. This is of no significant concern since this channel is primarily useful as a veto and the charge signal from this channel is not used directly in the WIMP-search analysis.

In the silicon detectors, many 356 keV gammas are not completely contained within

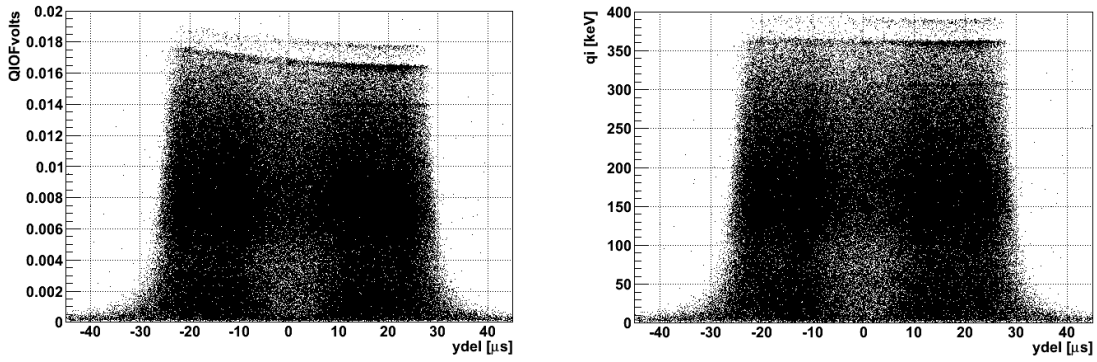

Figure 7.4: Position dependence in the y-direction for the inner charge electrode signal. Above the continuum, spectral lines characteristic of the ^{133}Ba calibration source are visible, the most prominent at 356 keV. (left) The uncorrected signal exhibits clear position dependence in the 356 keV line. (right) Position-corrected and calibrated signal.

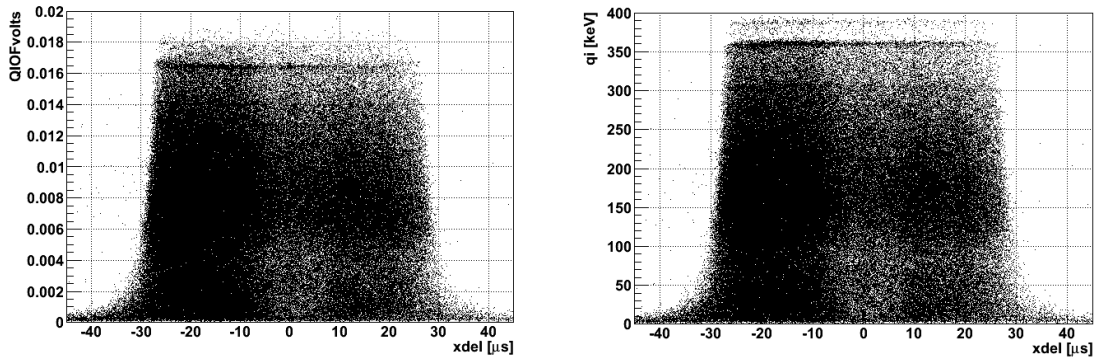

Figure 7.5: Position dependence in the x-direction for the inner charge electrode signal. (left) The uncorrected signal exhibits only minor position dependence in the 356 keV line. (right) Position-corrected and calibrated signal.

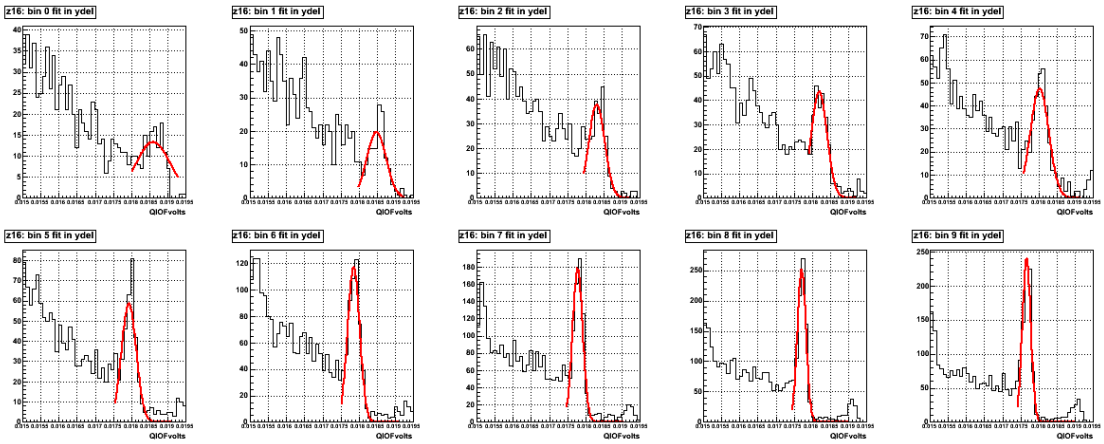

Figure 7.6: Panels show consecutive slices in y-delay (position) and Gaussian fits to the local amplitude (in uncalibrated OF-volts) of the 356 keV line. The μ and σ estimates from these fits are used as input data points for the polynomial fit in Fig. 7.7.

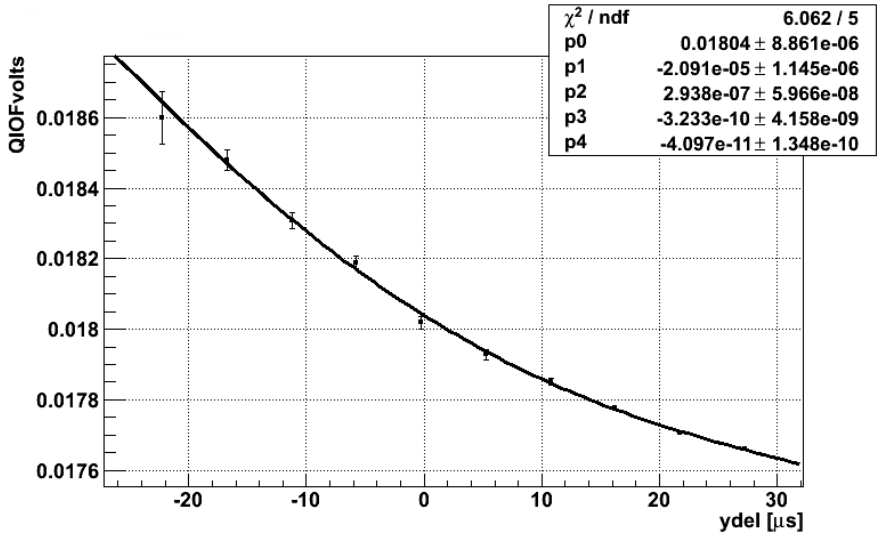

Figure 7.7: Polynomial fit to the local Gaussian-fit amplitudes of the 356 keV γ calibration line, in bins of y-position. This polynomial is factored into the calibration to remove the position dependence of the charge signal. Shown for T3Z4.

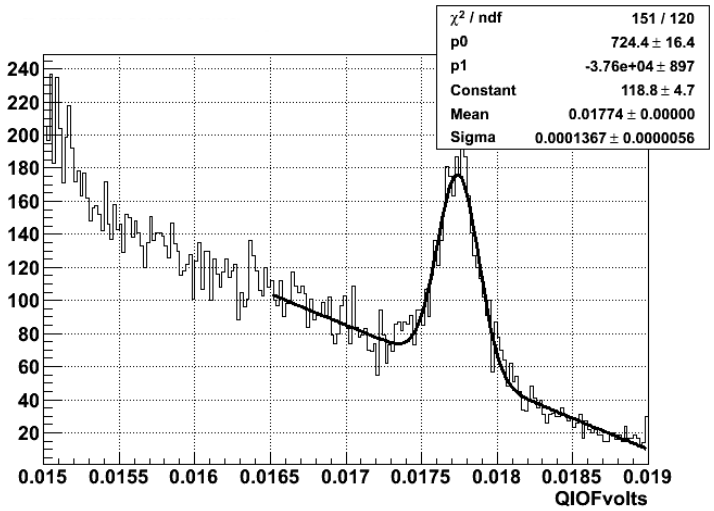

Figure 7.8: Final ionization calibration factor in T3Z4 (Ge). After crosstalk and position dependence are removed, the 356 keV line is identified and fit by a Gaussian with a linear background. The mean of this fit in OF-volts is calibrated to 356 keV.

a single detector due to the lower stopping power of the material. Thus the calibration is performed by looking at 356 keV gammas that are shared between two neighboring detectors, much like the cross-calibration of the inner and outer charge electrodes (Fig. 7.9). In most cases the Si detector will have a neighboring Ge detector, but even in the case of T2Z1, which has only Si neighbors, at least a faint line is visible in the sum of the ionization signals from the two detectors. Rarely, in earlier runs, no line was visible in one Si detector's shared events and the charge calibrations were taken to be equal across Si detectors. This limitation did not affect the main 5-tower runs under study.

The primary result of this calibration of the ionization signal is an electron-equivalent recoil energy, the "ionization energy" E_Q. This quantity gives one measure of the recoil energy for electron recoil events and helps characterize the energy partitioning for all events.

7.2 Phonon calibration

The phonon signal's energy calibration is defined relative to the ionization signal rather than independently with spectral peaks. This method of interdependent calibration is critical in

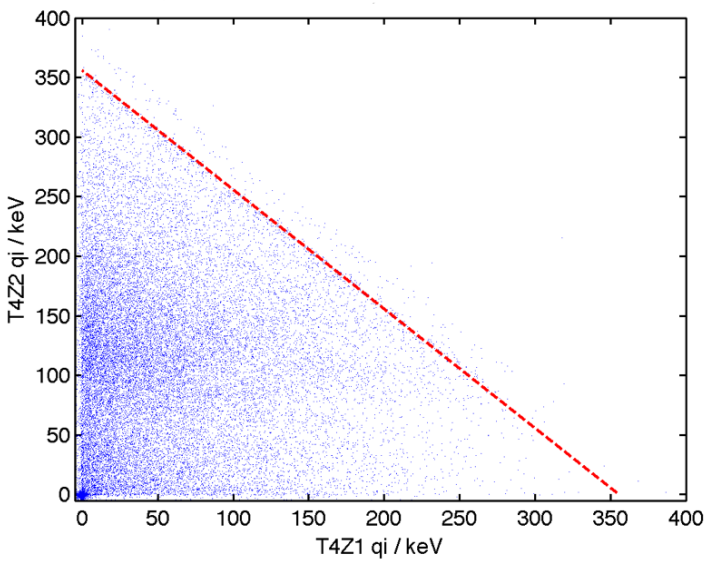

Figure 7.9: Events shared between T4Z1 (Si) and T4Z2 (Ge). The inner charge electrode energy for the two adjacent detectors is shown on each axis. Spectral lines from the ^{133}Ba source may not visible be in Si due to its lower stopping power than Ge. The dotted red line shows a calibration of the summed energy from the two detectors at the 356 keV line.

order to have a well-defined ionization yield parameter (derived from both signals; detailed in Sec. 7.3), which must be near unity for electron recoils in the analysis energy range of 10-100 keV. As discussed in Sec. 5.5.2, phonon pulses in this energy range have very different shapes than those from much higher energy γ energies, such as those in the 356 keV line. In the absence of clear spectral lines at lower energies, calibrating the phonon signal relative to ionization is the best way to ensure well-behaved yield in the energy range of interest to WIMP searches.

Bulk electron recoils from the ^{133}Ba source are used as the calibration sample. The optimal-filtered signals from the four phonon channels are adjusted with individual gain factors to account for channel-to-channel sensitivities that vary at the level of $\sim 10\%$. This is done examining the energy partition quantities defined in Sec. 5.5.2, and ensuring roughly equal amplitudes in each quadrant, so that the "box" in y-partition vs x-partition space is square. The sum of these adjusted signals is matched to the value of the calibrated

ionization signal in order to minimize the width of the ionization yield band. In doing so, the yield parameter is calibrated to unity, on average, for bulk electron recoils in the energy range of interest. As discussed in Sec. 5.3, Luke phonons are produced when electrons and holes are drifted across the detector by the applied electric field. The produced amount of these Luke phonons relative to the amount of primary phonons strongly characterizes whether they result from an electron recoil or a nuclear recoil. This calibration includes the contribution of these Luke phonons from electron recoil events, and as such it results in an "electron-equivalent" recoil energy, given in units of $\mathrm{keV_{ee}}$.

7.2.1 Energy and position correction

The shape of observed phonon pulses depends strongly on their position and energy. Both of these factors lead to smearing of the energies reconstructed by the optimal filter algorithm, which assumes a single, fixed pulse shape. Two pulses with the same amplitude but different shapes are assigned different energies. This energy smearing is visible in the diffuse form of the electron recoil yield band in the left panel of Fig. 7.10. Timing quantities derived from bin-by-bin walks along digitized pulses are also sensitive to pulse shape, and are similarly compromised.

A phonon correction table is used to reduce these strong position and energy dependences. This table is built to contain information about how the mean values of phonon-derived parameters vary with event location and energy. Each event's phonon parameter values are compared against the table and bulk trends are factored out, resulting in corrected parameters that have much weaker dependence on position and energy. This procedure results in vastly improved resolutions. Thus the electron recoil band constructed using these energy quantities is much tighter, with a consistent mean and a more well-defined and slowly-varying Gaussian width (Fig. 7.10, right panel).

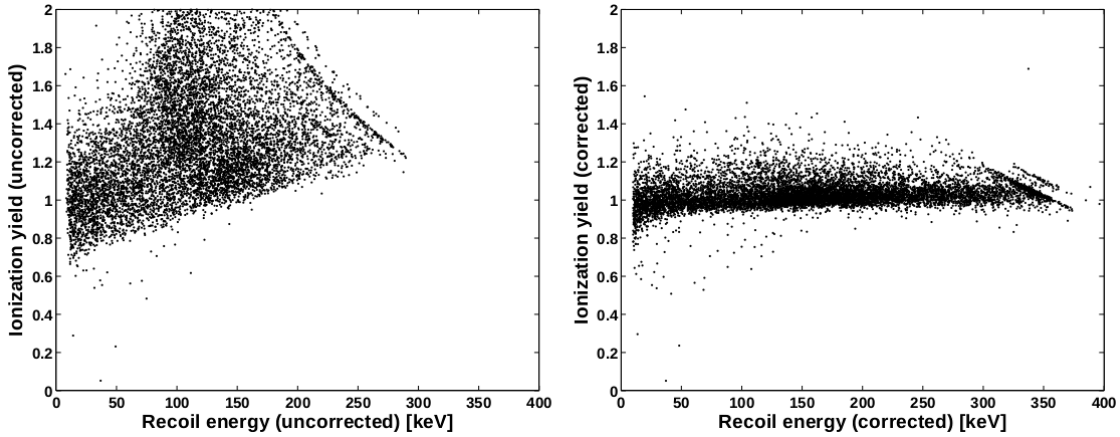

Figure 7.10: Ionization yield vs recoil energy for T1Z2, a Ge detector, in ^{133}Ba calibration data from the first 5-tower run. (left) Prior to applying the phonon correction table. (right) After applying the phonon correction table.

7.2.2 Deviations from an ideal phonon detector

An idealized picture of phonon detection was presented in Sec. 5.3, where we expect to observe the true total phonon signal, with each of the three contributions to the signal being detected at 100% efficiency.

$$E_P = E_{\text{prim.}} + E_{\text{recomb.}} + E_{\text{Luke}} \tag{7.1}$$

$$= (E_R - N_Q E_g) + N_Q E_g + N_Q e V_b \tag{7.2}$$

$$= E_R + E_Q \frac{eV_b}{\epsilon} \tag{7.3}$$

The first potential problem with this picture is that each of the three phonon generation mechanisms produce phonons with different energy spectra, which may also be produced and absorbed by the collection system at different times. The Al collection fins are sensitive only to athermal phonons with energies more than twice the superconducting band gap in Al, $\sim$0.35 meV. Phonons at lower energies are not detected and result only in a slight increase in the crystal's temperature over timescales too long to have any measurable effect within the phonon pulse reconstruction time window.

These differences could affect the measurement in several ways. Because Luke phonons have different energy spectra and arrival times relative to primary phonons, their collection efficiency by a ZIP detector may be more or less than that for primary phonons. By the same token, recombination phonons may produce a different response than either primary or Luke phonons. Of even greater concern is that the response to primary phonons may vary depending on whether they result from an electron or nuclear recoil, given their clearly different energy spectra. The expected degree of difference in all cases is not well known, both because the detailed detector response is difficult to model, and because these differences may depend on details of the specific technique used to reconstruct the pulses.

When accounting for relative efficiencies of contributions to the phonon signal we must take into account that only a fraction f_Q of the total charge is observed. Uncollected charge carriers may be trapped within the crystal lattice or recombined before the electric field is able to separate them.

Taking into account the above effects, which can suppress or enhance the detector's sensitivity to recombination or Luke phonons, we write,

$$E_P = \eta_{\mathrm{NR}} \left(E_R - N_Q E_g\right) + \eta_{\mathrm{recomb.}} \left(f_Q N_Q\right) E_g + \eta_{\mathrm{Luke}} \left(f_Q N_Q\right) eV_b, \tag{7.4}$$

where $\eta_{\mathrm{recomb.}}$ and η_{Luke} represent the detector's relative response to recombination and Luke phonons relative to that for primary phonons, and η_{NR} represents the relative response to primary phonons from nuclear recoils.

As described above in Sec. 7.1, the ionization energy scale is calibrated directly from photon spectral lines. Therefore linear ionization collection inefficiencies are folded into the calibration and do not affect the electron-equivalent ionization energy scale. These ionization losses instead show up in the phonon energy scale, where ionization inefficiency could lead to subtraction of an incorrect Luke phonon contribution. Inefficiency in phonon collection for nuclear recoils vs that for electron recoils would then distort the energy scale for nuclear recoils. We will return to Eq. 7.4 after examining observed deviations in the energy scale for nuclear recoils compared to expectations.

7.3 Ionization yield discrimination

Ionization yield is the CDMS II ZIP's primary discriminator between electron recoils and nuclear recoils, and is therefore of central importance to the analysis of any set of WIMP-search data. This parameter is defined as

$$y \equiv \frac{E_Q}{E_R} = \frac{E_Q}{E_P - \frac{eV_b}{\epsilon} E_Q}, \tag{7.5}$$

where V_b is the bias voltage and ϵ is the mean electron-recoil energy required to generate a single electron-hole pair in a specific target material. The normalization is such that the average yield is unity for an electron recoil of any energy. Equivalently, this states that E_Q is a reliable estimator of an electron recoil's true recoil energy E_R.

The factor ϵ is significantly larger than the band gap E_g. Only a minority of the deposited energy in a particle interaction goes directly into the production of electron-hole pairs, and the overall energy loss is split between several competing processes. At first, the incident particle excites electrons and holes into the conduction band, resulting in an effectively instantaneous cascade, which continues until the energy of individual charge carriers is below the threshold for ionization. At the same time, these electrons and holes interact with the crystal lattice and produce optical phonons. Eventually, the charge carriers' kinetic energy falls below the threshold energy for ionization, at which point they no longer couple to optical phonon modes and instead dissipate their residual kinetic energy through emission of acoustic phonons over an extended time scale of $\sim$10 ps. In total, the ϵ factor is the sum of three components:

1. E_g to excite an electron-hole pair into the conduction band. At base temperature the band gap is 1.17 eV for Si and 0.74 eV for Ge.

2. Residual kinetic energy ($1.8E_g$) transferred to acoustic phonons, under the assumption that the carriers uniformly populate momentum space.

3. Optical phonons deposit some fraction of an eV in energy, given by $r\hbar\omega$, where r

gives the number of optical phonon scatters per ionizing event, and ω_R is the Raman phonon frequency.

In total, this model (originated by Klein (53)) predicts

$$\epsilon = \frac{14}{5} E_g + r\hbar\omega_R \tag{7.6}$$

This factor depends on the type of incident particle and the target material (shown in Fig. 7.11a). Its temperature dependence tracks known temperature variations in the band gap (shown in 7.11b). For CDMS, the electron recoils of interest are those resulting from electrons and photons. For these particles, the consensus values adopted by CDMS at base temperature are $\epsilon_{\mathrm{Ge}} = 3.0\,\mathrm{eV}$ and $\epsilon_{\mathrm{Si}} = 3.82\,\mathrm{eV}$. These values are consistent with measurements (54; 55) and two theoretical models by Klein/Varshni (53; 56) and Thurmond (57).

The calibration of ^{133}Ba electron recoils is used to define the relative scale of the ionization yield for nuclear recoils. Calibration of the yield thus results in the clustering of several recoil event type populations, each residing in its own band in the yield vs. recoil energy plane.

The recoil energy E_R used in the band definitions is found on an event-by-event basis by subtracting the Luke phonon component from the total phonon signal, as measured through the charge channels. The remaining phonon signal is entirely derived from energy transferred from the incident particle, rather than the applied electric field. It is a measure of the recoil energy.

7.3.1 Electron recoil band definition

Data from ^{133}Ba gamma calibration are used to define the statistical distribution of electron recoils populating the electron recoil band, also referred to as the "gamma band." A large fraction of these events are photoelectric absorption or Compton scatters of photons off electrons in the crystal, though they may also come from Coulomb scattering of electrons

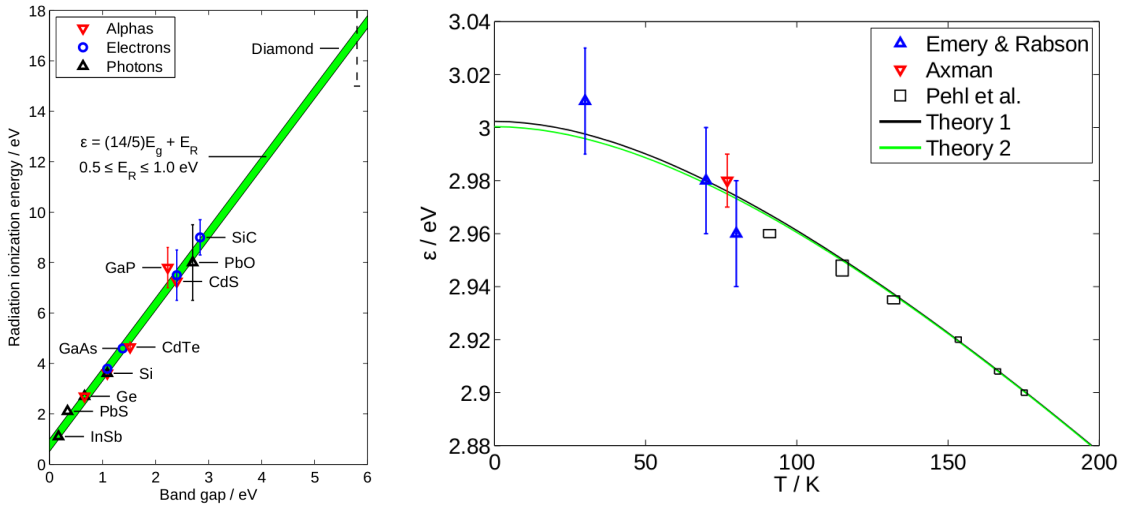

(a) (b)

Figure 7.11: (a) Electron recoil ionization energy per charge carrier pair (ϵ) vs band gap energy for several materials, taken from (53). The green band represents uncertainty in the nearly-linear relation due to varying optical phonon losses (assumed to be Raman phonons, and so the notation, as used in the inset text, is often $E_R = r\hbar\omega$) in the range 0.5 to 1.0 keV. Note that this factor is dependent on particle type in Si, while it is relatively insensitive to particle type in Ge. These data points use the band gap at base temperature.

(b) ϵ vs temperature for Ge, as modeled by Klein (58) with Varshni's (56) parameters (the darker "Theory 1" curve, taking $E_R = r\hbar\omega = 0.927\,\text{eV}$), and more recent parameters from Thurmond (57) (lighter "Theory 2" curve, taking $E_R = 0.918\,\text{eV}$). In both cases the optical phonon losses E_R have been varied to best fit the data (54; 55).

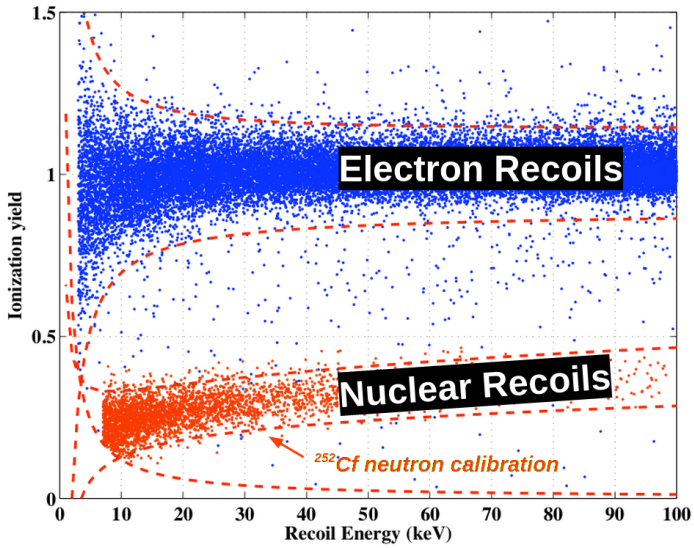

Figure 7.12: Electron recoil and nuclear bands in ionization yield vs recoil energy. The dark blue events mostly populating the electron recoil band (dotted lines $\pm 3\sigma$ from the mean at unity yield) are sampled from ^{133}Ba calibration data, while the lighter red events populating the nuclear recoil band (dotted line $\pm 2\sigma$ from the mean at yield ~ 0.3) are sampled from ^{252}Cf calibration data.

in the detector bulk. The selection of recoil events is binned in energy separately for each detector. The data falling into each energy bin are then fit with a Gaussian in the yield parameter. The mean and standard deviation parameters from these fits for each energy bin are then fit to simple, smooth functions of the recoil energy,

$$\mu_{\mathrm{ER}} = a_1 E_R^{a_2} \tag{7.7}$$

$$\sigma_{\mathrm{ER}} = \frac{b_1^2 E_R^{b_2} + b_3^2}{E_R}. \tag{7.8}$$

With these functional forms established, the standard electron recoil band is defined as that region lying between the upper and lower $\pm 2\sigma$ bounds away from the mean of the distribution. As seen in Fig. 7.12, the band widens at low energy, a result of increasing fractional noise in both the phonon and ionization signals at lower energy. It is primarily this noise that characterizes the width of the band.

7.3.2 Nuclear recoil band definition

The band constituting the region containing nuclear recoils is defined in a similar way, using a ^{252}Cf neutron source. Since the ^{252}Cf source emits γ-rays, there is a portion of its event population found in the ER band. The neutrons populate a band with yield ~ 0.3 for much of the 10-100 keV energy range. The functional forms used for the fits to the mean and width of the band are again empirically determined, and slightly different than those for the electron recoil band:

$$\mu_{\mathrm{NR}} = a_1 E_R^{a_2} \tag{7.9}$$

$$\sigma_{\mathrm{NR}} = \frac{b_1^2 E_R^{b_2} + b_3^2}{E_R} + \begin{cases} b_1 E_R^{b_2} & \text{if } E_R < E_{\mathrm{cutoff}} \\ b_1 E_{\mathrm{cutoff}}^{b_2} & \text{if } E_R \geq E_{\mathrm{cutoff}} \end{cases} \tag{7.10}$$

A simple power law form for the width of the band will result in a widening at energies above approximately 60 keV, where neutron statistics are poor and more electron recoil events that fall at lower yield values contaminate the sample. This widening is not physically motivated, as both the phonon and ionization channels have nearly constant energy resolution at these higher energies. To address this, the width is fixed to remain constant at the value it takes on at some cutoff energy for all energies above the cutoff. This cutoff energy is empirically determined and generally lies in the 20-40 keV range for each detector. The resulting $\pm 2\sigma$ bands are shown in Fig. 7.12.

7.3.3 Theoretical predictions

The empirical bands in the yield vs recoil energy plane established on these ^{252}Cf calibration data have a form generally consistent with expectations, when compared to the best available theoretically motivated models, outlined below.

Lindhard theory

It is useful to define a "quenching factor" Q as the ratio of the ionization yield from a nuclear recoil to that from an electron recoil of the same energy. In Si and Ge crystals where the electron recoils have unity ionization yield, the quenching factor is simply the ionization yield for nuclear recoils, $Q = y(E_R)_{\mathrm{NR}}$.

The most commonly-cited theoretical model of the quenching factor in semiconductor crystals is that of Lindhard *et al.* (59). This model was among the earliest attempts to quantitatively evaluate the competing energy loss mechanisms of slow ($< 100\,\mathrm{keV}$), heavy ions moving through a target material. These losses are characterized by distinct electronic and nuclear stopping powers. In general, the nuclear contribution to a heavy ion's energy loss $(dE/dx)_n$ resulting from the target's nuclear stopping power S_n depends on details of both the projectile and target. A more general form can be found by substituting the dimensionless variables ϵ and ρ for the ion's energy E and range R, which can be written as

$$\epsilon = C_{\mathrm{TF}} \frac{A_T}{A_{\mathrm{tot}}} \frac{E/(2E_B)}{Z_P Z_T Z^{1/2}} \tag{7.11}$$

$$\rho = 4\pi \left(a_B C_{\mathrm{TF}}\right)^2 \frac{A_P A_T}{A_{\mathrm{tot}}^2} \frac{RN}{Z}, \tag{7.12}$$

if $Z = Z_P^{2/3} + Z_T^{2/3}$ and $A_{\mathrm{tot}} = A_P + A_T$. Here N is the target material's number density, Z_P (A_P) is the atomic (mass) number of the ion projectile, Z_T (A_T) is that of the target, a_B and E_B are the Bohr radius and energy, respectively, and $C_{\mathrm{TF}} = (9\pi^2/2^7)^{1/3}$ is the Thomas-Fermi constant. This simplified notation is used in more recent studies of nuclear stopping power such as (60). In this dimensionless form, the nuclear portion of the energy loss $(d\epsilon/d\rho)_n$ depends only on the Thomas-Fermi interaction potential and is this a "universal" function of energy for any material, $f(\epsilon)$. This function has been calculated numerically by multiple groups (61; 60). It can be converted back to physical units for various target materials, several of which are shown in Fig. 7.13.

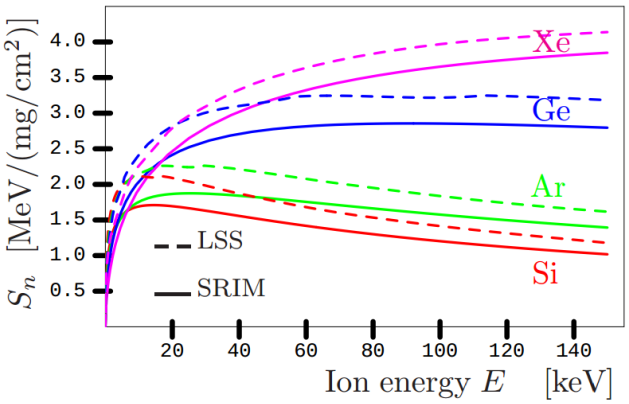

Figure 7.13: Nuclear stopping power S_n as a function of the kinetic energy of the recoiling ion. The dotted lines show the Lindhard form (also referred to as LSS, or Lindhard-Sharff-Schiøtt, after the coauthors). The solid lines are modern numerical calculations using SRIM (Stopping Range of Ions in Matter) code from Ziegler et al.(62), as presented in (60).

Electronic stopping power S_e has been studied extensively and is relatively well understood. Various approximations are in good agreement in the energy range of interest for WIMP searches in Si and Ge crystals, where S_e has a relatively simple dependence on the energy of the incident particle. In Lindhard's dimensionless units (Eqs. 7.11,7.12), an ion's electronic energy loss $(d\epsilon/d\rho)_e = \kappa\sqrt{\epsilon}$, where κ is a proportionality constant depending only on Z_P, A_P, Z_T, A_T, and the electron mass m_e.

It is assumed that the electronic and nuclear stopping powers can be calculated independently. This is generally a reasonable assumption, as electron excitations occur almost exclusively at impact parameters much larger than those for nuclear collisions.[1] Under this assumption the Lindhard model gives a nuclear recoil yield parametrization for a nucleus of atomic number Z and mass number A:

$$y(E_R)_{\mathrm{NR}} = \frac{kg(\epsilon(E_R))}{1 + kg(\epsilon(E_R))} \tag{7.13}$$

[1] This approximation works well for most energies, but it fails at very low energies. Any two interacting nuclei experience a screened Coulomb repulsion. As a result, the available range of impact parameters for target electrons in the projectile's screened Coulomb field is restricted; thus the two energy loss mechanisms are not completely independent. This can result in a greatly suppressed electronic stopping power S_e, but only when the velocity of the incoming particle is small compared with the average velocities of electrons in the material (63).

where

$$\epsilon(E_R) = 11.5E_R[\text{keV}]Z^{-7/3}, \quad k = 0.133Z^{2/3}A^{-1/2},$$

and $g(\epsilon(E_R))$ is given by

$$g(\epsilon) = 3\epsilon^{0.15} + 0.7\epsilon^{0.6} + \epsilon. \tag{7.14}$$

The semi-empirical k parameter is often allowed to vary slightly, and the current best fit of the Lindhard form to several Ge data sets (detailed below in Fig. 7.17) estimates $k = 0.159$. This form matches the measured nuclear recoil bands for CDMS II Ge detectors very well throughout the traditional analysis energy range of 10-100 keV, shown in Fig. 7.14. A more detailed examination of the compatibility of this model with Ge yield measurements down to lower energies is presented in Sec. 7.4.

In Si detectors the agreement is not as good, particularly at high energies where the measured nuclear recoil band dips to significantly lower yield than predicted by the model. This discrepancy may be in part due to the low electric fields in the detectors when biased at the operational 4 V for these datasets, leading to reduced ionization collection in Si. While the mechanism for such an inefficiency is not completely understood and its energy dependence is unknown, this hypothesis is supported by comparisons to data taken at much higher fields (2000 V/cm) by a Si ionization detector (64), which agree very well with the Lindhard model, shown in Fig. 7.15. Moreover, the shape of the bias dependence around fields of ± 4 V/cm in plots of phonon channel energy vs charge electrode bias for some early test runs of 2.54 cm thick Si detectors (shown in Fig. 7.16a) suggests incomplete ionization collection at the bias voltage used in CDMS II running. This is in stark contrast with the apparent complete ionization collection in Ge at much lower bias voltages, shown in Fig. 7.16b.

Alternate models

The Lindhard model has not been shown to be accurate at recoil energies in the sub-keV range, where uncertainties in the theoretical derivation become larger. An alternate

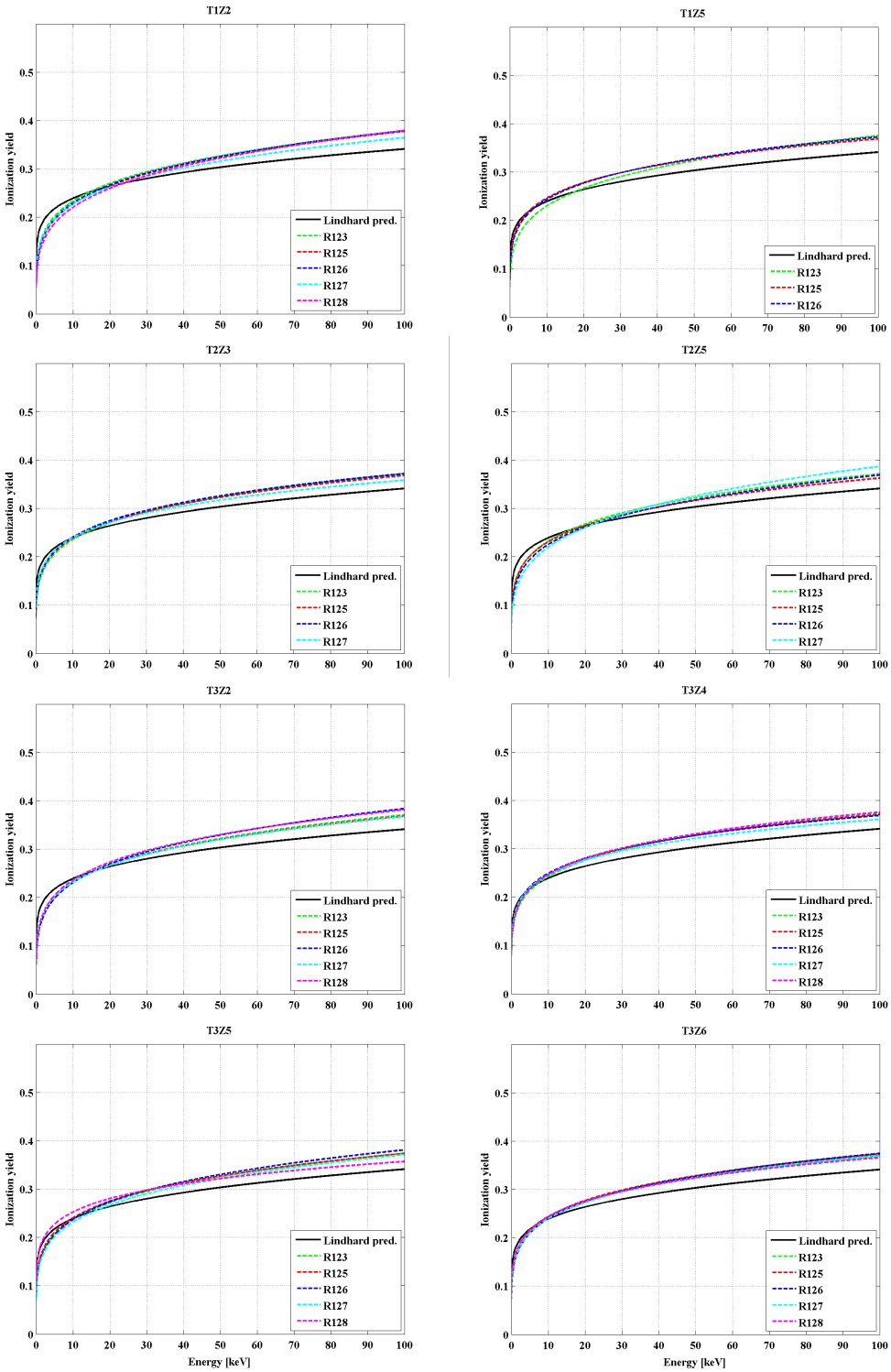

Figure 7.14: Ionization yield vs recoil energy for Ge detectors from Towers 1-3. The Lindhard prediction (solid black curve) is matched very closely throughout this energy range by the nuclear recoil band means for each detector, shown as separate dotted lines for each fridge run. Small run-to-run variations at the level of a few percent are consistent with slight shifts in calibration constants.

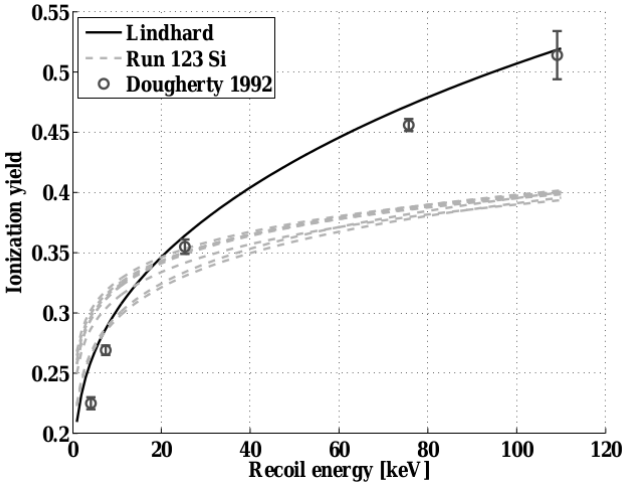

Figure 7.15: Data from an ionization-only Si detector biased to 2000 V/cm (64) are in close agreement with the form predicted by Lindhard theory, shown as a solid line. The dashed curves represent the means of the fitted nuclear recoil yield bands for the CDMS II Si detectors as measured in the first 5-tower run. The imperfect agreement below ∼10 keV can be attributed to the very simple fit functions, but the large difference at higher energies cannot. It may be in part due to the relatively low bias of 4 V/cm used for CDMS II Si detectors, which may lead to incomplete ionization collection (see Fig. 7.16a).

model designed specifically to model low energy interactions in germanium, was proposed by Barker and Mei (66). This model uses newer SRIM-derived (62) "ZBL" stopping power functions (solid lines in Fig. 7.13). The authors calculated the fraction of this S_n contributing to ionization efficiency to be $C_f = 6.2 \times 10^{-2} E_R^{0.15}$. Combined with a SRIM-based treatment of the electronic stopping power S_e, the result is an alternate form of $y(E_R)$, given as

$$y_c(E_R) = \frac{0.14476 \cdot E_R^{0.697747}}{-1.8728 + \exp[E_R^{0.211349}]}, \tag{7.15}$$

where E_R is allowed to take on values from 1 to 100 in units of keV. This model is compared to the Lindhard model and well as measurements from CDMS and several other experiments in Fig. 7.17.

A separate model attempting a best-fit to the data was used by J. I. Collar *et al.* (67; 68) to interpret CoGeNT and CDMS II results, and was later used by CDMS in an analysis

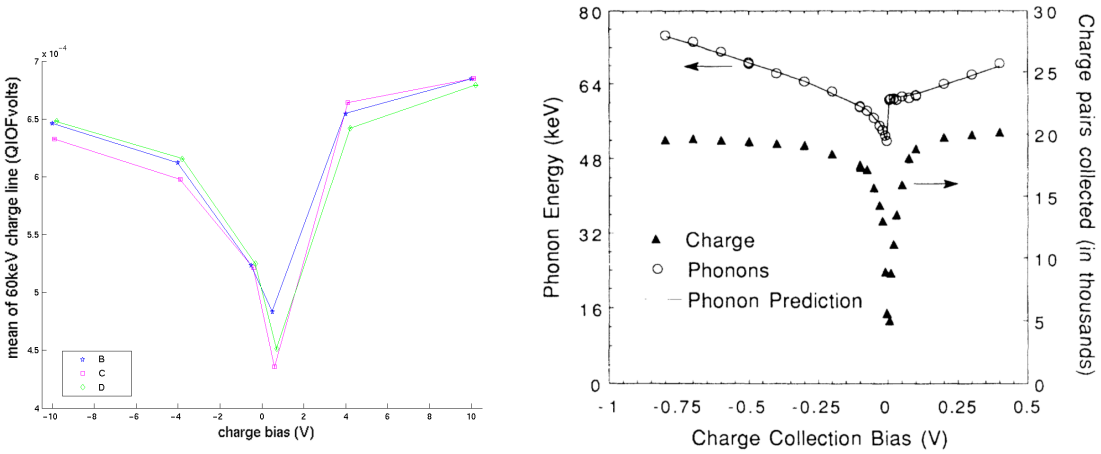

(a) (b)

Figure 7.16: (a) Charge collection vs bias voltage in an early test run of a prototype 2.54 cm thick Si ZIP ("S10C"). The data points show the mean values of fits to the 59.5 keV peak from four collimated ^{241}Am sources shining on the charge side. The selected events are localized to primary phonon channels B, C, and D using phonon position quantities. The charge signal amplitude of the peak appears to continue to increase out to electric fields of $\sim$4 V/cm. The shape is still somewhat slanted at the edges of the plot's range, suggesting ionization collection may be incomplete at the CDMS II operating bias of 4 V in 1 cm thick Si ZIPs.

(b) Charge and phonon collection vs bias voltage for a Ge detector with a thickness of 1 cm, from (65), also calculated for 59.5 keV photons from a 2 µCi ^{241}Am source. Unlike Si, Ge apparently achieves complete charge collection at field strengths as low as 200 mV/cm.

(69) to confirm the possible annual modulation signal reported by CoGeNT (34):

$$E_v = 0.199 E_r^{1.12}, \tag{7.16}$$

where E_v is the visible energy and E_r is the true recoil energy. This parametrization closely follows the Lindhard model with the parameter $k = 0.2$ at low energies and approaches a slope parallel to the Lindhard form with $k = 0.1$ at energies above $\sim$10 keV. This model is shown as a dotted line in Fig. 7.17.

As these alternate models are still relatively new, further validation is needed. The Barker-Mei model is consistent with much of the experimental data and closely follows the $k = 0.159$ Lindhard form at energies below a few tens of keV, but at higher energies it is systematically low. Conversely, the Collar model closely matches Lindhard and other measurements at energies above $\sim$10 keV, as well as Barbeau *et al.* at lower energies, but is significantly higher than measurements from CDMS and the best-fit Lindhard model.

All of the ionization yield models presented are still semi-empirical, and the true functional form may depend significantly on operating conditions such as temperature and bias voltage. Results from high precision neutron beam scattering experiments may present a less muddied picture in the near future.

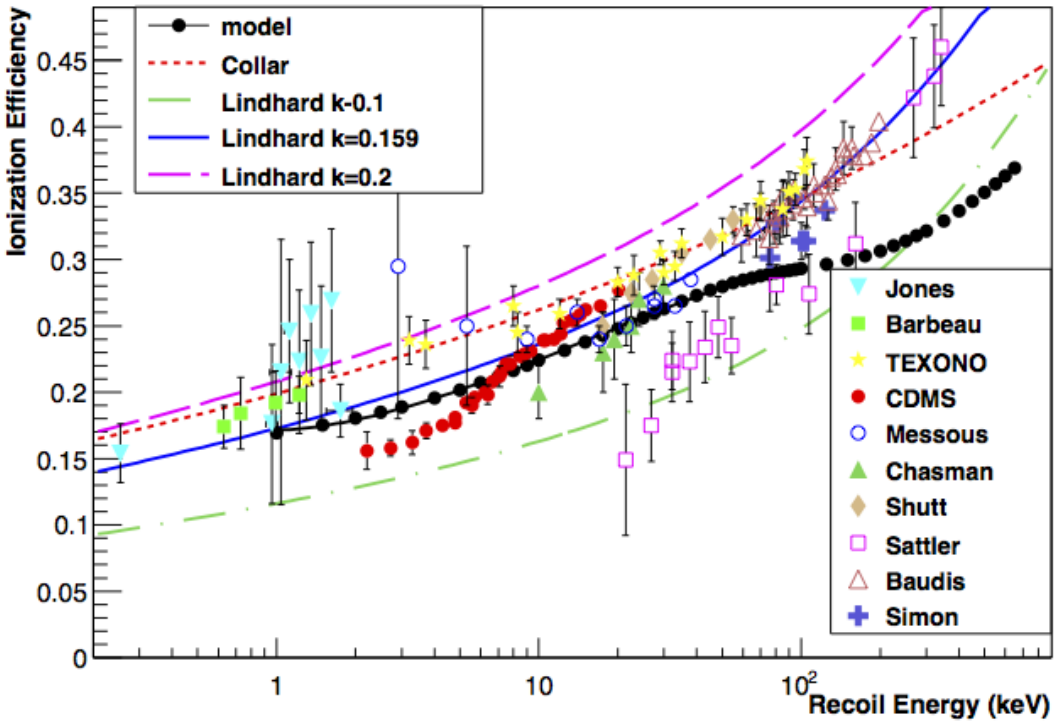

Figure 7.17: Summary of the current state of systematic uncertainties associated with semi-empirical models and measurements of ionization yield vs recoil energy for nuclear recoils in Ge. The primary "model" is that of Barker and Mei (66), as the figure was created for that paper. The dotted line represents the model of Collar *et al.* (67; 68). Measured data points and their error estimates are shown for several experiments (65; 70; 71; 72; 73; 74; 75; 76; 77), at varying levels of agreement with the models. These data come from detectors with a wide range of operating conditions (eg. temperature, voltage bias). The Lindhard form is shown in dashed lines for several values of the semi-empirical k parameter, including some extreme cases and the best-fit value of $k = 0.159$. These CDMS data are derived in Sec. 7.4.

7.4 Yield model-based energy scale correction

By comparing the measured ionization in the ZIPs to the predictions of various yield models, as described in Sec. 7.3.3, one can infer constraints on the magnitude of the systematic uncertainty in the energy scale for nuclear recoils. This is not straightforward, and deviations from predictions could mean several things:

- Standard Lindhard-form yield models may not apply very closely to the CDMS II operating conditions, as most previous measurements cited in Fig. 7.17, used to find the global best-fit parametrization of the Lindhard form, were taken at higher temperatures, higher bias voltage, and higher recoil energies
- We may not have properly accounted for energy-dependent inefficiency in charge collection
- There may be inefficiencies in the phonon measurement, as discussed in 7.2.2.

While we do not understand the precise mechanism behind any discrepancies, we can still estimate the extent to which the energy scale may be distorted by these effects. This study is an auxiliary of the CDMS II low threshold analysis (72) due chiefly to David Moore. Figures and arguments in this section are adapted from a paper in preparation on the nuclear recoil energy scale in CDMS II Ge detectors (78).

The low-energy ionization yield for nuclear recoils is determined by first binning the calibration data in recoil energy. The ionization yield distribution is fit to a Gaussian in each bin, as shown in Fig. 7.18. The recoil energy is determined from the phonon signal alone following (72). For these fits, the distribution is no longer required to lie above noise. Instead, a correction is applied to account for the bias introduced by the optimal filter search as the signal becomes comparable to noise, as follows. For each detector, 5000 randomly-triggered noise traces spaced throughout the calibration data sets are selected. A pulse template of a known energy is generated and added to each noise trace, with a random time offset within the search window. These traces are then processed by the same

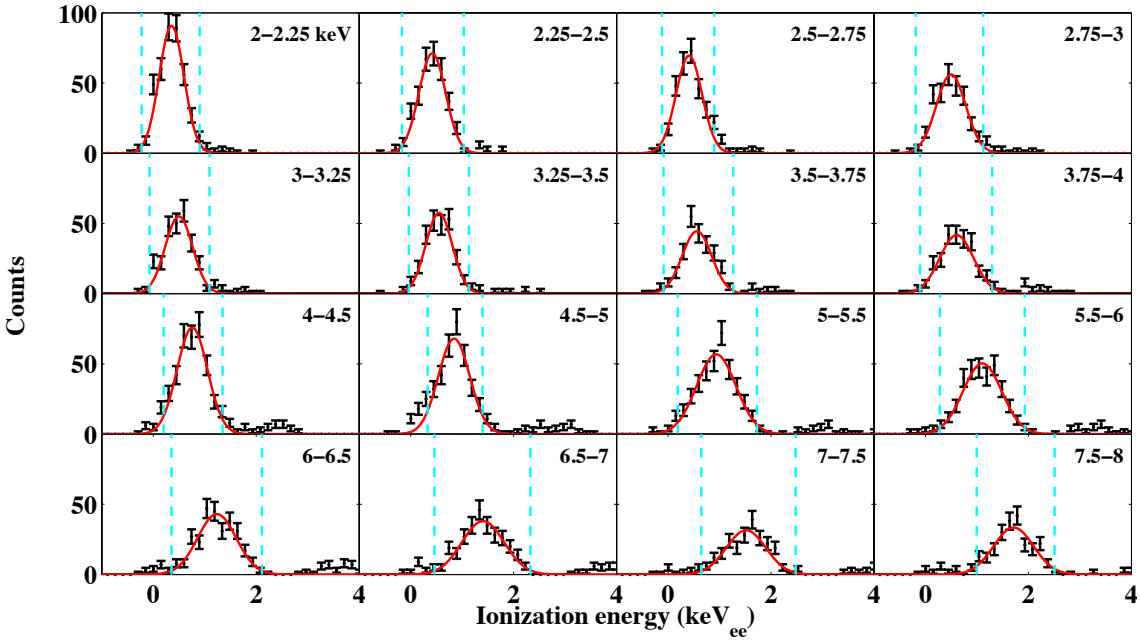

Figure 7.18: Fits to the ionization distribution for nuclear recoils in the ^{252}Cf data for T1Z5 at low energy. The observed counts (error bars) are fit to a Gaussian distribution within the fitting window indicated by the dashed lines.

algorithm used on the calibration data. The distribution of reconstructed energies is fit to a Gaussian to determine the mean reconstructed energy as a function of true energy. An example of this correction for T1Z5 is shown in Fig. 7.19.

A small population of events with ionization energy consistent with noise are observed below the bulk of the nuclear recoil distribution in Fig. 7.18, for certain energy bins (e.g. 6–8 keV$_{ee}$). The majority of these events are expected to arise from interactions at high radius, where the ionization signal can be incompletely collected (72). At low energies, an increasing fraction of these events cannot be rejected by the fiducial volume cut as the signal in the outer ionization electrode becomes comparable to noise. For the fits at low energy shown in Fig. 7.18, such events can lie in the wider fitting window. However, their expected rate is more than an order of magnitude smaller than the counting rate from neutron-induced nuclear recoils at low energy. Thus such events are not expected to provide a significant source of systematic error in the fits.

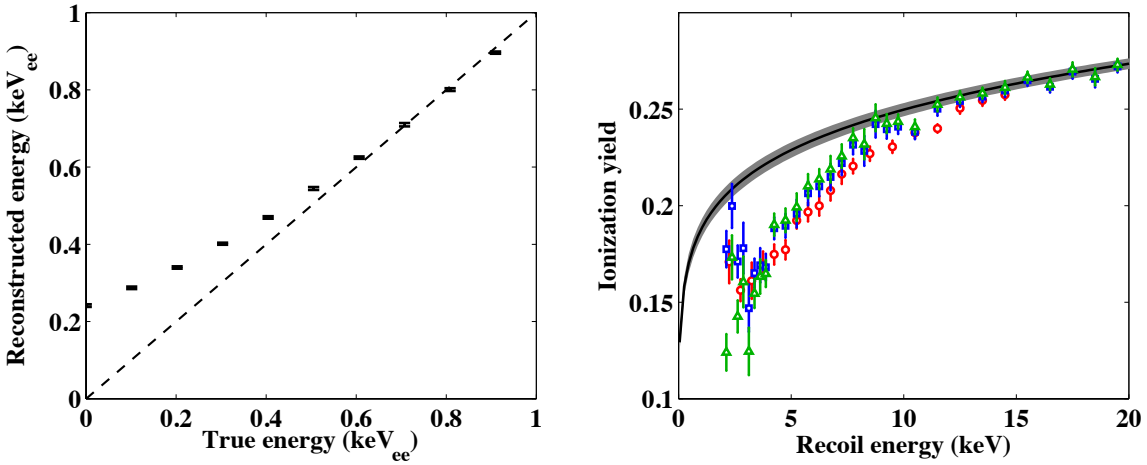

Figure 7.19: (left) Energy reconstructed by the optimal filter search algorithm as a function of true energy for T1Z5. The dashed line shows the expected reconstructed energy in the case of no bias. At low energy, the reconstructed energy is biased to larger values by the search algorithm. (right) Comparison between the measured ionization yield at low energy before (blue, squares) and after (green, triangles) applying the correction for the optimal filter search bias. Good agreement is found between the corrected yields and those determined by the 1-parameter constrained fits to the portion of the distribution $>2\sigma$ above noise (red, circles).

As an independent cross-check at low energy, the mean ionization yield was also determined by fitting a Gaussian to only that portion of the yield distribution for which the ionization energy is $>2\sigma$ above the mean of its associated noise distribution. The amplitude of the Gaussian in each energy bin was fixed using the expected spectrum determined from the Monte Carlo simulations described in Sec. 8.1, and the width was fixed using the ionization energy resolution functions measured from activation lines at 1.3, 10.4 and 66.7 keV$_{ee}$ for each detector. These constraints allowed the mean of the distribution to be determined by a 1-parameter fit, even when only a portion of the high-yield tail was within the fitting window (i.e., $>2\sigma$ above noise). As shown in Fig. 7.19, the results from the 1-parameter constrained fits and those to the full distribution after correcting for the search bias are in close agreement.

Although WIMPs have a negligible probability of scattering more than once in the target material, approximately 30% of neutrons depositing 2-100 keV of total recoil energy

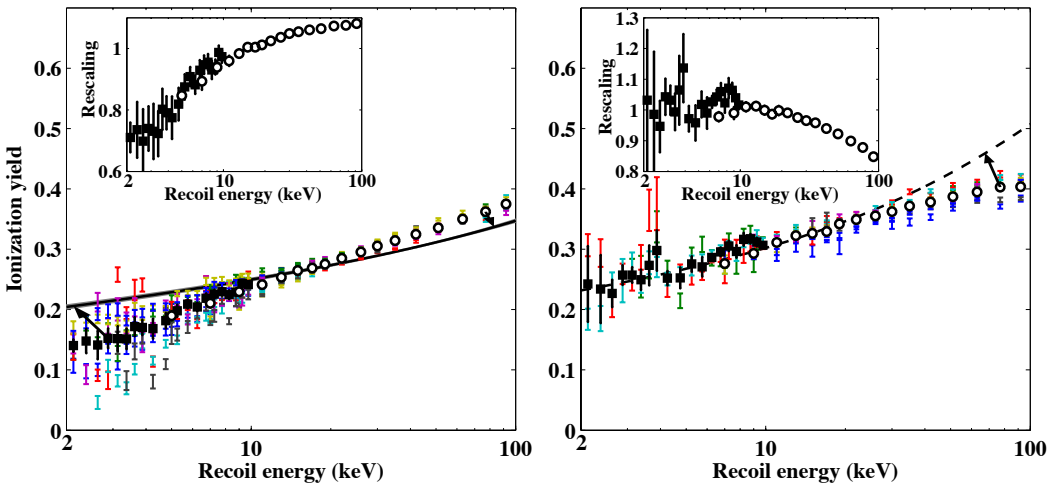

Figure 7.20: Measurements of the ionization yield in CDMS for Ge (left) and Si (right). The error bars indicate the results of the fits to the ionization yield distributions for each detector individually. The ionization yields averaged over detectors are shown for Gaussian fits at high energy (open circles) and fits corrected for the optimal filter search bias at low-energy (filled squares). The solid and dashed lines indicate the parametrizations of previous measurements shown in Fig. 7.17. The insets show the rescaling of the recoil energy scale needed to give agreement with previous measurements of the yield, assuming the ionization collection is the same as previous measurements. The arrows indicate the effect of this rescaling, which changes both the ionization yield and recoil energy.

will interact at multiple locations within a single detector. These multiple-site scatters are not distinguishable from single-site interactions of the same total energy and will lead to systematically lower measured values of the yield. Since the quenching of the nuclear recoil ionization response is an increasing function of recoil energy, a multiple-site interaction where the ionization is divided among several lower energy recoils will produce less ionization than a single recoil of the same total recoil energy. The effect of multiple scattering was determined from the Geant4 simulations of the ^{252}Cf neutron calibrations described in Sec. 8.1 below. For Ge, the measured yields from the neutron calibration data from 2-100 keV are expected to be ∼2-3% lower than for single scatters alone. For Si, the yields are expected to be ∼2-5% lower over the same energy range.

Figure 7.20 shows the ionization yield determined from the Gaussian fits to the nuclear-recoil distribution for each detector, including the correction for multiple scattering determined from Monte Carlo. Above 10 keV, all 14 Ge and 8 Si detectors not suffering from readout issues during the data taking period were used. For the low-energy points, only the 8 Ge detectors and 3 Si detectors with the lowest trigger thresholds were used, following (72). The measured yields for each detector and the average of the measurements over all detectors are shown. Although the yield measurements for different detectors typically agree within 10% at high-energy, there are systematic differences between detectors at low energy that are larger than the statistical errors. To account for these variations, we add a systematic error on the mean yield that is the standard deviation of the measurement for each detector divided by the square root of the number of detectors.

By comparing the CDMS measurements of the yield to the previous measurements of the ionization quenching shown in Fig. 7.17, we can constrain the nuclear recoil phonon energy scale assuming that the ionization measurement in CDMS is consistent with previous measurements. Although differences in ionization quenching or collection are possible due to temperature or field dependent effects, we will neglect any differences in the relative ionization collection in the following discussion.

As shown in Fig. 7.20, bringing the CDMS measurements of the ionization yield in Ge into agreement with previous measurements would require the recoil energy to have been overestimated at energies below $\sim$20 keV, and underestimated at higher energies. For the Si detectors, the measurements of the yield agree with the Lindhard prediction within uncertainties below $\sim$20 keV, but are lower than expected at higher energies. This may be related to suspected ionization collection inefficiencies in Si at low bias, as indicated in Fig. 7.16a, if they have an energy dependence.

The rescalings shown in the inset of Fig. 7.20 were determined by comparing CDMS measurements of the ionization yield to previous measurements, where the energy of the recoiling nucleus is fixed by kinematics or known features in the recoil energy spectrum. In contrast, the recoil energy estimate in CDMS is determined from the phonon signal

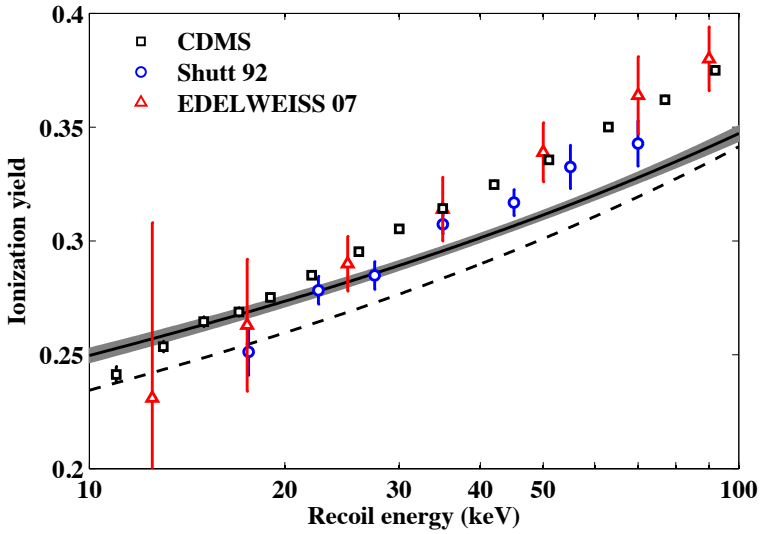

Figure 7.21: Comparison of CDMS yield measurements in Ge to previous measurements of the ratio of ionization to phonon energy for nuclear recoils in calorimetric detectors (65; 79). The dotted line shows the predicted yields from Lindhard *et al.*, while the solid line and gray band show the best fit to previous measurements with known recoil energy.

assuming that there is no difference in the relative collection efficiency for phonons produced for nuclear recoils and electron recoils. If the phonon collection or energy reconstruction depends on recoil type, this could lead to the discrepancy between the ionization yields measured in CDMS and previous experiments. Figure 7.21 compares the yields measured in the CDMS Ge detectors to previous measurements of the ratio of ionization to phonon energy for nuclear recoils in calorimetric detectors. While there are significant differences in the mechanism of phonon collection used by the calorimetric and CDMS II detectors, both are based on measurements of the ratio of the ionization to phonon signal using nuclear recoils with a broad energy spectrum. Differences in the relative phonon signal for electron recoils and nuclear recoils should be common to both measurements. As shown in Fig. 7.21, these phonon-based measurements agree with the CDMS II measurements within statistical errors, but are higher than previous measurements with known recoil energies above $\sim$20 keV.

The extent to which these energy rescalings may affect upper limits on spin-independent WIMP-nucleon cross section vs WIMP mass in Ge detectors is presented in Chapter 9.

Chapter 8

Monte Carlo-based energy scale recalibration

As the primary analysis variable, an event's measured recoil energy is of central importance at nearly every step of an analysis and its interpretation. Energy calibration of the ionization and phonon signals in CDMS II detectors, which are together used to estimate an event's recoil energy, was discussed in Chapter 7.

For an ideal detector this estimate would be very close to the true recoil energy, and it would work equally well for electron recoils and nuclear recoils. Real ionization and phonon detectors are vulnerable to a number of non-idealities (such as the collection inefficiencies discussed in Sec.7.2.2), which introduce systematic uncertainties that are difficult to quantitatively predict. Analytical techniques can set constraints on the magnitudes of these uncertainties and determine the extent to which they may bias our results. One technique to constrain the uncertainty on the energy scale for nuclear recoils compares measurements of their ionization yield in CDMS II detectors to semi-empirical yield models and previous measurements by other experiments. This method was presented in Sec. 7.4.

An alternative technique compares the shapes of the observed recoil energy spectra from neutron calibration data to simulations or numerical calculations. Spectral confirmation of the energy calibration for electron recoils is generally straightforward due to the availability

of a variety of spectral lines from radioactive γ sources at a wide range of energies. No such lines are available in the energy spectrum of nuclear recoils from the ^{252}Cf calibration source, and so the comparison is more difficult. The nuclear recoil energy spectrum decreases quasi-exponentially and is nearly featureless, particularly in the Ge detectors.

In this chapter I present such a spectral comparison with a Monte Carlo simulation in an attempt to directly verify the constructed energy scales for nuclear recoils in CDMS II detectors, and constrain their systematic uncertainty. The extremely smooth spectrum in Ge detectors limits this method's power, but stronger constraints are possible for the Si detectors. A broad resonance in the elastic scattering cross section for ^{28}Si results in a visible feature at $\sim$20 keV in the Si recoil spectra. The origins of this feature are detailed in Sec. 8.6.

Generally, knowledge of the nuclear recoil energy scale to within $\sim$10% is sufficient to prevent significant bias when interpreting results as constraints or allowed regions in the plane of WIMP-nucleon cross section vs WIMP mass for masses greater than a few tens of GeV/c^2. However, at the lowest masses to which the CDMS II detectors may be sensitive, a more accurate determination of the energy scale becomes important for robust comparison of results from different experiments. This is particularly important in light of recent interpretations of data from several experiments as possible evidence for a light ($<$10 GeV) WIMP (80; 81; 34; 82).

8.1 The Simulation

The simulated data were generated by a Geant4 Monte Carlo containing the full experimental apparatus in the five-tower configuration used for CDMS II. The code was run in parallel on hundreds of cores continuously over several months, thanks to resources provided by the UNIX Compute Farm at SLAC.

Geometry

The configuration of icebox, hardware, and shielding is centered around the 30 Si and Ge ZIP detectors, and is designed to closely match the arrangement presented in Sec. 4.2. Depicted in wireframe in Fig. 8.1, it contains, in order of increasing radius:

- High-purity copper defining the structure of each tower, each housing six detectors and consisting of, from top to bottom:
  - 2.0 kg, 8.66 mm thick, 10.62 cm long "upper tower"
  - 0.233 kg, 4.85 mm thick lower cap to the upper tower
  - 0.140 kg, 1.02 mm thick connector tube running from the upper tower down to the main detector housing
  - 0.051 kg, 6.22 mm thick ring at base of the connector tube

  and finally the detector housing itself, which consists of
  - 0.384 kg, 2.15 mm thick, 7.27 cm long side housing
  - 0.071 kg, 1.32 mm thick upper cap
  - 0.078 kg, 1.52 mm thick lower cap.
- Copper side coax assembly, less than 1 mm thick, connects each detector to the base temperature stage of its tower
- 0.381 mm thick "mu-metal" (a nickel-iron alloy) shielding can, with 0.19 mm thick lids
- 10 cm thick "inner" layer of polyethylene shielding, with circular holes removed for the stems connect the icebox to the external electronics and dilution refrigerator
  - Electronics pass through the "E-stem," represented here as a copper tube of radius 6.35 cm; the real stem is 1 cm thick, so the inner 5.35 cm volume is filled with vacuum

  - The icebox is couple to the refrigerator through the "C-stem" tube, represented here as a 1.75 cm thick cylinder of copper, with outer radius 4.29 cm; the hollow inner volume is again represented with a solid vacuum layer with a radius of 2.54 cm.

- 4.4 cm thick layer of "ancient" lead shielding with extremely low ^{210}Pb content
- 17.8 cm thick layer of standard low-activity lead shielding
- 39.4 cm thick cylindrical shell "outer" shell of polyethylene shielding; the circular holes for the stems extend through this layer as well as the lead layers
- Muon veto panels, composed of $C_{10}H_{11}$ scintillator material. Each is represented as a large flat box 2.54 cm in thickness. The complex multi-tiered array of side panels is more simply represented as five larger panels. This simplification has no impact on any study not directly associated with the veto itself; in particular, the ^{252}Cf calibration sources bypass this layer entirely and it has no impact on the neutron flux at the detectors.

As in the real towers, there is no material in the space between one detector's lower face and the upper face of the detector positioned 3.5 mm below it.

Approximately 10 billion primary decay events were simulated, distributed evenly across the three source positions (detailed below). This was determined to be a sufficient number to satisfy two requirements:

- The resonance feature at $\sim$20 keV, discussed in more detail in Sec. 8.6, should be clearly visible and resolved as well as possible.
- Bin errors added in quadrature across measured and simulated spectra should be no more than 5% larger than the error in the measured bin alone. In fact, using all the generated Monte Carlo data would result in a $\ll$1% increase in relative error, but generally a much smaller random subset was chosen to speed up computation when scanning over finely-binned multi-dimensional parameter space.

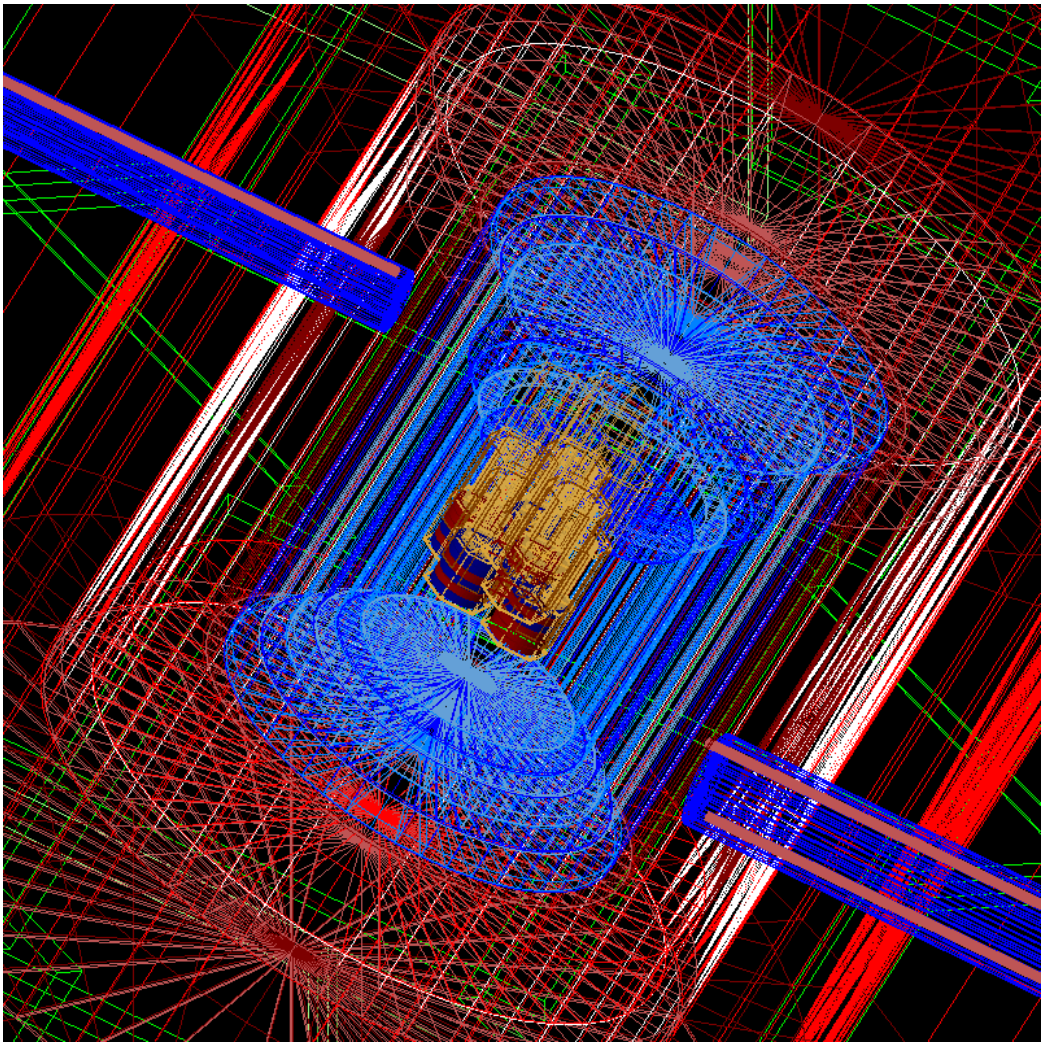

Figure 8.1: Wireframe rendering of the complete detector, hardware, and shielding geometry used in the high-statistics Geant4 Monte Carlo simulation of ^{252}Cf neutron calibration during 5-tower CDMS II running. The view is angled to simulate perspective and to emphasize the "E-stem" (left) and "C-stem" (right), connecting the icebox to the readout electronics, and to the dilution refrigerator, respectively.

Label	x (cm)	y (cm)	z (cm)
SW	55.24	-7.60	19.87
NW	-55.24	-9.60	-21.20
NE	-55.24	9.60	-21.20

Table 8.1: Coordinates for all three nominal ^{252}Cf source positions, as used in the Geant4 Monte Carlo. The origin of this coordinate system is the center of the icebox. All three positions were used throughout 5-tower data-taking. They correspond to an operator retraction of 8 inches from the maximum insertion point (where the tube comes into contact with the copper cans).

This configuration was exposed to a ^{252}Cf source placed at three separate locations corresponding to the recorded source positions along the tubes into which these sources were inserted during neutron calibration data acquisition. The operational procedure was to insert the sources into the source tubes until they contacted the copper cans, and then to measure a retraction of 8 inches. In a coordinate system with the center of the icebox at the origin and each tower's center at a vertical offset of $z = +3.28\,\mathrm{cm}$), the nominal ^{252}Cf source positions are given by the coordinates in Table 8.1, using the convention that $+\hat{x}$ points southward, $+\hat{y}$ points eastward, and $+\hat{z}$ points upward.

These source positions bypass most of the shielding with high neutron stopping power.A standard ^{252}Cf input spectrum was used to generate incident energies for neutrons, and this spectrum was degraded in energy by propagation through the shielding. Features in the input spectrum are washed out to the extent that an independent simulation with an input spectrum of the Maxwellian form $dn/dE = \sqrt{E} \cdot \exp(-E/1.42\,\mathrm{MeV})$ produced identical results to within uncertainties. It can thus be inferred that the shape of the spectrum of recoil energies for this configuration is largely independent of details of the input neutron energy spectrum.

Each event's recoil energy in a detector was determined by directly summing its energy depositions into that detector's crystal lattice via the recoiling nuclei. These energies were then used to fill a histogram with bins chosen to give comparably sized error bars throughout the energy range of interest.

8.2 Dataset selection

The recoil energy spectra for Si and Ge have distinct shapes, and they were analyzed separately in previous publications (42; 72; 80). Of the two, the distinctive shape of the Si spectrum allows for more conclusive comparisons than does the extremely smooth Ge spectrum.

The CDMS II Ge detectors have been used for both low and high-thresold WIMP-search analyses over a period from October 2006 to September 2008, comprising Runs 123 to 128. During this period twenty-nine ^{252}Cf calibration datasets were acquired. The discussion in this chapter will refer to these data sets and the corresponding analyses as the "Ge low-threshold analysis" (72) and the "Ge high-threshold analysis" (83; 42).

The primary WIMP search using the CDMS II Si detectors was a blind analysis of data taken from July 2007 to September 2008, during Runs 125 to 128 (80). There were sixteen ^{252}Cf calibration datasets acquired during these runs. The discussion in this chapter will simply refer to this as the "Si analysis."

8.2.1 Normalization and relative exposure

The above data sets were pruned to include only those series during which there was no known problem with detector operation or data acquisition. Data quality cuts were applied at this early stage, rejecting events and time periods displaying known pathologies, including electronics glitches, anomalously shapen charge pulses, and period of high baseline noise. These data were then subject to many standard WIMP-search analysis or modified selection cuts on an event-by-event basis, as detailed in Sec. 8.3.

The observed neutron event rates in the remaining data sets were examined in more detail to ensure they were suitable for further study. With the standard operational procedures undertaken for neutron calibration runs during CDMS II, variations in the exact ^{252}Cf source placement by the on-site operator on the order of ± 1 cm are quite plausible. This level of variation has been shown by simulation to contribute to variations in the overall neutron count rate in the detectors at the order of 20%, as in Fig. 8.2. These unknown

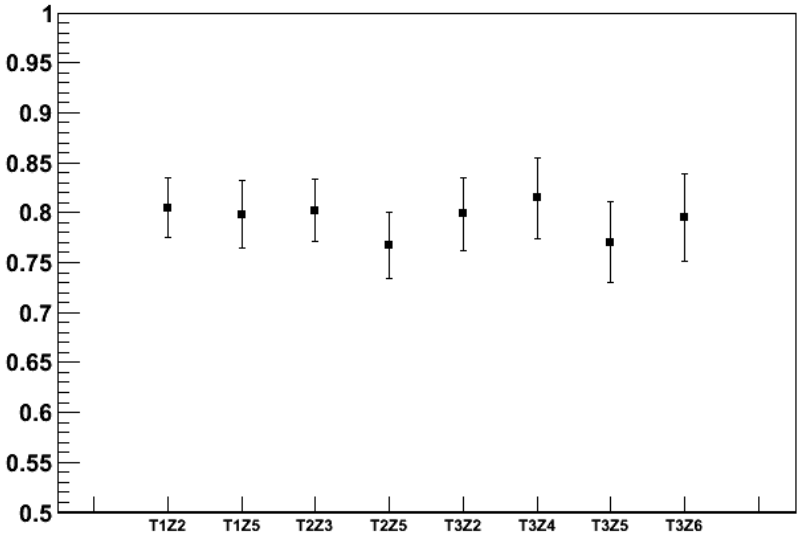

Figure 8.2: Ratio of neutron counts in several Ge detectors with source positioned ± 1 cm from nominal. This introduces effects on the overall spectral normalization each contributing at the 20% level that are difficult to predict.

normalization variations are in general difficult to quantify.

Any attempt to quantify the actual neutron flux to which each detector was exposed is complicated by the additional effect that each detector has a unique distance from each noninal source position. These detector-to-detector variations are shown for each source position in Fig. 8.3. Moreover, many of the defined "bad" data periods were restricted to a subset of the detectors.

This unequal weighting is not present in the simulated data. To account for this, we quantify the effective neutron flux at each detector during periods of good neutron calibration data acquisition, for any of the source positions. Each detector's neutron count rate was tracked vs the total neutron count rate for each series. Each source position was analyzed separately, as each detector's exposure should scale at a different rate relative to the total rate based on its separation from the source. These detector-rate vs total-rate fits are shown in Figs. 8.4 and 8.5.

An analogous but simpler exposure scaling is carried out in the Monte Carlo data as

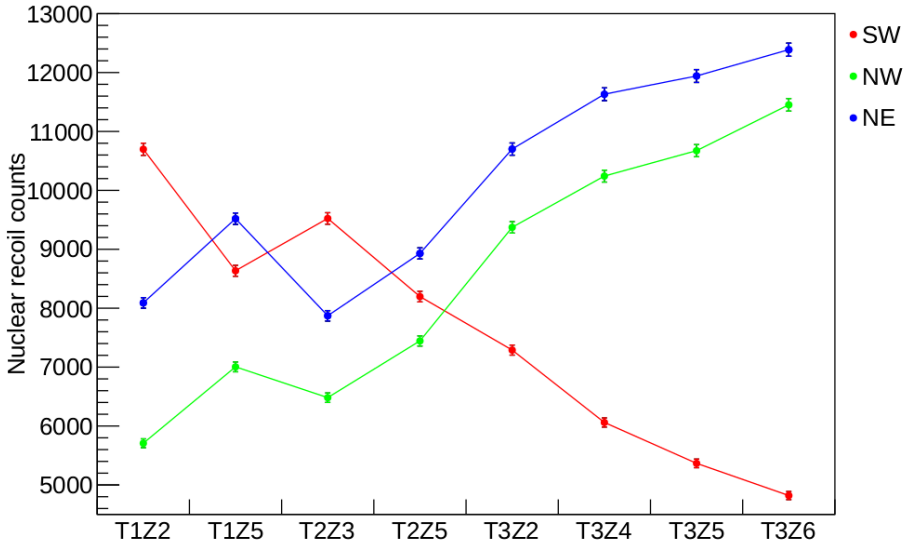

Figure 8.3: Nuclear recoil event counts in Geant4 ^{252}Cf calibration data for each detector, colored by source position. The detector-to-detector variations in exposure are strongly dependent on the position of the source, by approximately a factor of 2.

well. Variations in the number of Monte Carlo primaries from each source position are factored out, so that the fractional volume of Monte Carlo data from each source position corresponds to the exposure fraction in the measured data at that position.

8.3 Analysis cuts

Events in the selected calibration datasets are subject to further cuts on event-specific parameters to ensure a sample that includes only true nuclear recoil events with signals that appear to have been measured reliably by the detectors. These cuts are very similar to those called for in the corresponding WIMP-search analyses.

Energy range

The analysis energy range for each branch of this study was chosen to match the corresponding WIMP-search analysis. All of these analyses use a maximum recoil energy of

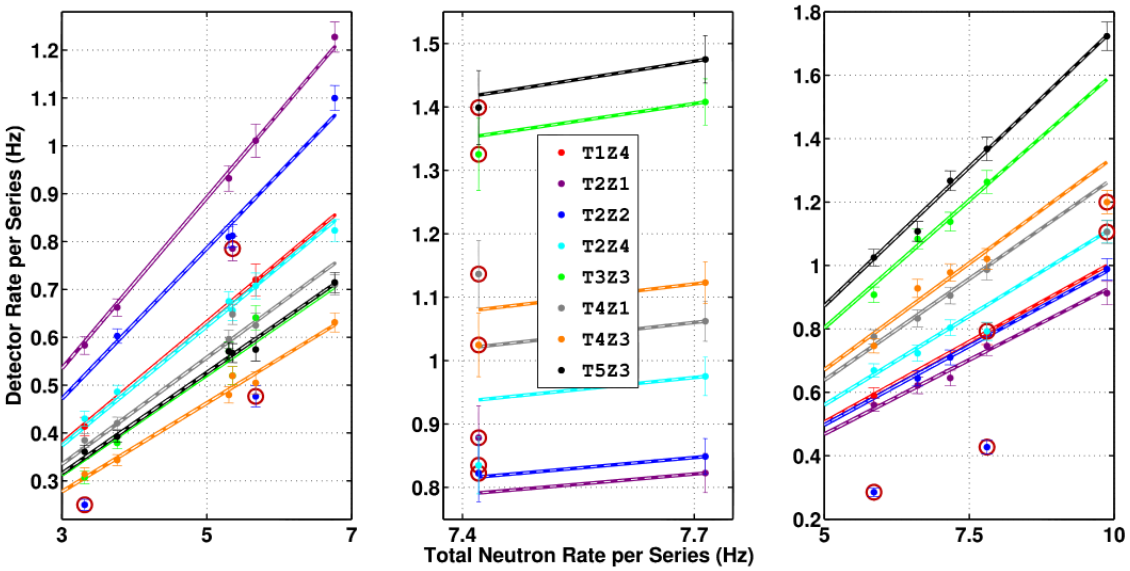

Figure 8.4: (left) Neutron calibration data series taken with ^{252}Cf source placed at the SW position; (center) series with source at the NW position; (right) series with source at the NE position. Individual detector nuclear recoil rates for each series are plotted vs the total nuclear recoil rate in all Si detectors for that series. Circled detector-series combinations with anomalously low or high neutron rates were excluded from further analysis, such as the two low-rate series in T2Z2 at the NE source position.

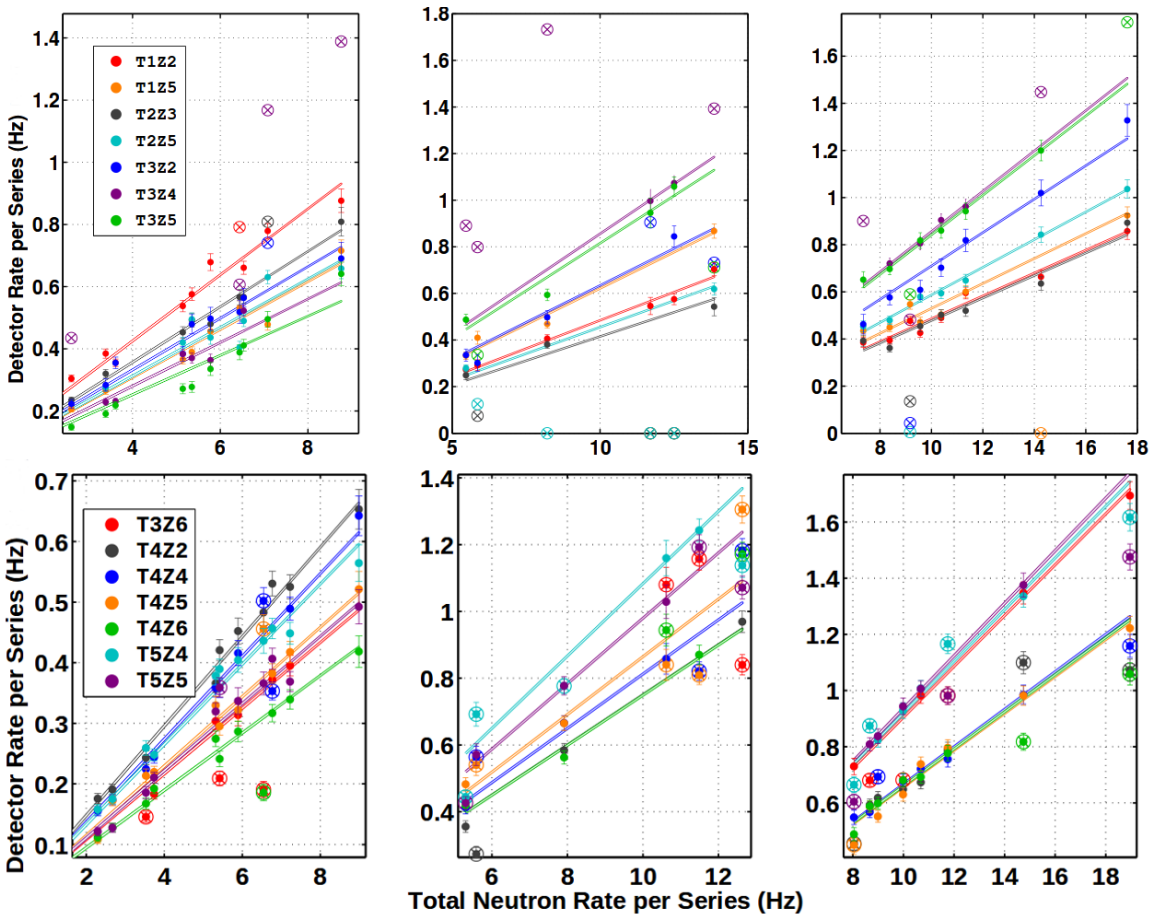

Figure 8.5: Nuclear recoil event rates per detector vs the total rate in all detectors, with each vertical alignment of points representing a different series of ^{252}Cf calibration data. Linear fits across series are shown for each detector. **Top row**: Ge detectors from towers 1-3. **Bottom row**: Ge detectors from towers 4-5. **Left column**: series with the source placed at the SW position; **Center column**: series with source at the NW position; **Right column**: series with source at the NE position. Those series-detector combinations represented by a cross marker were excluded from further analysis for having anomalously low or high neutron rates.

100 keV. For the Si analysis (80), the recoil energy of each event was restricted to lie above a detector and dataset-dependent threshold ranging from 7 keV to 15 keV, chosen blindly based on calibration data. For the Ge high-threshold analysis, the traditional analysis range of 10 keV to 100 keV was used. For the Ge low-threshold analysis, this study focuses on the 2 keV to 30 keV range, corresponding to the most sensitive region analyzed in (72).

Fiducial volume cut

The first selection cut passes only those calibration events occuring within a detector's fiducial volume by requiring that the signal in the outer ionization electrode be consistent with noise. This "q-inner cut" is highly energy-dependent. On the low energy side, it begins to fail when recoil energies become low enough that even events with charge fully collected in the outer electrode produce a signal consistent with noise and are thus accepted. Its acceptance is also slightly reduced at higher energies where increased charge production leads to a larger fraction of charge carriers being absorbed by the outer electrode. The cut is defined independently on each of the three data analyses. A typical construction of this cut for a Ge high-threshold detector is shown in Fig. 8.6.

Charge threshold cut

The charge threshold cut is designed to reject events with sufficiently small ionization signals that they are consistent with noise. For these events ionization yield is unreliable and the charge signal is not useful in discriminating against background events.

The cut is set using randomly-triggered events, representing a noise sample. Events passing the cut were required to have an ionization signal in the inner charge electrode above a detector and dataset-dependent threshold set at 4.5σ above the noise mean. This cut is shown in two-dimensional "outer vs inner" space in Fig. 8.7, and projected along the inner charge axis used to set the cut in Fig. 8.8.

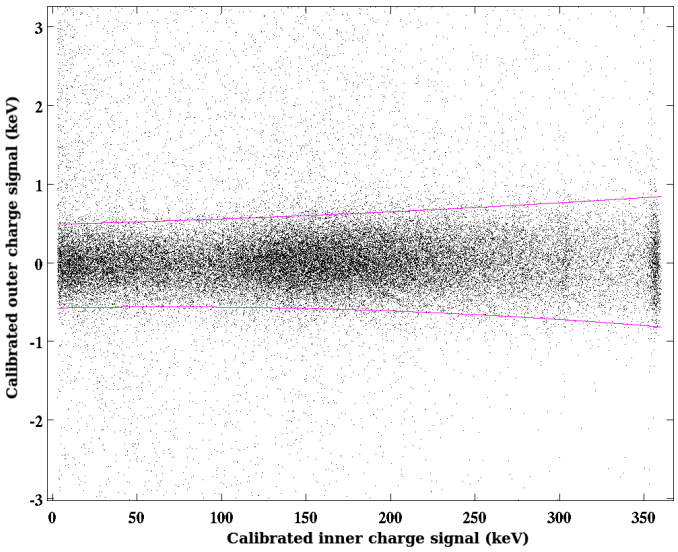

Figure 8.6: Fiducial volume cut from the Ge high-threshold analysis, shown for a typical Ge detector, T1Z2. Magenta curves represent the $\pm 2\sigma$ width of the fitted gaussian about zero in outer charge energy. Events outside these curves are considered inconsistent with a noise signal in the outer channel, and are thus rejected.

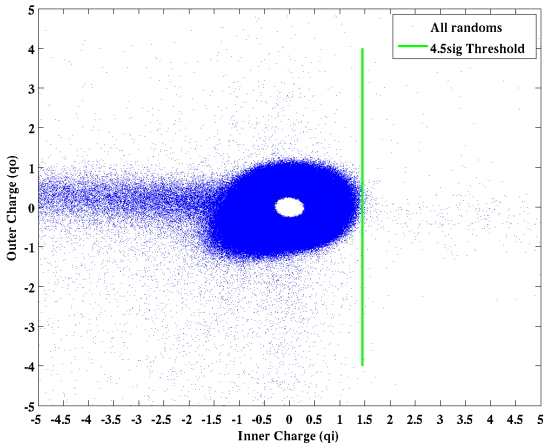

Figure 8.7: The ionization "noise ring" at zero energy. The optimal filter algorithm is biased away from zero as it will always attempt to reconstruct an energy from a noise trace.

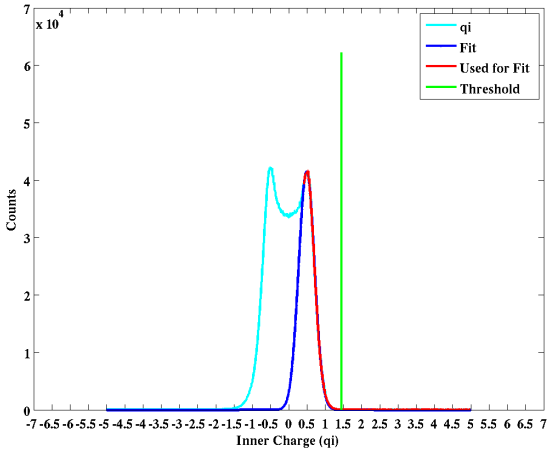

Figure 8.8: The charge threshold cut placed at 4.5σ above the mean of a fit of a Gaussian to the near-Gaussian portion of the positive peak in the ionization noise ring.

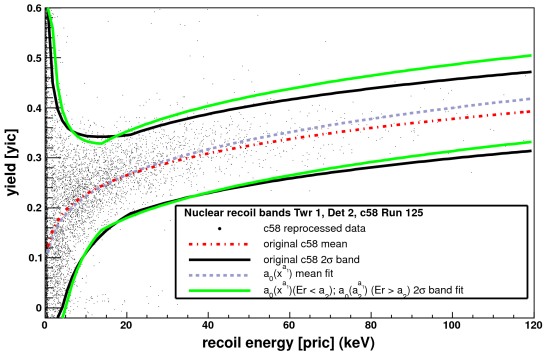

Figure 8.9: The $\pm 2\sigma$ nuclear recoil yield band cut; defined as a smooth polynomial for the original Ge high-threshold analysis, and with a piecewise definition for the Ge high-threshold re-analysis (in preparation).

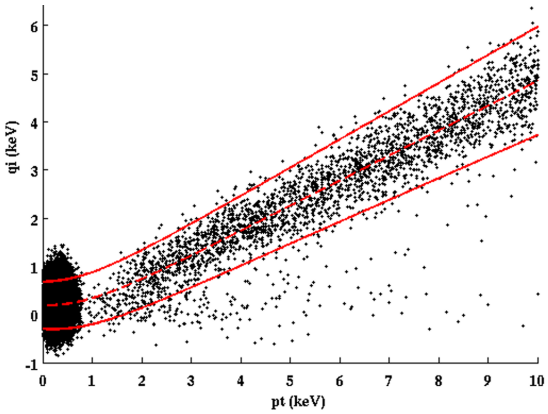

Figure 8.10: The nuclear recoil band cut for a typical Ge low-threshold detector (T1Z5), defined directly in charge (`qi`) vs total phonon (`pt`) energy, to avoid band flaring at low energy.

Nuclear recoil yield band

To select nuclear recoils, events were required to lie within $\pm 2\sigma$ of the mean nuclear recoil yield. For the Si and Ge high-threshold analyses, the distribution is binned in Luke-corrected recoil energy and fit to a Gaussian in yield within each energy band. The μ and σ parameters from these fits are used as inputs to further polynomial fits to the mean and width of the nuclear recoil band as a function of energy, shown in Fig. 8.9.

For the Ge low-threshold analysis, the width of a band defined in yield flares out severely at low energies where the ionization signal becomes comparable to its noise resolution. Thus the fits are made in the plane of `qi` vs. `pt` instead, where `qi` is the calibrated ionization energy from the inner charge electrode and `pt` is the calibrated total phonon energy. Similar binned fits to the mean and width of the distribution are performed, producing a `qi` vs `pt` nuclear recoil band as in Fig. 8.10.

The distribution of events about the mean of these bands is not exactly Gaussian, but a $\pm 2\sigma$ band cut has consistently been measured to be 95% efficient throughout the energy range.

8.4 Efficiency functions

The selection cuts discussed in the previous section introduce a bias in the measured data that is not reflected in the simulated data. One method to compensate for this this is to simulate the effect of these cuts on the Monte Carlo results.

A more practical method brings to bear the many techniques that have already been developed by the CDMS analysis team to study each cut's acceptance efficiency for nuclear recoils as a function of recoil energy. These efficiencies are typically measured in several energy bins and parametrized as "efficiency functions." In order to directly compare the measured data to simulation, the efficiency function for each cut must be calculated, evaluated at each bin of the recoil spectrum, and used to normalize on a bin-by-bin basis. Each function has an associated systematic uncertainty that must be estimated and propagated to the final spectrum. The resulting total uncertainty in each bin is a factor in the χ^2 calculation which evaluates the goodness of fit between the measured and simulated spectra (Sec. 8.5).

8.4.1 Energy-dependent efficiencies

Analysis cuts with energy-dependent acceptace of nuclear recoils can significantly alter the shape of the energy spectrum. Modeling the efficiency of these cuts is critical to any spectral analysis. Four such efficiencies are significant in this analysis, detailed below.

Hardware phonon trigger

Each detector is configured to issue a trigger if it registers a phonon signal above a threshold value, specified in mV. The resulting energy threshold in energy units is modeled as an error function with a width characterized by the resolution of the phonon pulse measurement. Evaluated in the energy ranges used in to the present study, it is always equal to unity, but it is necessary to include this effect when examining the shape of the spectrum below the analysis threshold. By definition, this efficiency applies only to single-scatter events, as

any given detector's signal in a multiple-scatter event will be recorded with 100% efficiency, regardless of the energy ultimately reconstructed for that detector.

The trigger efficiency for single-scatter events is a measure of the probability that a test detector will issue a trigger when a given recoil energy is deposited in that detector. Events with phonon signals below that detector's trigger threshold are only recorded when some other detector triggered. In broad terms, a test detector's trigger efficiency in a given energy bin is thus calculated as the fraction of events for which the test detector has a reconstructed energy in that bin and also issues a trigger.

This calculation is less straightforward for ^{252}Cf calibration data than for low-background WIMP-search data. During calibration, the overall scattering rate in the detectors is highly elevated, so additional care must be taken to deal with "pileup" events, in which unrelated scatters in separate detectors may appear in the same trace window. The modified procedure involves the following steps:

- The trigger buffer records at most five trigger times after the global trigger. The optimal filter search window is within [-50, 200] µs of the global trigger, so only events for which the trigger buffer extends at least 200 µs after the global trigger are considered. This ensures that no potential triggers within the optimal filter search window could have been gone unrecorded.

- If the test detector issued the global trigger, events are not considered unless at least one other detector triggered within [-200, 50] µs of the global trigger. This ensures the test detector's trigger would have been part of either the positive or negative portion of the search window of another event, and would thus have been recorded anyway.

- If the global trigger was issued by a different detector, the test detector must also trigger within the standard [-50, 200] µs search window from the global trigger.

- Reject events with a trigger in the test detector in the windows of [-500, -51] µs or [201, 400] µs from the global trigger. Triggers in these windows were seen almost exclusively in pileup events.

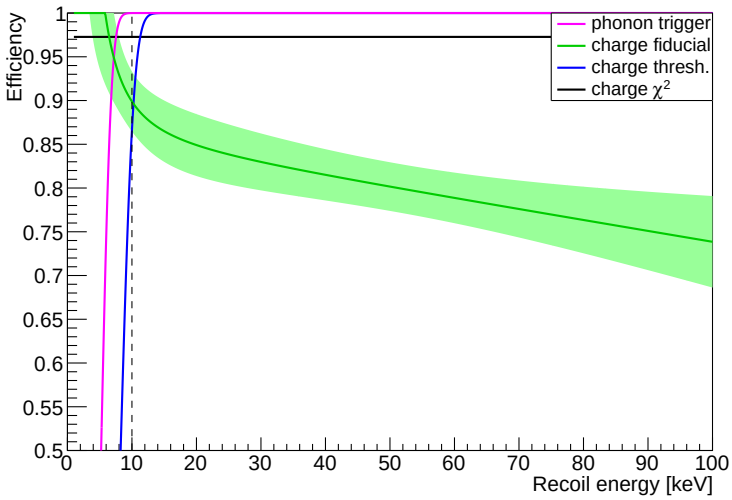

Figure 8.11: General form of the four significant energy-dependent efficiency functions, shown for detector T1Z4 during Run 125. The phonon trigger efficiency (magenta) is unity above the analysis threshold (dashed vertical line at 10 keV). The charge threshold is the biggest contributor to the position of the analysis threshold, and its efficiency (blue) generally falls below unity at energies near this value and lower. The charge χ^2 efficiency (black) was found to have negligible energy dependence. The charge fiducial volume cut efficiency (green) is shown with shaded 1σ error band.

The efficiency is calculated by dividing the remaining number of events in an energy bin for which the test detector triggered by the total number of events in that energy bin. The subdominant nature of this efficiency for this analysis can be seen in its magenta curve in Fig. 8.11.

Charge threshold cut

The charge threshold cut efficiency is the primary determinant of the overall analysis threshold for the Si and Ge high-threshold analyses. It is calculated analytically at each energy by finding the integrated fraction of the probability distribution that fits within the bounds of the 2σ nuclear recoil band, excluding the portion falling within 4.5σ of the mean of the charge noise Gaussian. Due to their conceptual similarity, this efficiency is combined with that of the cut requiring nuclear recoil events to have yield at least 3σ below the mean of

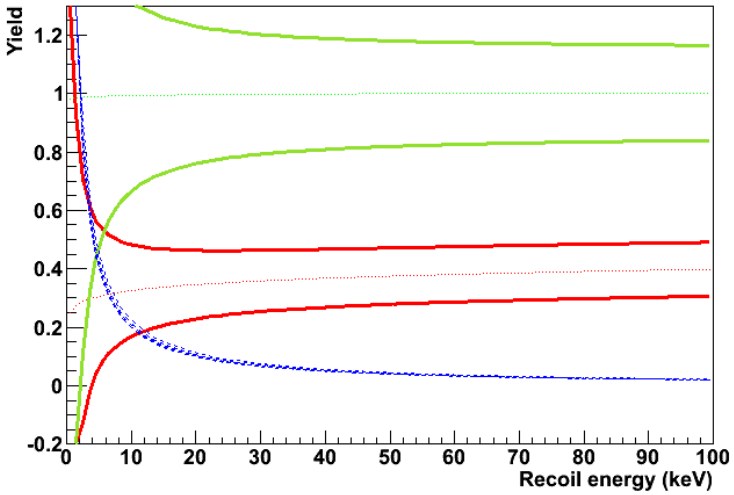

Figure 8.12: The electron and nuclear recoil bands overlap at low energies, shown here for the Ge detector T2Z1. Any region falling within the green (solid, light) $\pm 3\sigma$ electron recoil band or below the blue (dashed) 4.5σ charge threshold cutoff is removed from the signal region defined by the red (solid, dark) 2σ nuclear recoil band. This subtraction analytically defines the combined inefficiency of the charge threshold and "below-ER-band" cuts.

the electron recoil band. The region defined by these three conditions is shown in Fig. 8.12.

The combined efficiency of these two cuts is calculated analytically on a finely-spaced grid across the analysis energy range. A simple 1-dimensional linear interpolation function gives a much better fit to the shape of this efficiency curve than would an error function; the two forms are compared in Fig. 8.13.

Ionization χ^2 cut

An additional cut efficiency that may have significant energy dependence is the ionization pulse χ^2 cut. This cut is based on a χ^2 variable derived from a comparison between the ionization signal pulse shape and the ionization pulse optimal filter template. A parabolic cut is set as a function of energy, excluding events with ionization χ^2 values greater than 3σ above the mean. No significant energy-dependence is observed for this cut, so a simple mean value for the efficiency serves over the analysis energy range.

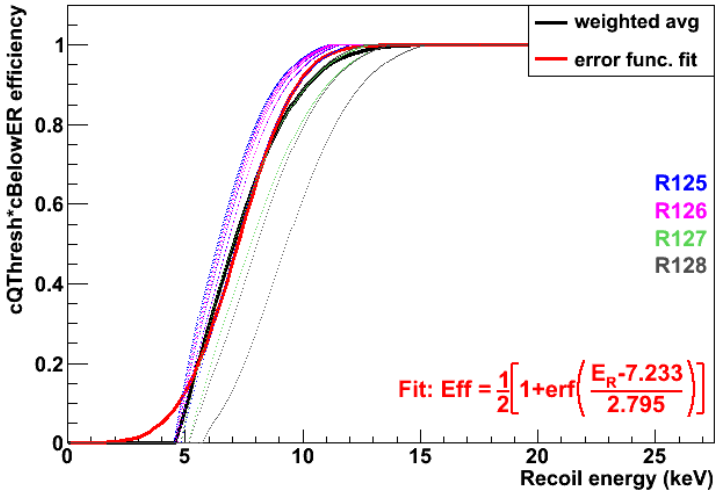

Figure 8.13: The efficiency of the charge threshold and "below-ER-band" cuts (labeled `cQThresh_c58` and `cBelowER_c58` in the Ge high-threshold analysis), as calculated analytically from the yield band overlaps as depicted in Fig. 8.12. An error function fit is shown in red, but is not used, as it is in poor correspondence with the shape of the overlap region at the edges. Instead the efficiency is calculated at a series of finely spaced energies and a linear interpolation function is fit, shown in black.

Fiducial volume cut

Finally, the ionization-based fiducial volume cut efficiency represents a significant overall efficiency drop and exhibits strong energy dependence. Gamma leakage into the nuclear recoil band at low energy compromises the accuracy of a simple estimate of the fraction of events in the nuclear recoil band that pass the fiducial volume cut. The efficiency calculation is thus adjusted by subtracting an estimate of the number of passing electron recoils leaking into the nuclear recoil band from both numerator and denominator. This estimate is made by examining the number of events in extended-band and between-band regions in both ^{133}Ba and ^{252}Cf calibration data, and assuming a Gaussian distribution of events populating each band.

The resulting spectra give the raw nuclear recoil rate in units of counts per keV per kg-day, and are directly comparable to the spectra as generated by the simulation. A mosaic of the efficiency-corrected nuclear recoil spectra for all eight detectors in the Si analysis

is shown in Fig. 8.14. For the Ge high-threshold analysis, Fig. 8.15 compares a typical observed spectrum to Monte Carlo, and Fig. 8.16 shows the residuals for these spectra for all Tower 1-3 Ge Detectors. For the Ge low-threshold analysis, Fig. 8.17 shows the corresponding spectra, and Fig. 8.18 shows the corresponding residuals.

8.4.2 Energy-independent efficiencies

Several other analysis cuts have efficiencies that are independent of energy, and as such have no direct effect on spectral hardness or the inferred energy scale. Their effect is only important when considering overall normalization of the recoil spectra, and so they were factored into the relative normalization calculations discussed in Sec. 8.2.1. These cuts are listed below with their internal run-generic labels and brief descriptions:

- `cPstd`: requires the pre-trigger phonon baseline standard deviation to be less than 5σ from the mean of the noise
- `cGoodPStartTime`: removes events for which the optimal filter doesn't correctly find both the charge and phonon pulses because the phonon start time is outside the search window
- $\sim$`cNegPhononPulse`: reject events for which the signal from any phonon channel is 6σ below the mean of the noise blob in that channel
- $\sim$`cPsat`: reject events with saturated phonon pulses
- `NRband`: with sufficient Gaussianity, 95% of true nuclear recoil events are accepted by the 2σ NR band cut; this is shown to be true, to within statistical uncertainties

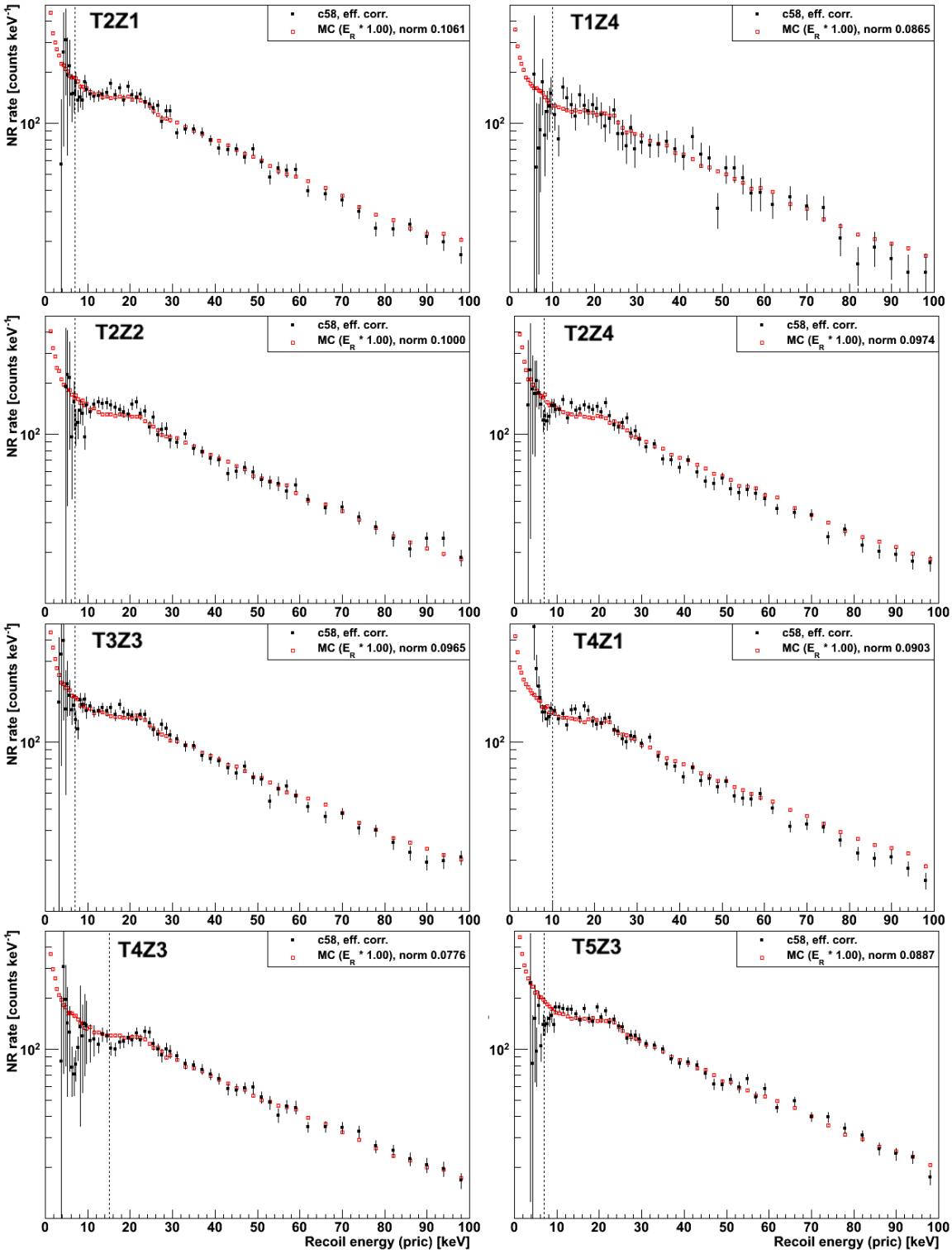

Figure 8.14: Nuclear recoil spectra in Si detectors, showing a resonance feature at $\sim 20\,\mathrm{keV}$. (solid markers) Observed energy spectra for all eight detectors used in the CDMS II Si WIMP-search (80), each bin normalized to factor out all efficiency functions evaluated at that energy. Error bars incorporate statistical and efficiency-systematic uncertainties. (red hollow markers) Monte Carlo spectrum; statistical error bars are too small to be visible.

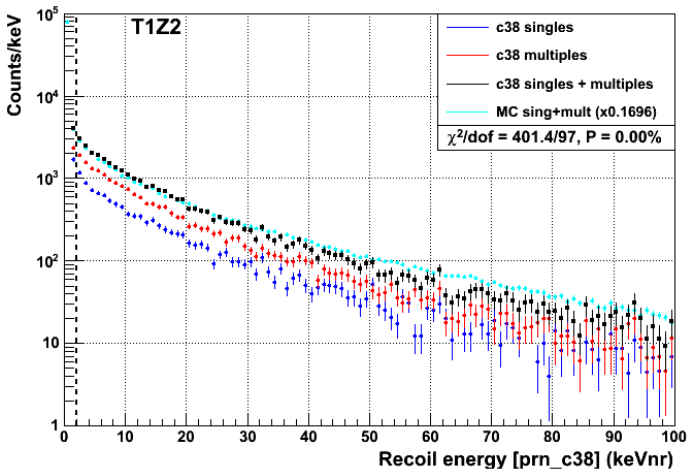

Figure 8.15: Nuclear recoil spectrum for the Ge high-threshold analysis (83; 42), shown for T1Z2. Single-scatter events (blue markers) are normalized to factor out all efficiency functions at that energy; the same is done for the multiple-scatter events (red markers), excluding the trigger efficiency. The combined calibration spectrum (black markers) is compared to the spectrum from the Monte Carlo (cyan markers).

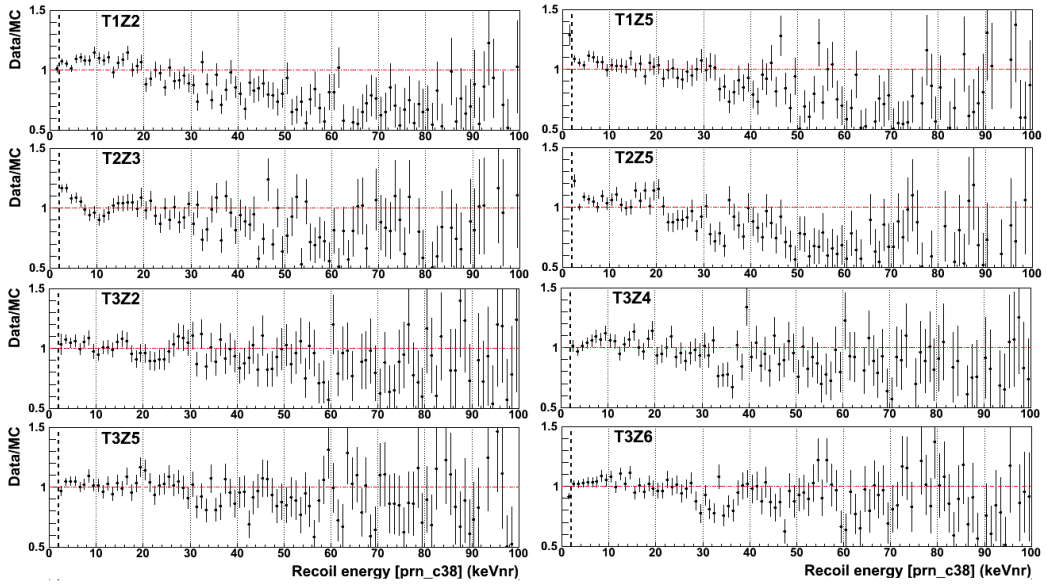

Figure 8.16: Residuals for Ge high-threshold analysis, for Tower 1-3 detectors. Markers show the ratio of observed spectrum to the Monte Carlo spectrum (black and cyan, respectively, in Fig. 8.15. These residuals highlight the growing deficit in high energy events in the calibration data compared to the simulation.

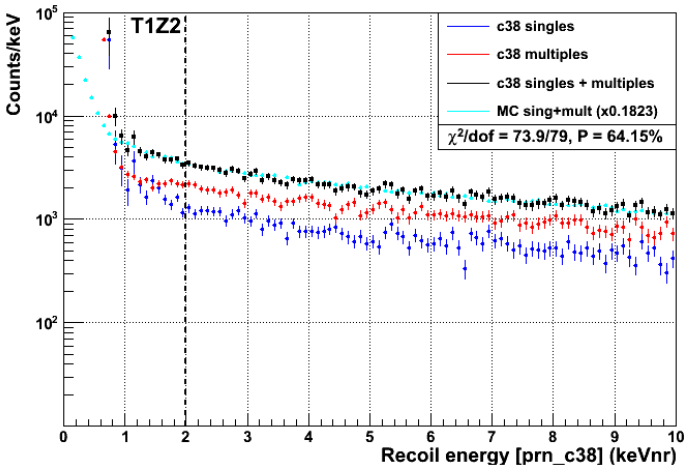

Figure 8.17: Nuclear recoil spectrum for the Ge low-threshold analysis (72), shown for the lowest energies analyzed in T1Z2. Single-scatter events (blue markers) are each normalized to factor out all efficiency functions at that energy; the same is done for the multiple-scatter events (red markers), excluding the trigger efficiency. The combined calibration spectrum (black markers) is compared to the spectrum from the Monte Carlo (cyan markers).

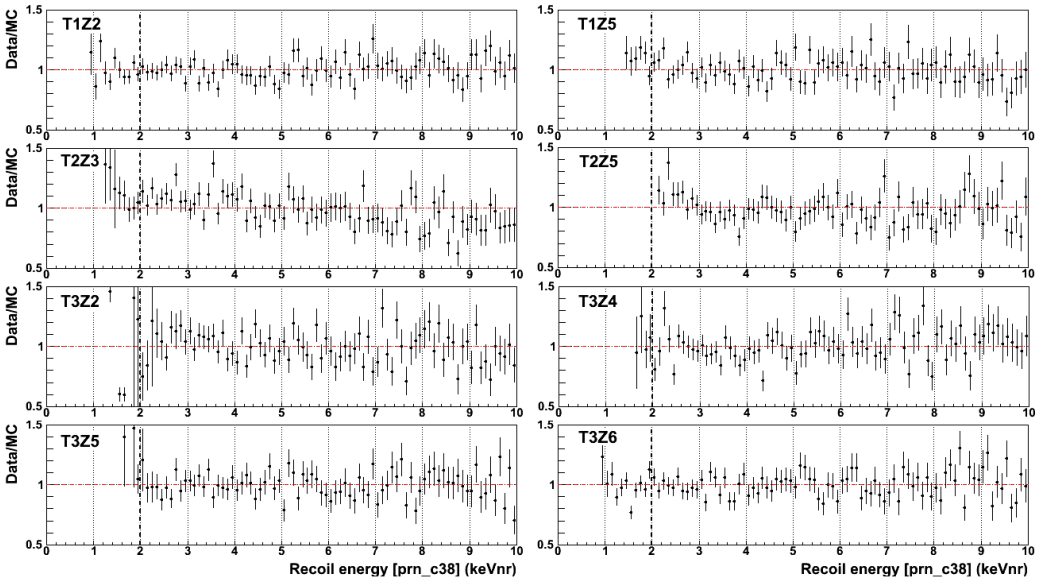

Figure 8.18: Residuals for Ge low-threshold analysis, for Tower 1-3 detectors. Markers show the ratio of observed spectrum to the Monte Carlo spectrum (black and cyan, respectively, in Fig. 8.15. These residuals highlight that the agreement between calibration data and simulation is very good at low energy, but this means very little when the normalization and spectral hardness are nearly degenerate for this nearly single-exponential spectral shape.

8.5 χ^2 minimization across energy scaling factors

Agreement between the experimental and simulated recoil spectra for each detector was then determined by scanning over a range of linear rescaling factors. These factors were applied to the recoil energy of each event in the experimental dataset prior to binning, computing a χ^2 statistic between them. The χ^2 is defined in the usual way:

$$\chi^2 = \sum_{i=1}^{k} \left(\frac{X_i - \mu_i}{\sigma_i} \right)^2 \qquad \sigma_i^2 = \sigma_{\mathrm{expt.},i}^2 + \sigma_{\mathrm{MC},i}^2 \tag{8.1}$$

The sum runs over the histogram bin index i. The energy rescaling factors correspond to potential recalibrations of the energy scale for nuclear recoils. For each adjusted experimental spectrum, normalization of the simulated spectrum was initially set by matching its integral to that of the experimental spectrum over the energy range of interest of the WIMP-search analysis. The χ^2 statistic was then calculated as a function of rescaling factor. The preferred rescaling factor was defined to be that resulting in the minimum χ^2 value.

This one-parameter minimization method was not expected to produce convincing results for the Ge detectors, since their smooth double-exponential form means the spectral hardness and overall normalization are nearly degenerate parameters. With matched-integral normalization across the 10-100 keV high-threshold analysis range, the energy rescaling factors corresponding to each detector's χ^2 minimum varied across a wide range of positive values, from 10% to 45%.

In the 2-30 keV sensitive region of the low-threshold Ge analysis (72), the spectral form is very nearly a single exponential. Any two such spectra with relative normalization fixed by matching their integrals should match very closely. It is not surprising that the χ^2 minimum is consistently found to be within 1σ of unity. The fit is severely underconstrained in this region and it provides no useful energy scale constraints.

In contrast, the visible resonance feature at ~ 20 keV in the Si recoil spectrum provides real constraining power. The scanning procedure concludes with a polynomial fit over the

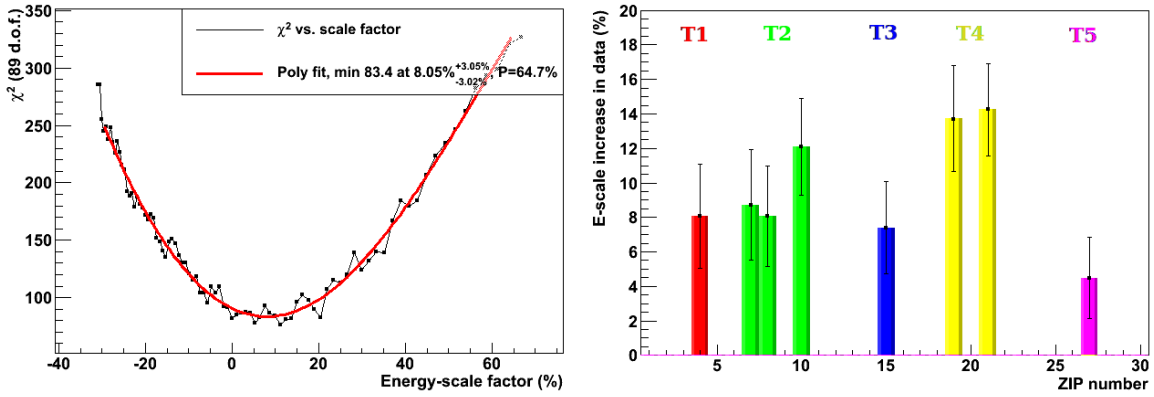

Figure 8.19: (left) Calculated χ^2 values across a range of linear energy rescaling factors for typical Si detector T1Z4. A simple polynomial fit (red curve) is used to calculate the *chi*^{2} minimum. (right) Summary of the best-fit energy rescaling factors and their 1σ ($\Delta\chi^2 = 2.3$) uncertainties for all Si detectors. These results are nearly consistent at the 1σ level with a common positive energy rescaling factor of 10%.

sampled points to find the best-fit χ^2 minimum, shown for a typical Si detector in the left panel of Fig. 8.19. The right panel of Fig. 8.19 gives the best-fit rescaling factors and their 1σ uncertainties for all Si detectors. They are nearly consistent at the 1σ level with a positive energy rescaling of $\sim$10%.

In order to explore the degenerate parameter space for Ge, and since the spectral comparison technique demonstrated believable energy scale constraints for the Si detectors, a second, more robust Monte Carlo comparison was run in a two-dimensional space of overall relative normalization vs recoil energy rescaling factor. The resulting maps of χ^2 space show a clear degeneracy in the parameters for the Ge spectra (as in Fig. 8.20), with wide regions of multiple local χ^2 minima. These maps are also useful to check for any such degeneracy for Si and to confirm the results from the one-dimensional procedure, for which relative normalization was fixed by matching integrals. The maps in Si (see Fig. 8.21) have contours aligned along the axes and show no signs of parameter correlations.

Ideally, there should be a detector-independent global χ^2 minimum for the effective neutron flux-weighted livetime normalization factors derived in Sec. 8.2.1. The only obvious remaining systematics are actual differences between the simulation geometry and the real

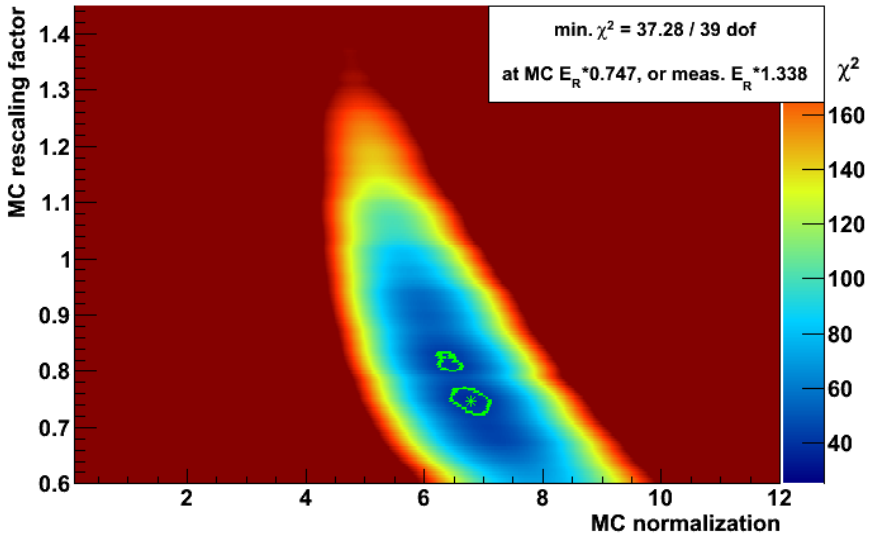

Figure 8.20: Two-dimensional histogram for typical Ge detector (T3Z4), colored by χ^2 value, sampled across a grid in the space of Monte Carlo energy rescaling factor (the inverse of the inferred rescaling in calibration data) vs overall normalization. Multiple local χ^2 minima are visible along the sloped contours, indicating significant degeneracy in the parameters. The global minimum cannot be considered robust.

apparatus. When the effective neutron flux-weighted livetimes are factored into the experimental nuclear recoil spectra from the Si analysis, the floating Monte Carlo normalizations preferred by the two-dimensional χ^2 minimization procedure agree at the 90% confidence level for data at two source positions. Somewhat worse agreement at the third position leads to the moderate horizontal spread in relative normalization of the 90% confidence regions ($\Delta\chi^2 = 4.61$) seen in Fig. 8.22, for which data from all three source positions is included.

The best-fit Monte Carlo rescaling factor at a detector's global χ^2 minimum is the inverse of the linear energy rescaling factor that would bring the experimental and simulated spectra into best alignment when applied to the calibration data. The Monte Carlo rescaling factor can thus be viewed as an effective inefficiency ϵ_P(NR) in phonon collection relative to that for electron recoils. To correct for such an inefficiency, the nuclear recoil energy spectrum in Si is shifted to slightly higher energies with a correction factor of $1/\epsilon_P$(NR).

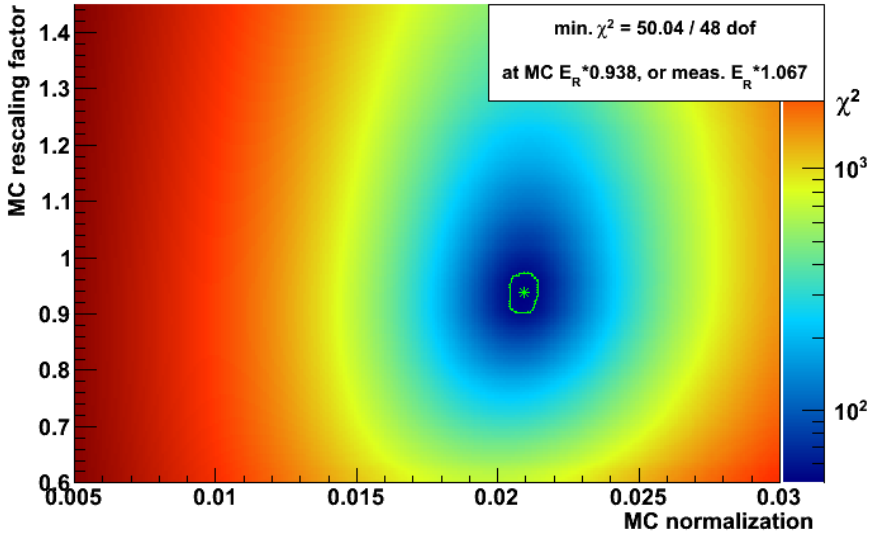

Figure 8.21: Two-dimensional histogram for typical Si detector (T2Z1), colored by χ^2 value, sampled across a grid in the space of Monte Carlo energy rescaling factor (the inverse of the inferred rescaling in calibration data) vs overall normalization. The reduced χ^2 at the global minima (green asterisk) indicate good fits, with P-values generally in the range of 0.4 to 0.6. The 90% CL ($\Delta\chi^2 = 4.61$) contour is also shown (green line).

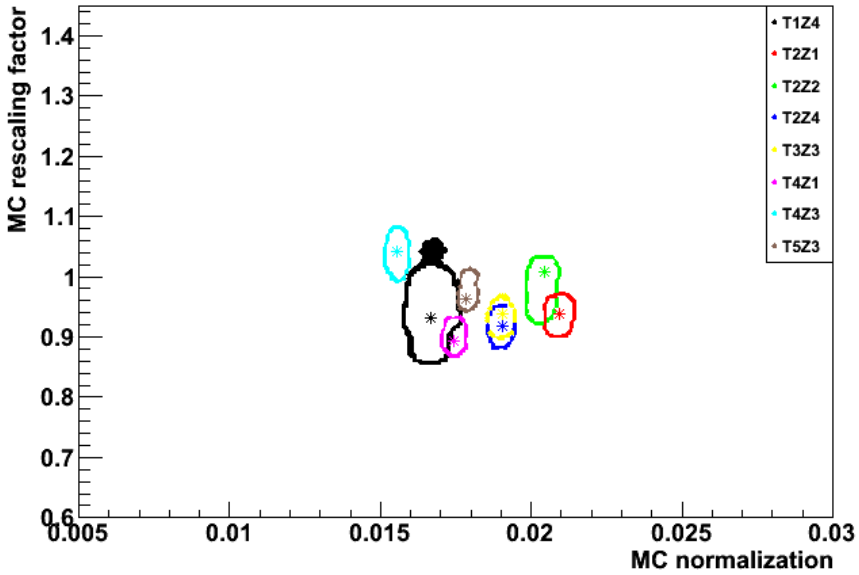

Figure 8.22: Summary of the 90% CL ($\Delta\chi^2 = 4.61$) contours (thick lines) and global χ^2 minima (asterisk) for each Si detector. These contours are calculated using calibration data from all three ^{252}Cf source positions. Two detectors, T2Z2 and T4Z3, can be considered outliers in that their χ^2 minima occur at nearly unity energy scaling.

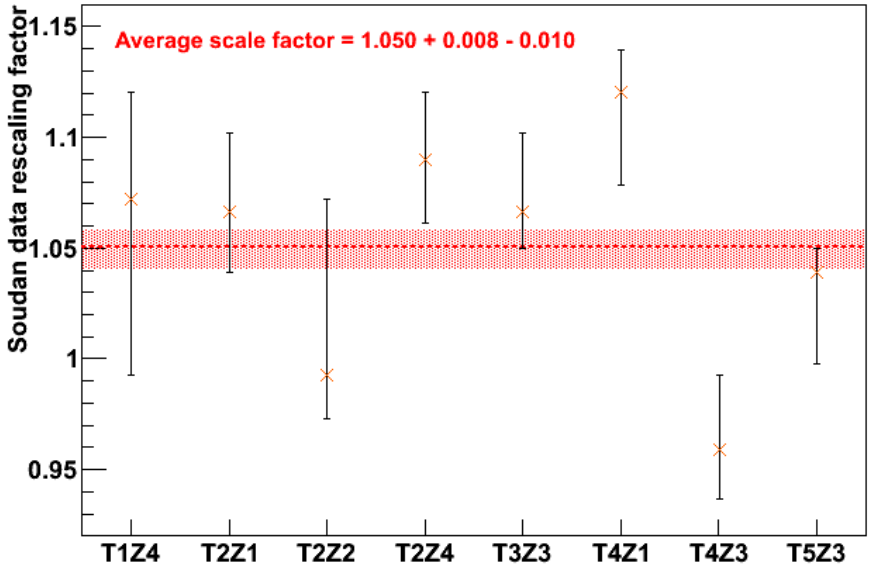

Figure 8.23: Summary of the preferred linear recoil energy rescaling factors corresponding to the global χ^2 minima for each of the eight Si detectors. The uncertainty-weighted average scale factor across all eight detectors is $1.05^{+0.008}_{-0.010}$.

A summary of the preferred energy rescaling factors corresponding to the global χ^2 minima for all 8 Si detectors is shown in Fig. 8.23. A weighted linear fit across detectors finds an average rescaling factor of $1.050^{+0.008}_{-0.010}$, corresponding to $\epsilon_P(\mathrm{NR}) = 0.953$. By removing outlier detectors T2Z2 and T4Z3 (as defined by Fig. 8.22) from the scaling process, a fit across the other detectors gives $\epsilon_P(\mathrm{NR}) = 0.905$. Both of these interpretations indicate that the true recoil energy is slightly larger than measured in most Si detectors. When computing the impact of this inefficiency on the published WIMP limits and contours, we take the conservative value of $\epsilon_P(\mathrm{NR}) = 0.9$. This is compatible with the one-dimensional minimization, which suggested a positive energy rescaling of $\sim$10%. This slightly shifts WIMP limits and contours toward higher WIMP mass, as discussed in Chapter 9.

Several physical mechanisms for a phonon collection inefficiency or other source of a mismatch between the reconstructed recoil energy and the true recoil energy for nuclear recoils were presented in Sec. 7.2.2. Any such inefficiencies specific to these detectors have not been measured directly. Since the energy calibration is fundamentally based on an

electron-equivalent scale defined by gamma calibration peaks, linear losses in the collection of either ionization or phonons from nuclear recoils would appear in the energy scale chiefly through a mis-subtraction of the Luke phonon contribution to the total phonon energy. This is because the Luke contribution is proportional to charge and varies with energy for nuclear recoils. Since there is no clear reason to believe the magnitude of these effects should be the same across the CDMS II detectors, is it not of any great concern that the preferred rescaling factors across detectors are not quite in agreement at the 1σ level. Whatever effects are present are seen clearly to be limited to the 5-10% level.

8.6 Elastic scattering resonance in ^{28}Si

The shape of the nuclear recoil energy spectrum in Si (Ge) resembles a single (double) exponential. Deviation from this form is seen most clearly in the Si spectrum from the high-statistics Geant4 Monte Carlo simulation. Around 20 keV the exponential spectrum has a bump from a resonance in the elastic scattering cross section for Si. This feature is also present in the experimental data, lending most of the constraining power to the spectral comparison to Monte Carlo data in the previous sections. The following figures and arguments are adapted from the forthcoming (78) and (84).

The differential scattering rate for nonrelativistic neutrons incident on nuclei can be written as an integral over the incident energy of the differential cross section and the differential number density,

$$\frac{dR}{dE_R} \propto \int \frac{d\sigma}{d\Omega}\frac{dn}{dE_i}\frac{dE_i}{\sqrt{E_i}}. \tag{8.2}$$

The differential number density of interest is that of the incident neutrons after propagation through the shielding separating the detectors from the ^{252}Cf sources during calibration. The spectrum of incident neutron energies was taken directly from the same Geant4 simulation and fit with four exponentials, as seen in Fig. 8.24.

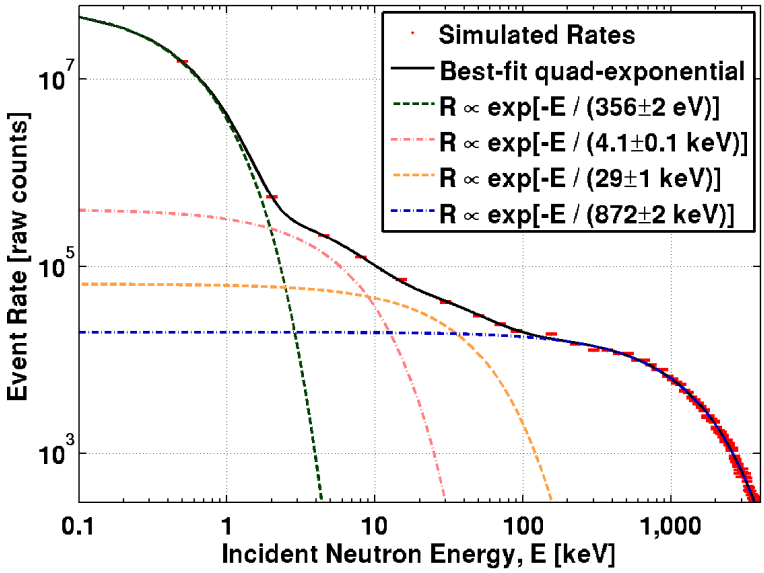

Figure 8.24: Spectrum of neutron energies incident on the ZIPs in the Geant4 simulation of ^{252}Cf calibration runs, following transport through the intervening shielding. The data are shown along with a multi-exponential fit. Figure adapted from (78; 84).

Based on this fit, the input differential number density is modeled as the following sum:

$$\frac{dn}{dE_i} \propto e^{-E_i/(356\,\mathrm{eV})} + e^{-E_i/(4.1\,\mathrm{keV})} + e^{-E_i/(29\,\mathrm{keV})} + e^{-E_i/(872\,\mathrm{keV})}. \tag{8.3}$$

The differential cross section is composed of two components,

$$\frac{d\sigma}{d\Omega} \propto \sigma(E_i) P(E_i|\cos\theta^*), \tag{8.4}$$

where $\sigma(E_i)$ is the elastic scattering cross section as a function of incident neutron energy, and $P(E_i|\cos\theta^*)$ is the angular probability as a function of incident neutron energy for a given value of the center of mass scattering angle θ^*.

The elastic scattering cross section can be obtained from the ENDF (85) and JENDL (86) databases. Geant4 uses ENDF, but the JENDL database format was found to be considerably simpler to interpet and use at low energy. In the energy range of interest for

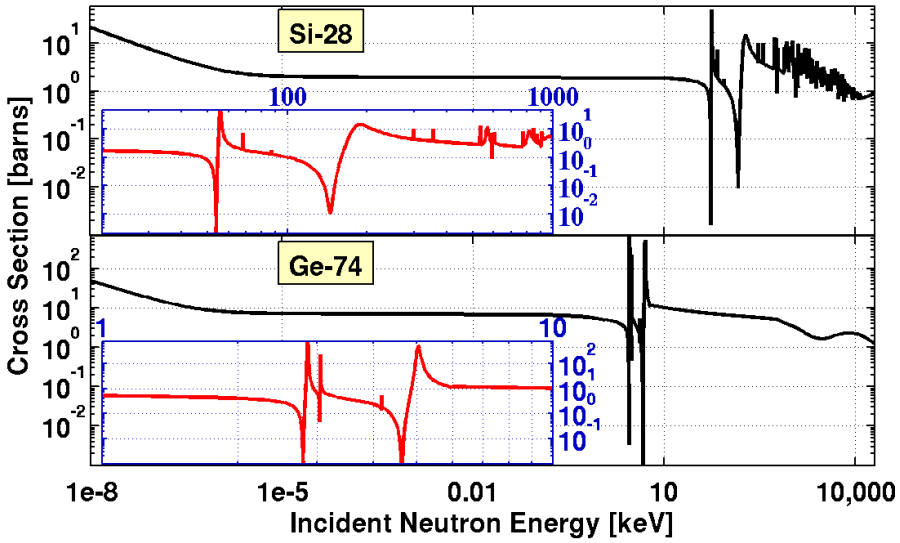

Figure 8.25: Elastic scattering cross sections for neutrons incident on Si and Ge targets. Regions of interest are shown in the zoomed insets. Values taken from the JENDL database (86). Figure adapted from (78; 84).

this study, values from both databases are effectively identical. Cross sections taken from JENDL for ^{28}Si and ^{74}Ge are shown in Fig. 8.25. Of particular interest in the Si cross section is the resonant structure observed at an incident neutron energy of approximately 200 keV, as neutrons in this energy range deposit recoil energies above the CDMS II Si analysis threshold.

Finally, the elastic scattering angular probabilities are available in the ENDF database as a series of coefficients of Legendre polynomials. These coefficients can be used to construct the probabilities as follows:

$$P(E_i|\cos\theta^*) = \frac{1}{2} + \sum_{l=1}^{N} \frac{2l+1}{2} a_l(E_i)\mathcal{P}_l(\cos\theta^*), \tag{8.5}$$

where $\mathcal{P}_l$ is the l^{th} Legendre polynomial and $a_l(E_i)$ is the corresponding coefficient for incident energy E_i. The sum runs from $l = 1$ to the highest-order nonzero term. Using Eqs. 8.3-8.5 it is possible to numerically evaluate Eq. 8.2. The resulting differential event rates are shown in Fig. 8.27 for ^{28}Si and ^{74}Ge.

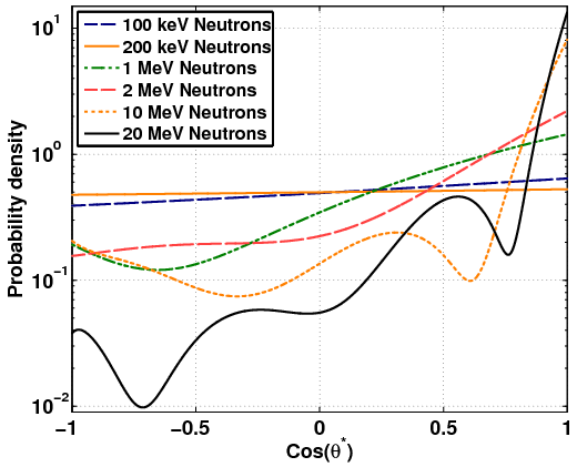

Figure 8.26: Angular probability density for neutrons scattering on ^{28}Si for different incident neutron energies. Data from ENDF database (85). Figure adapted from (78; 84).

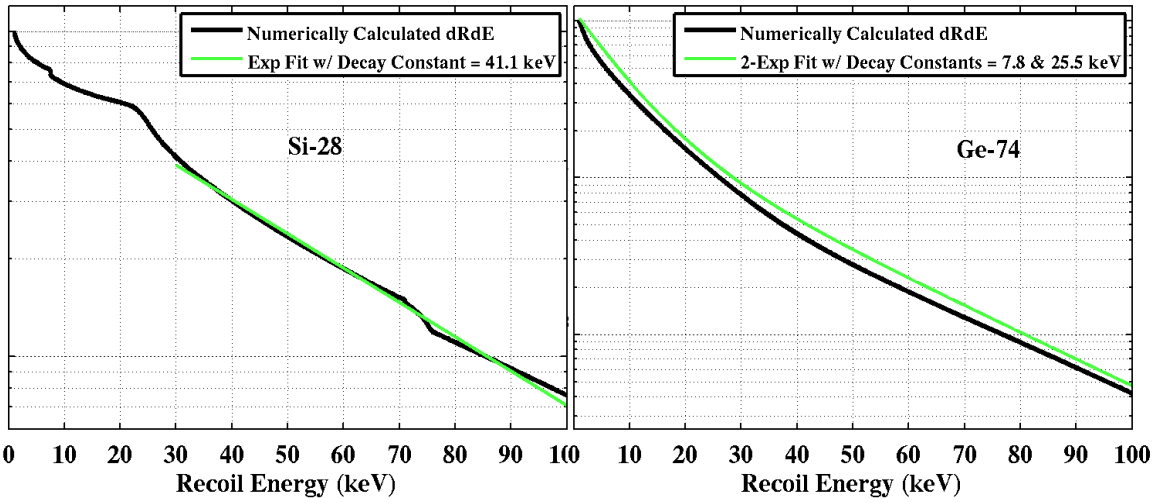

Figure 8.27: Shapes of the numerically calculated differential recoil spectra for elastic scattering of neutrons from a ^{252}Cf source on two common target nuclides: (left) ^{28}Si, partially overlaid with a single exponential fit to the high-energy portion of the spectrum. Three resonance features are visible, though only the largest, at $\sim$20 keV$_r$ is clearly visible in the experimental spectrum. (right) ^{74}Ge data, overlaid with a double exponential fit, shown with a small vertical offset for easier visual comparison. Results are extremely similar for other Ge isotopes. Figure adapted from (78).

The Si spectrum exhibits three bumps that appear to result from the three most prominent resonances in the elastic scattering cross section, at roughly 55, 200, and 550 keV. The resonance at 200 keV is broadest and appears in the feature at $\sim$20 $\mathrm{keV_r}$ in the experimental spectra. The higher energy resonance is washed out by statistical fluctuations, making it less useful as a calibration feature.

The spectrum of both Ge isotopes is fit reasonably well by two exponentials. This spectrum is too featureless for the degeneracy between overall normalization and spectral shape to be broken. Thus the Monte Carlo spectral comparison technique cannot constrain the Ge nuclear recoil energy scale cleanly.

Chapter 9

Energy Scale Impact on WIMP-search Results

This work has presented two methods to constrain the magnitude of uncertainties on the energy scales for nuclear recoils in CDMS II Si and Ge detectors. These methods suggest slight alterations in these energy scales to achieve closer agreement with theoretical models and previous measurements of ionization yield (Sec. 7.4) or to better match the spectral shape of Monte Carlo simulations (Chapter 8). This chapter presents the impact of these energy scale adjustments on the published WIMP-search results from the CDMS II experiment.

9.1 Effect on Ge results

The CDMS II Ge detectors were used for WIMP-search analyses at energy thresolds of 10 keV (83; 42) and 2 keV (72). The nuclear recoil spectrum in Ge has a smooth double-exponential form in the energy ranges used by both low and high-threshold analyses. Sec. 8.5 demonstrated the ineffectiveness of the spectral comparison method when spectral hardness and overall normalization have significant degeneracy, in the absence of precise constraints on the normalization. No alterations to published Ge limits can be inferred from this method.

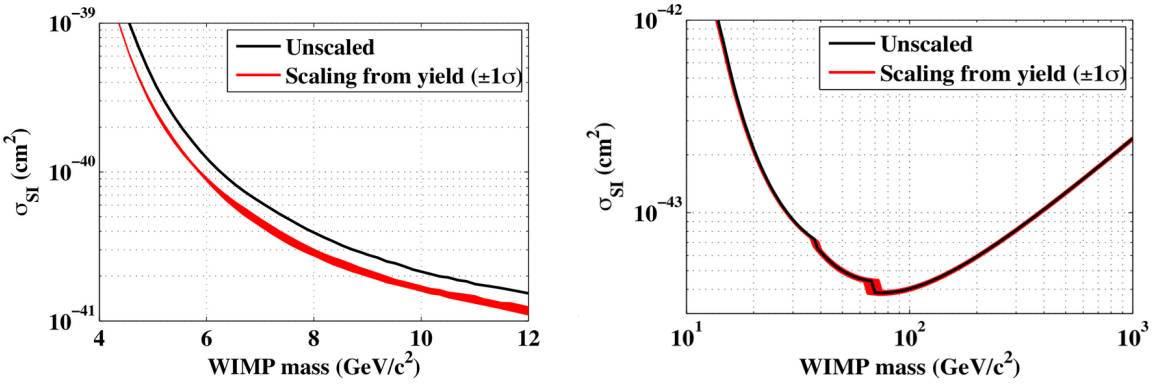

Figure 9.1: (left) Low-mass limit from (72) and a slightly stronger limit resulting from the yield-based energy rescaling derived in Sec. 7.4. The width of this limit results from the $\pm 1\sigma$ uncertainty on the derived energy rescaling factors. (right) High-mass limit from (42) is largely unchanged when yield-based energy rescaling is applied.

The measured ionization yield below $E_R \approx 10\,\mathrm{keV}$ in CDMS II Ge detectors was shown in Sec. 7.4 to be systematically lower than a best-fit parametrization to the Lindhard yield model using measurements from other Ge detectors as inputs. Assuming constant ionization collection down to the 2 keV energy threshold, this suggests that the true recoil energy at threshold was even lower than 2 keV. The adjustment of the lowest recoil energies to even lower values strengthens the low-mass limit (72). The measured yields at higher energies were in much closer agreement wth the model. Thus these energies are shifted very little, and the high-mass limit (42) is largely unchanged. These shifted limits are shown in Fig. 9.1.

9.2 Effect on Si results

WIMP-search analysis of the final exposure of the CDMS II Si detectors (80) set competitive limits at WIMP masses below $\sim 6\,\mathrm{GeV}$, but also observed three candidate events. The dominant surface-event background was estimated at $0.41^{+0.20}_{-0.08}(\mathrm{stat.})^{+0.28}_{-0.24}(\mathrm{syst.})$. The probability that known backgrounds would produce three or more events in the signal region was estimated to be 5.4%. Thus a profile likelihood analysis including the energies of the observed candidates was performed and 68% and 90% CL contours for a possible signal

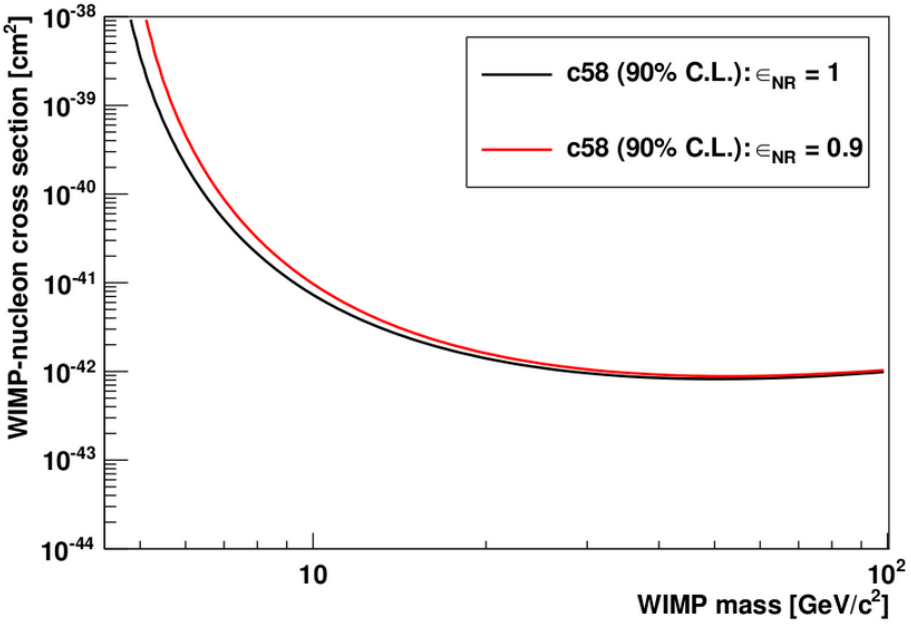

Figure 9.2: (black line) Zero-background spin-independent (90% confidence level) sensitivity limit for the Si analysis (80). (red line) The limit is shifted to slightly higher mass for an inferred phonon collection inefficiency for nuclear recoils at the largest level implied by the spectral comparison to Monte Carlo in Chapter 8, $\epsilon_{\mathrm{NR}} = 0.9$.

were presented (included in Fig. 9.4) in addition to the upper limit.

The effect of a shift in the Si nuclear recoil energy scale at the level inferred by the spectral comparison to Monte Carlo (Chapter 8) was checked by recomputing both the zero background-event sensitivity limit (Fig. 9.2) and the acceptance region preferred by the likelihood analysis including the three candidate energies (Fig. 9.3). The effect in both cases is a small shift toward higher WIMP mass, corresponding to the inferred slightly higher recoil energies. The sensitivity limit is only significantly weaker at WIMP masses below $\sim 10\,\mathrm{GeV}/c^2$. The profile likelihood analysis best-fit point shifts from $M_\chi = 8.58\,\mathrm{GeV}/c^2$ to $M_\chi = 9.13\,\mathrm{GeV}/c^2$.

The observed uncertainty in the nuclear recoil energy scale in Si at the level of $\sim 10\%$ does not significantly alter the interpretation of CDMS II Si WIMP-search results, nor does it ease the tension between its allowed region and recent exclusion limits, such as those from

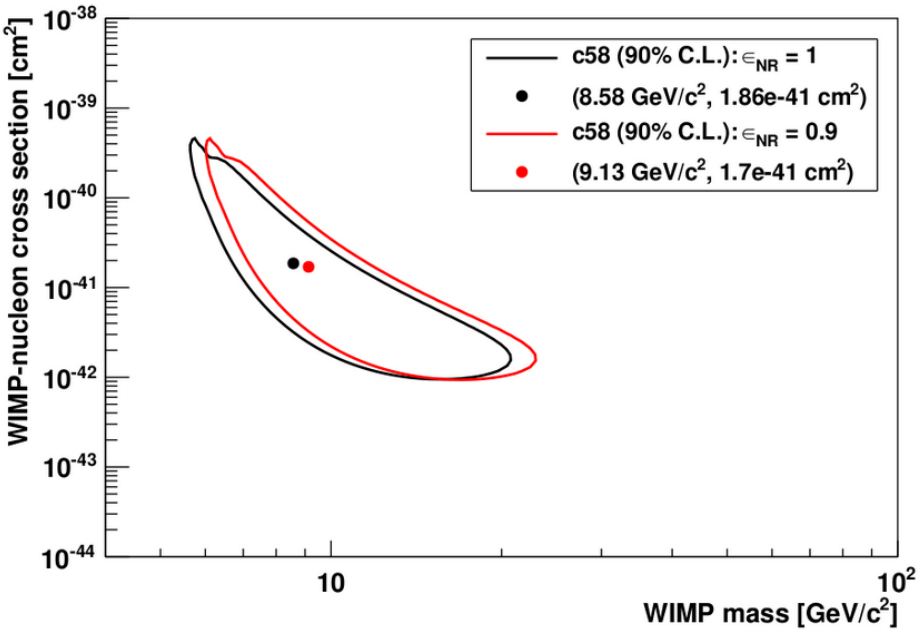

Figure 9.3: (black line) 90% confidence level contours for a possible dark matter signal, from the Si profile likelihood analysis in (80). The black dot shows the maximum likelihood point at ($8.6\,\mathrm{GeV}/c^2$, $1.86 \times 10^{41}\,\mathrm{cm}^2$). (red line) The contour is shifted to slightly higher mass for an inferred phonon collection inefficiency for nuclear recoils at the largest level implied by the spectral comparison to Monte Carlo in Chapter 8, $\epsilon_{\mathrm{NR}} = 0.9$. The red dot shows the shifted maximum likelihood point at ($9.13\,\mathrm{GeV}/c^2$, $1.7 \times 10^{41}\,\mathrm{cm}^2$).

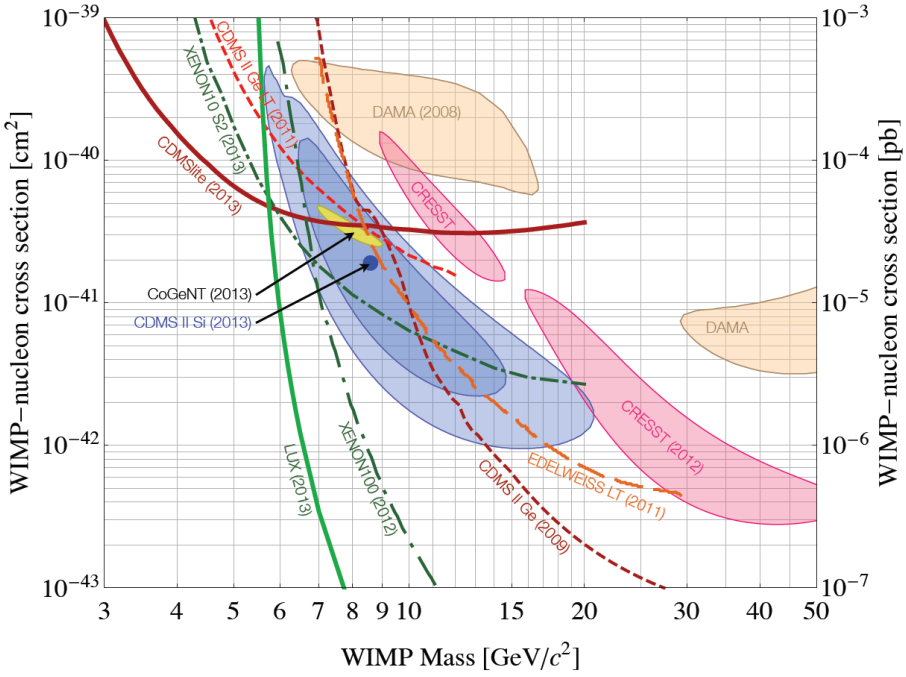

Figure 9.4: Current constraints on the low-mass WIMP parameter space for spin-independent interactions. Shifting the CDMS II Si acceptance region (80) to slightly higher masses, as implied by the Monte Carlo spectral comparison, does not ease tension with exclusion limits from XENON10 S2-only (87), XENON100 (88), and LUX (89).

XENON10 S2-only (87), XENON100 (88), and the first LUX results (89) (Fig. 9.4).

9.3 Complementarity and tension

Efforts to map out the parameter space of spin-independent WIMP-nucleon cross section vs WIMP mass have led to a complicated picture, with the highest level of confusion concentrated in the region of $M_\chi \approx$ 5-10 GeV/c^2, as highlighted in Fig. 9.4. Several results are in tension, and careful studies of energy scales (90; 78) have not led to resolution.

Many efforts are underway to explain the apparent disagreement in these results, most of which remain in active development and are beyond the scope of this discussion. Model-independent frameworks using effective field theories, inelastic dark matter, and multi-component dark matter models may resolve these issues, but the space of potential solutions

remains so large that it is clear that much more data is needed.

Complementarity of approaches appears increasingly critical as the space of dark matter models under serious consideration grows larger. While a majority of efforts have been focused on placing upper limits on the cross section for spin-independent interactions between WIMPs and nucleons, the actual couplings between dark matter and nucleons may be primarily spin-dependent. If there is more than one dark matter particle, studying the expanded space of coupling types and masses requires more than one detection strategy and multiple detection materials.

CDMS II was designed with complementarity in mind, using detectors built on two different target materials. With similar livetimes, a Ge detector will always have more exposure than a Si detector of the same volume, but maximizing exposure is not the only consideration. Coherent enhancement of the spin-independent cross-section favors heavy nuclei and leads to even more sensitivity to spin-independent WIMP-nucleon interactions for Ge, particularly at higher WIMP masses. But the kinematics of nuclear scatters in the two materials also give them varying sensitivities to WIMPs of different masses. Kinematic considerations continue to motivate detector design, and the next generation of dark matter searches (G2) will include many target materials with widely varying mass. Together these experiments will have greatly increased sensitivity to WIMPs with masses below $1\,\mathrm{GeV}/c^2$ up to several TeV/c^2. The expected reach of current and proposed G2 experiments is shown in Fig. 9.5.

9.4 CDMS in the Generation 2 landscape

SuperCDMS SNOLAB has been selected as a primary Generation 2 dark matter search experiment with a unique ability to probe spin-independent interactions for WIMP masses below 5 GeV. Its considerable advantage in the low-mass region is immediately visible in Fig. 9.5. This low-mass reach is complementary to the great high-mass sensitivity of the LZ experiment, a Xe-based successor to LUX and ZEPLIN.

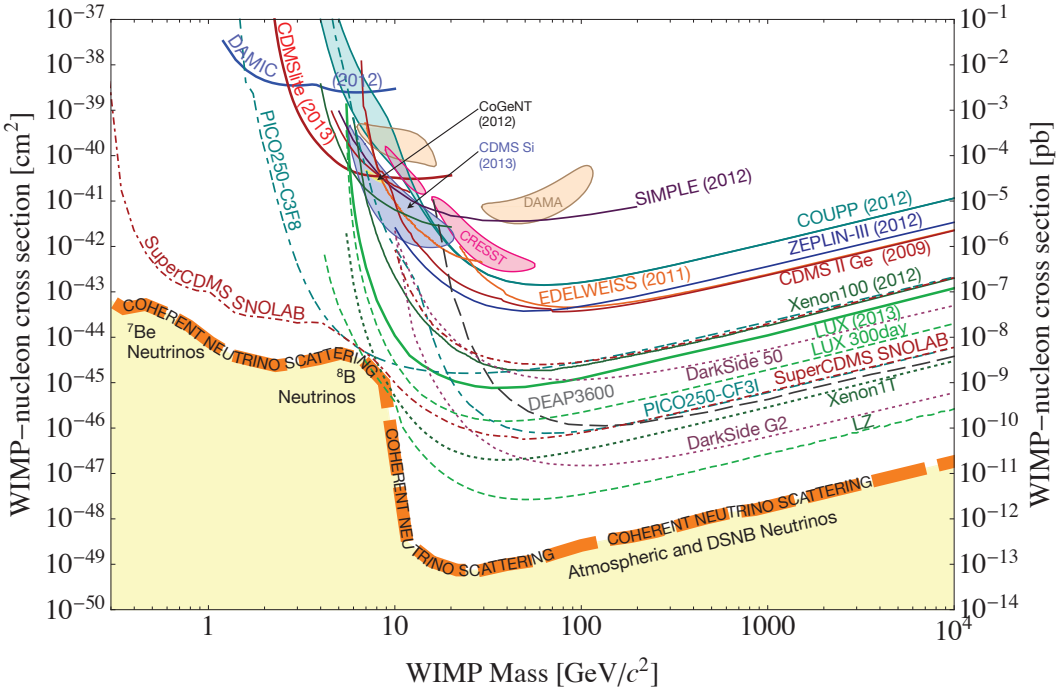

Figure 9.5: Combined low and high-mass projected sensitivities plot for SuperCDMS Soudan and SNOLAB, compared to sensitivities expected for several other proposed G2 experiments, as well as several ongoing experiments. SuperCDMS SNOLAB is alone in its excellent sensitivity to spin-independent interactions of WIMPs with mass below 5 GeV/c^2.

Ultimately, a credible discovery claim requires clear signals that are reproducible in multiple experiments. As a multi-target experiment that can be run in several modes to optimize sensitivity to WIMPs in different mass ranges, and a unique sensitivity to the low-mass region, SuperCDMS is poised to make significant contributions to the understanding of any dark matter signals that appear in the next generation of direct detection experiments.

Appendix A

Soudan Software and Data Quality System

This Appendix discusses details regarding the handling and verification of data after the amplified charge and phonon signals are transferred from the DAQ hardware to the on-site network of processing and real-time analysis computers. The data acquisition software used in CDMS II running had many small modifications but was largely unchanged for SuperCDMS Soudan running. An entirely new suite of data quality diagnostics was created to address new challenges in understanding and evaluating data from the next generation iZIP detectors.

A.1 Data acquisition software

The software component of the Soudan data acquisition system (DAQ) is composed of an interlocking group of C++ and Java programs run on a set of several modest servers in the Soudan electronics room. This system is modular in nature and the various specialized servers communicate using the CORBA network-messaging framework. The entire system is controlled through a single primary cross-platform "Run Control" GUI written in Java, through which separate GUIs can be spawned to perform each of the other major functions

in a centrally-controlled way (see Fig. A.1). Run Control is typically accessed from one of the electronics room servers, but secure remote access is possible through the use of Kerberos encryption, GSSAPI credential forwarding, and the VNC remote desktop server, channeled through a Secure Shell (`ssh`) tunnel.

With full readout of all detectors, the CDMS II DAQ is capable of recording event traces at a rate of about 20 Hz, while typical WIMP-search event rates during periods of good detector performance are closer to 0.3 Hz. This level of dead time prevents the system from recording a large fraction of the recoil events during ^{133}Ba calibration, which can have have recoil rates of 200 Hz or greater. To reduce the dead time, a selective readout mode was implemented, in which an event's digitizer output is recorded only for those detectors that issued phonon triggers for that event, rather than for all detectors and all veto panels. For calibration data, on average only about two detectors trigger for any given event, so the time required to transfer and record this data is greatly reduced, and trigger rates of $\sim$70 Hz are attainable. WIMP-search and neutron calibration data sets are still acquired in full readout mode.

A.2 Data management

The DAQ software writes raw data directly to local disks in the mine. Complete data files are processed through a series of Perl scripts, which compress the files, write a compressed copy to digital backup tape, and transfer the compressed files to the surface. When this process is complete, another monitoring script is triggered that ensures sufficient disk space is maintained on the mine disks by deleting files that have been successfully copied both to backup tape and to a surface disk.

The surface disks are attached to a cluster of 30 dual-core Linux computers known as the Soudan Analysis Cluster (SAC). In addition to writing a second copy of the raw data files to tape, this cluster performs the first processing of the data through a set of data reduction routines to produce reduced quantities (RQs). These low-level RQs are used by the data quality system for preliminary checks of the current performance of the experiment.

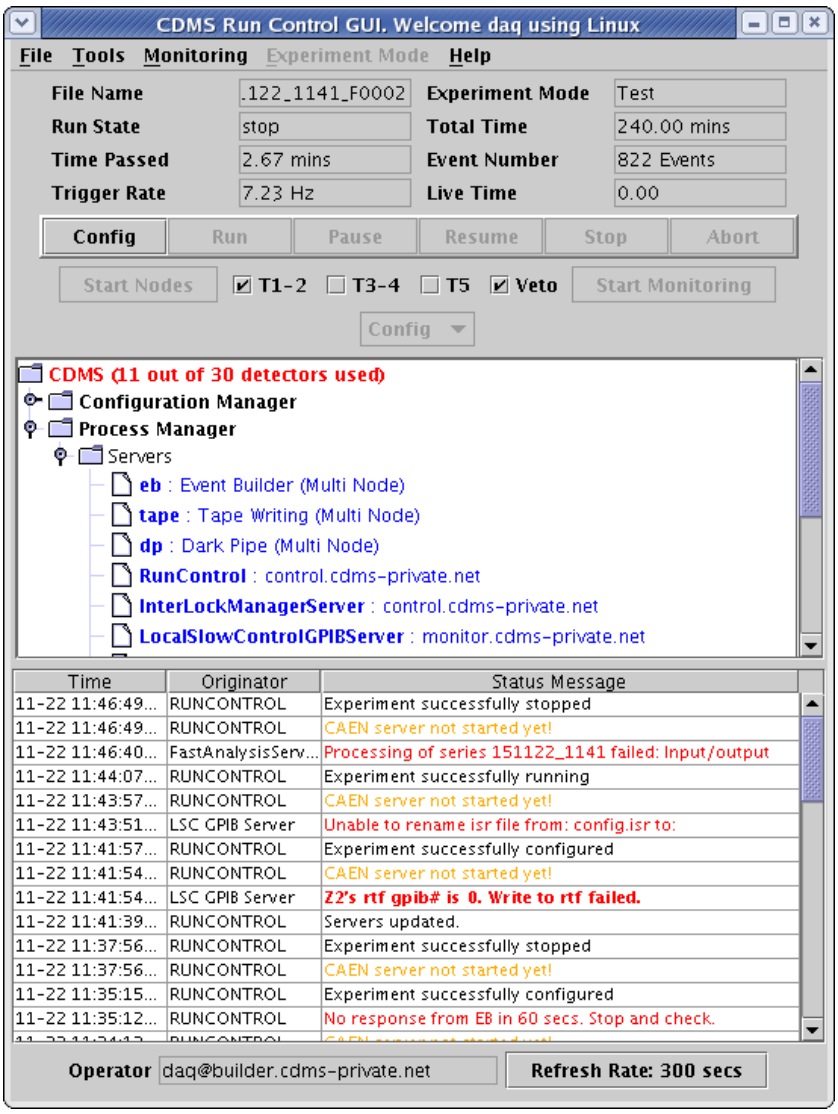

Figure A.1: The Run Control graphical user interface. As the primary control center for the Soudan DAQ software, many sub-systems can be accessed from here, and it can be used to change configurations and begin and end data acquisition from any location, primarily through VNC,with proper security credentials.

Final processing of the data (after energy calibration, etc.) is processor-intensive and is done at Fermilab on the FermiGrid computing cluster, where ∼100 CPUs can be dedicated to the processing at any given time. After this processing is done, the final data is distributed to the home institutions of the analyzers.

A.3 SuperCDMS Soudan DQ System

The SuperCDMS Soudan experiment was the first to use 1 in thick Ge iZIP detectors. Additional complexity resulting from the dual-sided nature of both the phonon and ionization detection systems, as well as observed trends in relatively short-term neutralization loss at test facilities, led to the need for a new level of real-time data monitoring and analysis, both to allow quick adjustments and detector tuning evaluation during the commissioning phase and to ensure stable operation and acquisition of high quality physics data over long time scales. Instability in operation could lead to drifts in the energy scale, introducing systematic calibration errors, on which earlier chapters of this work have placed several upper bounds.

A.3.1 User interface

The user is presented with a table summarizing the conditions of the most recently acquired data series, as in Fig. A.2. This table provides dynamic links to log files specifying complete run conditions, including detector trigger settings, charge channel biasing, DC voltage offsets on phonon channels, readout mode, and user-generated series quality diagnosis logs. It also provides links to the real-time analysis plots discussed in Sec. A.3.2.

The bulk of this interface is written in JavaScipt, and it reads a MySQL database to parse the status of the data acquisition system and to query this information for the series under study – by default these will be series from the last several days, but many search tools are provided to query the database for a specific category of series. Apache Tomcat is used to interface with and display the very large number of diagnostic plots available for

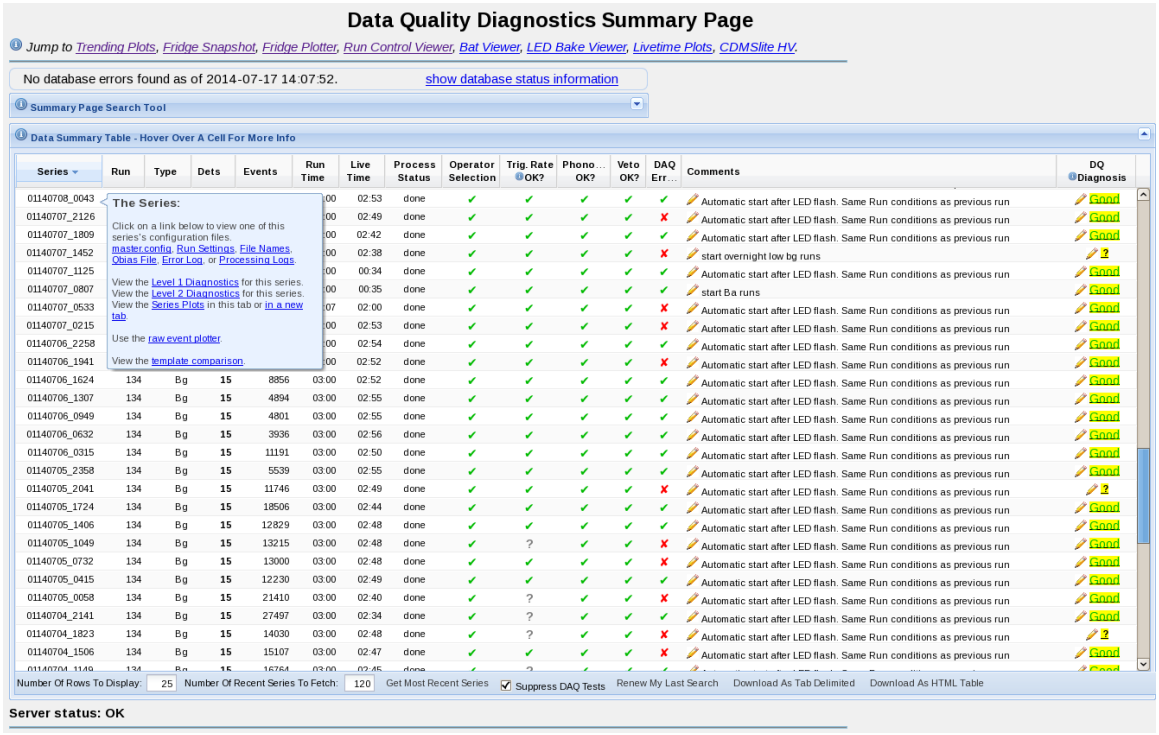

Figure A.2: Primary user interface to the SuperCDMS Soudan data quality monitoring system, presented as a password-protected globally-accessible webpage.

any given refrigerator run.

A.3.2 Real-time analysis

The observed neutralization trends for iZIP detectors led to a standardized maximum length of three hours for each data series taken for the SuperCDMS Soudan experiment. Each series begins with a re-evaluation of the noise environment through the sampling of 500 traces on each sensor channel, gathered randomly over a period of two to three minutes. A pulse rejection algorithm is run to ensure the noise sample is not contaminated with actual physics events. The noise traces are filtered, digitized, and run through a fast Fourier transform to generate power spectral density (PSD) plots. These plots are designed to be viewed by the operators of the experiment in real time to assess whether the noise environment for current data series is acceptable.

As raw data is acquired, it is processed through a rough calibration template. These intermediate files are read by a suite of automated fast-analysis scripts to provide near-instant feedback to the operator about the state of the detectors and the data being gathered.

These plots are divided into two levels. The first level emphasizes any basic operational faults in the detectors, such as dead charge or phonon channels, while also monitoring trigger rates and the state of the muon veto. This level includes the following plots:

1. Noise PSDs for each channel on each detector (Fig. A.3). These are constructed from 500 random triggers taken at the beginning of each dataset to thoroughly sample the noise environment at that time and in that bias state. These plots can be used to monitor changes in the noise environment over long periods of time or to check for shorts, dead channels, charge breakdown, or other operational problems, as in Fig. A.4.

2. Detector event distribution plots (Fig. A.5)

    - Phonon Delay, a map in which each event's x- and y-coordinate is calculated by projecting the unit vector pointing toward each channel's center onto the positive or negative x- or y-axis and using this as a weighting for the sum across channels of their "20% risetimes" – the delay between the start of digitization and the time at which the trace reaches 20% of its maximum.
    - Phonon Partition, a map similar to the delay map, but instead of timing information, the x- and y-coordinates are calculated by a weighted sum over each channel's energy as reconstructed by the optimal filter. This same technique is adapted for a "detector side view," by defining a radial partition and a "z-partition," which projects each side's total phonon energy onto the ±z-axis.
    - Phonon Fraction, a simple histogram of the fraction of the total phonon energy coming from each of the each separate phonon channels per detector
    - Ionization Distribution, a scatter plot of the distribution of ionization energy between the inner and outer charge channels, for each detector side. An additional

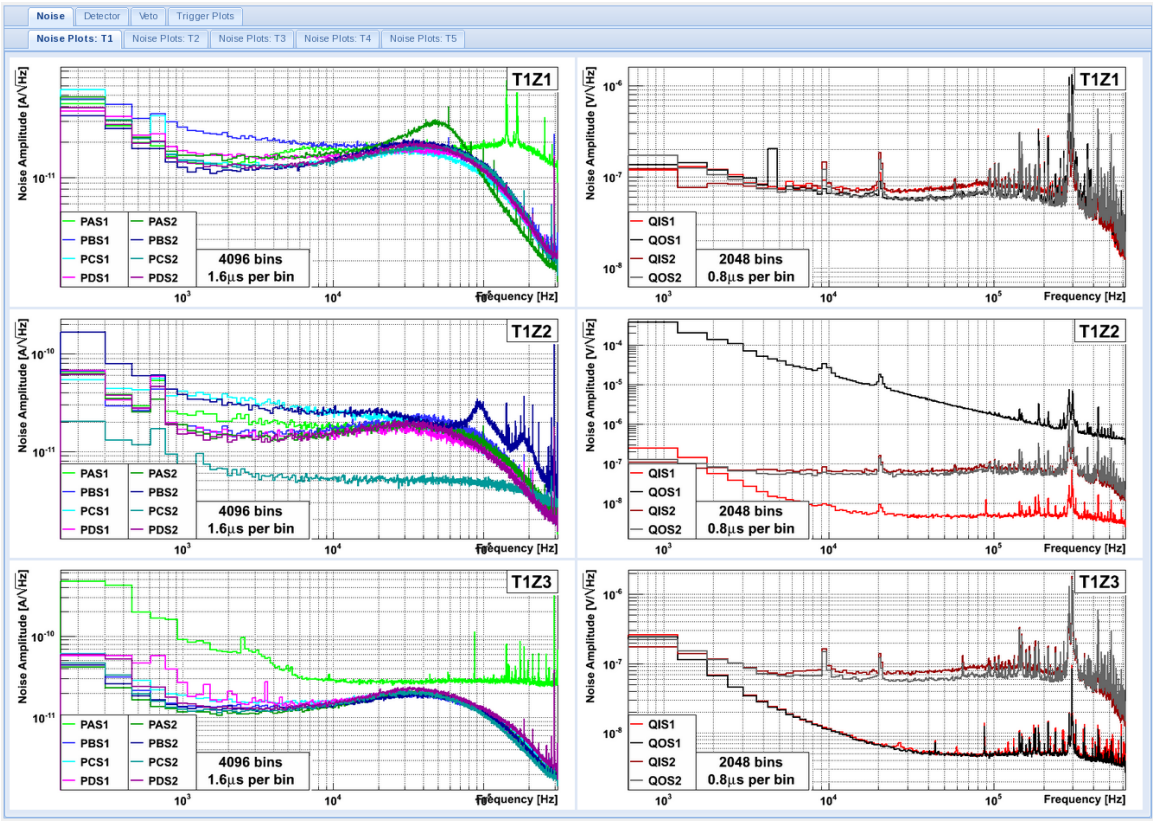

Figure A.3: Power spectral density (PSD) noise plots for all Tower 1 iZIP detector channels, both phonon (left) and charge (right), taken from an early data series in which numerous channels had performance problems.

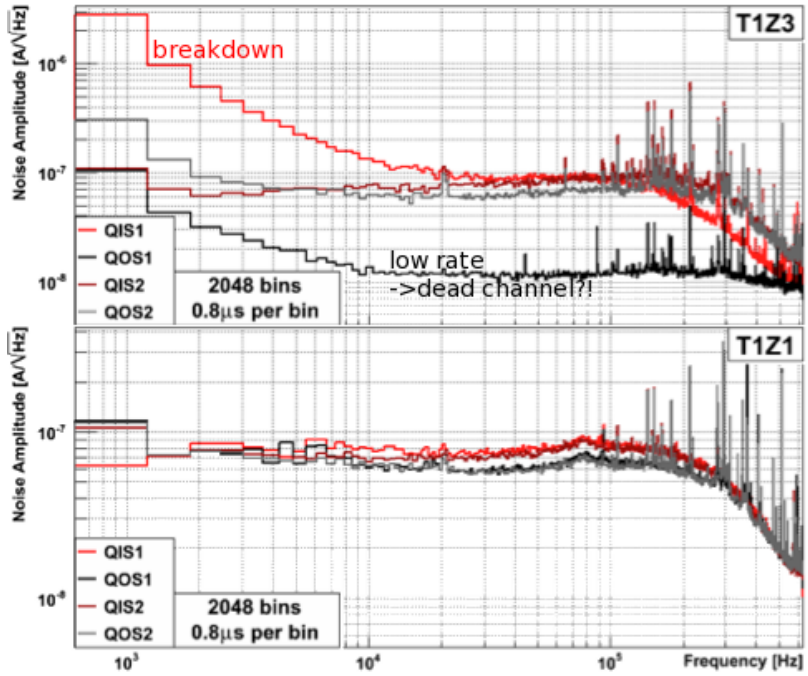

Figure A.4: (top) Problems visible in the noise PSD for the charge channels of a single detector. A steep rise in low frequency charge noise indicates possible charge breakdown, and a uniformly low PSD points to a channel that may be dead. (bottom) Noise PSDs for a detector with all charge channels functioning properly.

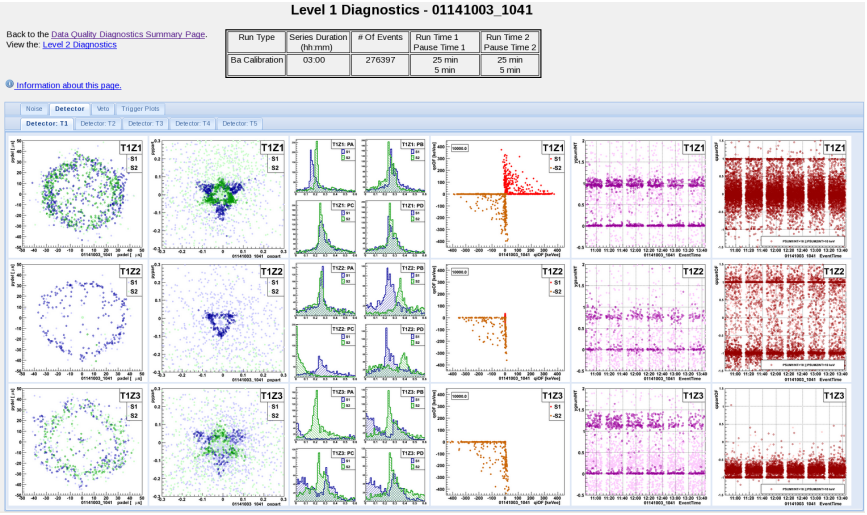

Figure A.5: The first level of real-time detector diagnostic plots, produced continuously for each series during data acquisition. These plots emphasize any basic operational faults in the detectors.

plot shows the charge energy on side 1 vs that on side 2.

- Ionization Partition, another "detector side-view" showing position along the z-axis vs radial position, the latter defined separately for each side.

3. Short-term Trending Plots, which track one quantity vs time over the length of the series. This is particularly useful for monitoring detector neutralization. Quantities monitored in this way include the ionization yield, ionization/phonon z-partition, and ionization/phonon radial partition.

4. Veto plots, showing energy spectra from events recorded in each of the forty separate veto panels.

5. Trigger plots, showing both the number of triggers registered in each half-detector DIB, and a scatter plot vs time showing, for each trigger, the time since the previous trigger.

The second level of plots (Fig. A.6), show more subtle trends and generally require less monitoring by a typical operator during routine running.

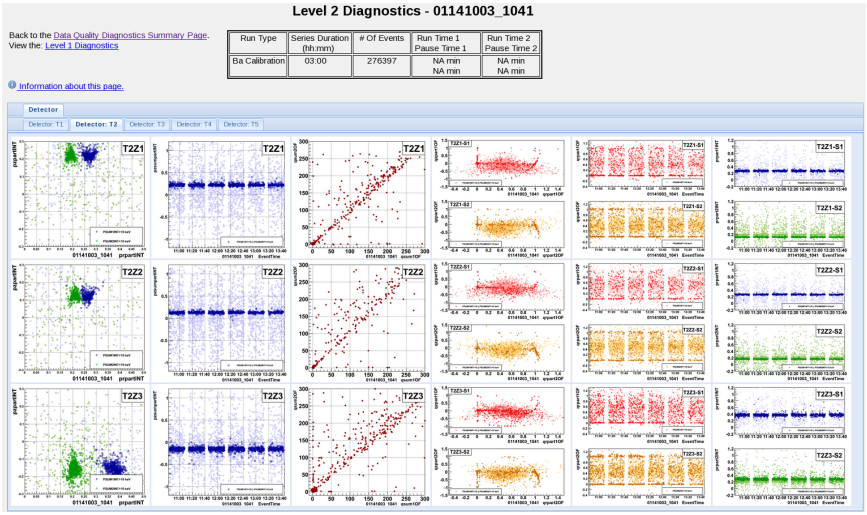

Figure A.6: The second level of detector diagnostic plots, used to diagnose subtle time-dependent behavior and neutralization states.

Python backend

A series of scripts written in Python to interface with ROOT libraries form the analysis infrastructure of the data quality suite. These scripts run at regular intervals by the cron scheduling daemon. They check for the appearance of data files processed through an initial rough calibration step by comparing timestamps of directory contents to that of a logfile recording the scripts' previous runtimes. If new files are found, the corresponding series are queued for online analysis processing.

For maximum flexibility, no details of the current detector setup are coded into the analysis scripts. A file containing the metadata for each series is read and a python dictionary is built mapping detector material, tower number, and location within the tower to a single detector index. This dictionary is queried to determine which scripts are to be run on any given detector, and to provide labeling information used in the creation of the plots.

A single master scipt is called with optional "mode numbers" to restrict the class of plots to be generated at any given time, to allow for the varying frequencies desired for plot updates, and the varying processing times involved in their generation.

A.3.3 Long-term trending

Analogous to the short-term trending plots automatically generated as part of the fast-analysis suite discussed in A.3.2, another tool was created to monitor trends over longer periods of time, shown in Fig. A.7.

A wide range of operational quantities are written to the MySQL run database over time during data acquisition, including binned trigger rates, DC phonon offsets, binned ionization yield, and binned z-partitions from the ionization and phonon channels. By querying the run database, the operator or any other interested party is able to study long-term trends in detector operation over much longer time periods, much more easily than was previously possible.

As the SuperCDMS experiment transitions to SNOLAB with a much larger number of detectors, low barriers to entry in widely-distributed diagnosis of detector operation issues, as made possible by further extensions to the system presented here, will be of critical importance.

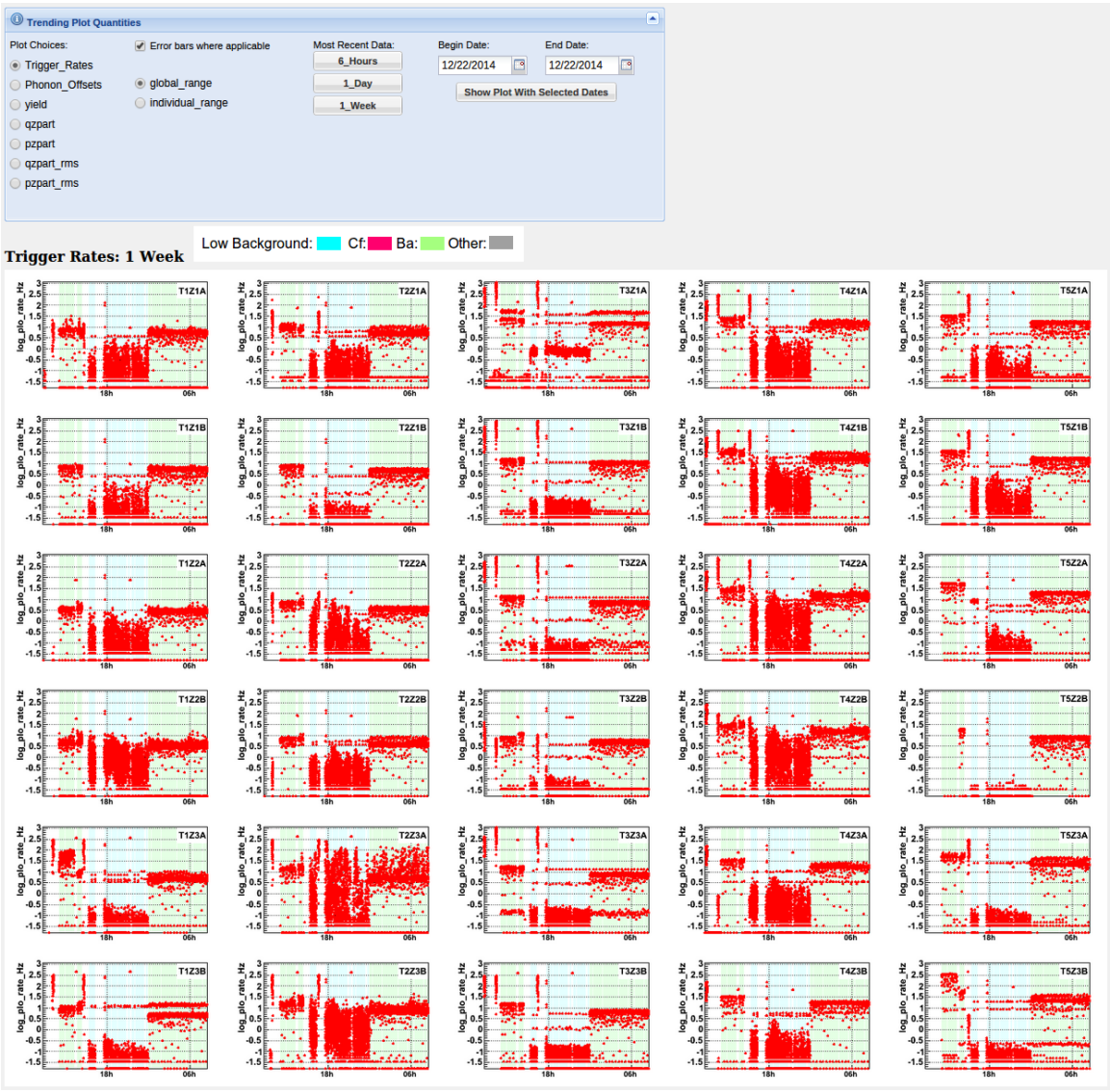

Figure A.7: User interface for the long-term trending plot generation tool. Plots are immediately available for the most recent 6-hour, 1-day, and 1-week periods, and can generally be computed for any other date range in a matter of seconds.

References

[1] V. C. Rubin, W. K. J. Ford, and N. Thonnard, Astrophys. J. **238**, 471 (1980).

[2] J. Filippini, *A Search for WIMP Dark Matter Using the First Five-Tower Run of the Cryogenic Dark Matter Search*, PhD thesis, University of California, Berkeley, 2008.

[3] D. E. Johnston *et al.*, (2007), arXiv:0709.1159.

[4] D. Clowe *et al.*, (2006), arXiv:astro-ph/0608407.

[5] C. Amsler *et al.*, Phys. Lett. **B667** (2008).

[6] V. Springel *et al.*, Nature **435**, 629 (2005).

[7] M. Kowalski *et al.*, Astrophys. J. **686**, 749 (2008).

[8] G. Jungman, M. Kamionkowski, and K. Griest, (1995), arXiv:hep-ph/9506380.

[9] E. W. Kolb and M. Turner, *The Early Universe* (Westview Press, 1990).

[10] K. M. Zurek, Phys.Rept. **537**, 91 (2014), 1308.0338.

[11] K.-Y. Choi and O. Seto, Phys. Rev. D **88**, 035005 (2013).

[12] G. Farrar and M. Shaposhnikov, Phys. Rev. Lett. **70**, 2833 (1993).

[13] T. Lin, H.-B. Yu, and K. Zurek, Phys. Rev. D **85**, 063503 (2012).

[14] R. D. Peccei and H. R. Quinn, Phys Rev. Lett. **38**, 1440 (1977).

[15] C. Baker *et al.*, Phys. Rev. Lett. **97**, 131801 (2006).

[16] H. Georgi and L. Randall, Nucl.Phys. **B276**, 241 (1986).

[17] Y. Nambu, Phys. Rev. **117**, 648 (1960).

[18] S. J. Asztalos *et al.*, (2009), arXiv:0910.5914.

[19] E. Komatsu *et al.*, (2008), arXiv:0803.0547.

[20] P. Tisserand *et al.*, Astronomy and Astrophys. **469**, 387 (2007), arXiv:astro-ph/0607207.

[21] M. Milgrom, Astrophys. J. **270**, 365 (1983).

[22] J. D. Bekenstein, Phys. Rev. **D70**, 083509 (2004).

[23] L. Goodenough and D. Hooper, (2009), 0910.2998.

[24] T. Daylan *et al.*, (2014), 1402.6703.

[25] K. Abazajian and M. Kaplinghat, Phys. Rev. D **86**, 083511 (2012).

[26] D. Malyshev, I. Cholis, and J. D. Gelfand, The Astrophysical Journal **722**, 1939 (2010).

[27] C. Weniger, Journal of Cosmology and Astroparticle Physics **2012**, 007 (2012).

[28] IceCube Collaboration, M. Aartsen *et al.*, Phys. Rev. Lett. **110**, 131302 (2013).

[29] ATLAS Collaboration, G. Aad *et al.*, Phys. Rev. Lett. **110**, 011802. 20 p (2012).

[30] A. Kurylov and M. Kamionkowski, Phys.Rev. **D69**, 063503 (2004), hep-ph/0307185.

[31] J. D. Lewin and P. F. Smith, Astropart. Phys. **6**, 87 (1996).

[32] R. Helm, Phys. Rev. **104**, 1466 (1956).

[33] R. Bernabei *et al.*, The European Physical Journal C **67**, 39 (2010).

[34] CoGeNT Collaboration, C. Aalseth *et al.*, Phys. Rev. Lett. **107**, 141301 (2011).

[35] K. Freese, M. Lisanti, and C. Savage, ArXiv e-prints (2012), 1209.3339.

[36] J. Billard, L. Strigari, and E. Figueroa-Feliciano, Phys.Rev. **D89**, 023524 (2014), 1307.5458.

[37] F. Ruppin, J. Billard, E. Figueroa-Feliciano, and L. Strigari, Phys.Rev. **D90**, 083510 (2014), 1408.3581.

[38] E. Armengaud *et al.*, Physics Letters B **687**, 294 (2010).

[39] P. Brink *et al.*, Nuclear Instruments and Methods in Physics Research Section A: Accelerators, Spectrometers, Detectors and Associated Equipment **559**, 414 (2006), Proceedings of the 11th International Workshop on Low Temperature Detectors LTD-11 11th International Workshop on Low Temperature Detectors.

[40] SuperCDMS Soudan Collaboration, R. Agnese *et al.*, Appl.Phys.Lett. **103**, 164105 (2013), 1305.2405.

[41] The CDMS and EDELWEISS Collaborations, Z. Ahmed *et al.*, Phys. Rev. D **84**, 011102 (2011).

[42] Z. Ahmed *et al.*, Science (2010), 10.1126/science.1186112.

[43] E. Armengaud *et al.*, Physics Letters B **702**, 329 (2011).

[44] CoGeNT Collaboration, C. Aalseth *et al.*, Phys.Rev. **D88**, 012002 (2013), 1208.5737.

[45] CoGeNT Collaboration, C. Aalseth *et al.*, Phys. Rev. Lett. **106**, 131301 (2011).

[46] CoGeNT Collaboration, C. Aalseth *et al.*, (2014), 1401.3295.

[47] M. Pepin, CDMS II global gamma monte carlo, CDMS internal note, 2013.

[48] B. S. Neganov and V. N. Trofimov, Otkrytia i izobreteniya **146** (1985).

[49] P. N. Luke, J. Appl. Phys. **64**, 6858 (1988).

[50] B. Cabrera, Notes on electron-phonon scattering, CDMS internal note, 1993.

[51] T. Bruch, *A Search for Weakly Interacting Particles with the Cryogenic Dark Matter Search Experiment*, PhD thesis, University of Zurich, 2010.

[52] S. Golwala, *Exclusion limits on the WIMP-nucleon elastic-scattering cross section from the Cryogenic Dark Matter Search*, PhD thesis, University of California, Berkeley, 2000.

[53] C. A. Klein, Journal of Applied Physics **39**, 2029 (1968).

[54] F. E. Emery and T. A. Rabson, Phys. Rev. **140**, A2089 (1965).

[55] R. Pehl, F. Goulding, D. Landis, and M. Lenzlinger, Nuclear Instruments and Methods **59**, 45 (1968).

[56] Y. P. Varshni, Physica **34**, 149 (1967).

[57] C. D. Thurmond, J. Electrochem. Soc. **122**, 1133 (1975).

[58] C. A. Klein, IEEE Transactions on Nuclear Science **15**, 214 (1968).

[59] J. Lindhard *et al.*, Mat. Fys. Medd. K. Dan. Vidensk. Selsk. **33**, 1 (1963).

[60] A. Mangiarotti *et al.*, Nucl. Inst. Meth. A **580**, 114 (2007), Proceedings of the 10th International Symposium on Radiation Physics (ISRP) 10.

[61] J. Lindhard *et al.*, Mat. Fys. Medd. K. Dan. Vidensk. Selsk. **33**, 1 (1963).

[62] J. F. Ziegler, M. D. Ziegler, and J. P. Biersack, Nuclear Instruments and Methods in Physics Research B **268**, 1818 (2010).

[63] I. S. Tilinin, Phys. Rev. A **51**, 3058 (1995).

[64] B. L. Dougherty, Phys. Rev. A **45**, 2104 (1992).

[65] T. Shutt *et al.*, Phys. Rev. Lett. **69**, 3531 (1992).

[66] D. Barker, W.-Z. Wei, D.-M. Mei, and C. Zhang, Astroparticle Physics **48**, 8 (2013).

[67] P. S. Barbeau, J. I. Collar, and O. Tench, Journal of Cosmology and Astroparticle Physics **2007**, 009 (2007).

[68] P. Barbeau, *Neutrino and Astroparticle Physics with P-Type Point Contact High Purity Germanium Detectors.*, PhD thesis, U. Chicago, 2009.

[69] CDMS Collaboration, Z. Ahmed *et al.*, (2012), 1203.1309.

[70] K. W. Jones and H. W. Kraner, Phys. Rev. C **4**, 125 (1971).

[71] CDEX-TEXONO Collaboration, Ruan, Xichao and (CDEX-TEXONO Collaboration), Nuclear recoil quenching factor measurement for hpge detector.

[72] CDMS Collaboration, Z. Ahmed *et al.*, Phys. Rev. Lett. **106**, 131302 (2011).

[73] Y. Messous, Astropart.Phys. **3**, 361 (1995).

[74] C. Chasman, K. Jones, and R. Ristinen, Phys.Rev.Lett. **15**, 245 (1965).

[75] A. Sattler, F. Vook, and J. Palms, Phys.Rev. **143**, 588 (1966).

[76] E. Simon *et al.*, Nucl.Instrum.Meth. **A507**, 643 (2003), astro-ph/0212491.

[77] L. Baudis *et al.*, Nucl.Instrum.Meth. **A418**, 348 (1998), hep-ex/9901028.

[78] CDMS Collaboration, Z. Ahmed *et al.*, (In preparation.).

[79] EDELWEISS Collaboration, A. Benoit *et al.*, Nucl.Instrum.Meth. **A577**, 558 (2007), astro-ph/0607502.

[80] CDMS Collaboration, R. Agnese *et al.*, Phys. Rev. Lett. **111**, 251301 (2013).

[81] CoGeNT collaboration, C. Aalseth *et al.*, Phys.Rev.Lett. **106**, 131301 (2011), 1002.4703.

[82] G. Angloher *et al.*, Results from 730 kg days of the CRESST-II dark matter search, 2011, arXiv:1109.0702.

[83] CDMS Collaboration, Z. Ahmed *et al.*, Phys. Rev. Lett. **102**, 011301 (2009).

[84] R. Bunker, *A Low-threshold Analysis of Data from the Cryogenic Dark Matter Search Experiment*, PhD thesis, University of California, Santa Barbara, 2011.

[85] M. Chadwick *et al.*, Nuclear Data Sheets **107**, 2931 (2006), Evaluated Nuclear Data File ENDF/B-VII.0.

[86] K. Shibata *et al.*, Journal of Nuclear Science and Technology **48**, 1 (2011), http://www.tandfonline.com/doi/pdf/10.1080/18811248.2011.9711675.

[87] XENON10 Collaboration, J. Angle *et al.*, Phys. Rev. Lett. **107**, 051301 (2011).

[88] XENON100 Collaboration, E. Aprile *et al.*, Phys. Rev. Lett. **109**, 181301 (2012).

[89] LUX Collaboration, D. S. Akerib *et al.*, Phys. Rev. Lett. **112**, 091303 (2014).

[90] G. Plante *et al.*, Phys. Rev. C **84**, 045805 (2011).